Near-infrared spectroscopy of shocked molecular hydrogen in star formation regions

Amadeu Joaquim Lima Fernandes

Presented for the degree of Doctor of Philosophy

University of Edinburgh

July 1993

This thesis has been composed by me and is entirely my own work except where specifically indicated in the text

Amadeu Fernandes

Dedicado a meus pais
(Dedicated to)

José e Laura Fernandes

Acknowledgements

Over the past three years plus one (MSc) that I have spent at the Royal Observatory Edinburgh, many things have contributed to transform my academic and social life. During that stay, many people have either directly or indirectly contributed to this work. To them, I wish to express my sympathy and thanks for making me feel as if I were at home. Academically, I thank first Peter Brand, my supervisor, for all those "grilling" discussions at coffee time, and for the ever so many Why? questions. His support was invaluable for the success of this work. Thanks also to Liz Gibson, the departmental secretary, for providing all the necessary bits of stationary.

Also I would like to leave a word of thanks for all my colleagues and friends. Thanks to Antonio C. for being my office mate and for the many useful discussions. From my own year, I would like to thank Suzie, Pippa and Dave for being close friends. Other people that also deserve mention are Bob Mann and Bobby Nichol; Steven "Doddsy" for being my office mate and good friend for the last part of my work; Ruth Doherty for thinking highly of my intelligence; Mike and Alistair for playing football, or try to anyway (just joking guys!); another Mike (Short) for reading part of this thesis and Martin for being Mac-user friendly; Chris Davis for being a star formation mate; Phil Puxley for knowing much about reduction of data; Phil James for the coffees, Hugh Jones for being himself, and Horst M. for being the software god of Starlink. Thanks Shona for all the help in the library plus the lifts up the hill.

In a social context, I would like to thank the pseudo-portuguese community in Edinburgh for all the support given on those long and depressing days without a hint of sunshine!! Also, thanks for all the gossip about the deeds of our countryman and for making my visit to Scotland a very enjoyable journey. I will never forget the beautiful sights of Mallaig, Oban, Glencoe and the isle of Skye. To be thanked is also the portuguese research council, JNICT (Junta Nacional de Investigação Científica e Tecnológica) without which this work would not have been possible. Also, for providing the extra money for travel expenses to the United Kingdom Infrared Telescope.

Lastly, some very special people must be thanked. For the very exceptional support and love given by my family in Portugal, I want to express my deepest gratitude and dedicate this work to them.

Table of contents

Abstract

The work presented in this thesis is devoted to the study of the physics of shock waves in the dense molecular cloud environments that are typical of star forming regions. The structure of these shock waves are analysed in terms of the two basic models: J-shock and C-shock.

We have investigated the H_2 emission properties from Herbig-Haro 7 and the DR21 bipolar outflow by measuring several spectral lines arising in the K band. These H_2 lines cover a wide range in energy of the upper level (6000–25000 K) and enables a detailed study of the temperature distribution of the gas. The calculated column density ratios have been compared to J and C–shock models for different shock geometries. We have shown that current oblique J- and C-shock models fail to explain the observed H_2 column density ratios. J-shock models fail to provide sufficient hot gas from behind the shock front and are not able to explain the large line intensities observed in the high-vibrational H_2 lines. The line emission from the 6 positions observed within the HH 7 bow are shown to be consistent with a paraboloidal bow shock geometry, which however necessitates of an extra source of excitation of the high energy levels to explain the H_2 line ratios. We present a study of the effects of the UV radiation field associated with the bow shock structure and show that a shock-induced Far-UV radiation field with a strength of $G_0 = 10^2$–10^3, can account for the observed H_2 line ratios. We suggest that shocks are responsible for the low-lying level excitation of the H_2 molecule while Lyα resonance pumping is responsible for the high-excitation line emission.

Measurements of several infrared emission lines of H_2 in the K window from the DR21 bipolar outflow, show different excitation conditions for the east and west lobes of H_2 emission. The higher H_2 line ratios measured for the east lobe is indicative of enhanced excitation for the high-excitation levels of the H_2 molecule, which can be caused by either shock-produced Lyα resonance pumping or by direct UV excitation of H_2 from the central HII region. This is consistent with the east lobe being bordering the central HII region and producing higher fluorescent fluxesWe show that the H_2 emission can be explained in terms of a model consisting of a C-shock and a PDR. The H_2 line ratios are best fitted with a PDR model with parameters: FUV field in the range $10^2 \leq G_0 \leq 10^3$ and densities $n \geq 3 \times 10^3$ cm^{-3}.

We show that the H_2 fluorescent emission from both HH 7 and DR21 is reproduced better with an ortho to para ratio of 1.8.

Chapter 1

Introduction

Stars are the basic component of the observable universe. Their formation, evolution and death are on-going physical processes that determine the ultimate fate of our galaxy. The energy generated by a collapsing cloud to form one or more stars, is absorbed and re-emitted by the interstellar medium in ways that can be used to indicate the physical conditions in the ambient cloud. In their late stages of evolution, stars can also deposit their energetic contents back into the interstellar medium causing violent shock waves that irreversibly change the dynamics of the gas.

Dense molecular clouds are the preferred sites for star formation (McKee 1989). Our understanding of the star formation process is still poor and depends greatly on the observations at these regions and on our ability to produce physical models capable of explaining these observations. Shock phenomena sweeping up the interstellar medium cause an irreversible change of entropy within the molecular gas cloud and can initiate or enhance physical and chemical processes that lead to the formation of new stars or halt the collapse of the molecular cloud by causing violent turbulent motions. For this reason, the study of shock waves has become extremely important in diagnosing the interstellar gas dynamics and its implications for star formation.

1.1 Shock waves in star forming regions

It is now widely accepted that all present star formation occurs within giant molecular clouds (GMC) which coalesce from the interstellar medium (ISM) by cloud-cloud collisions in a dynamical interaction that is moderated by powerful supernova events and other energetic phenomena (Blitz 1991). These GMCs provide the initial conditions for the process of star formation that occurs deep in the central and dense molecular cores. They have typical masses of around 10^5 - 10^6 $M_\odot$ and diameters of order 30 - 50 parsecs (Blitz 1991). The survey of local molecular material within 1 kpc of the Sun (Dame et al. 1986) finds no GMCs without star formation. Thus, it appears that star formation occurs rapidly after the formation of a GMC. This implies that all GMCs are young $\approx 3 \times 10^7$ years (Blitz et al. 1980) and that since all GMCs seem to be sites of star formation, especially of massive stars, the clouds do not appear to be able to survive the birth of more than a few generations of star formation. Their innermost regions are favourable sites to form new stars with the enhanced magnetic field providing clump support and the dominant neutral molecules collapsing to the centre core by ambipolar diffusion. This diffusion of the neutrals past the ions occurs in a timescale of $\approx 10^7$ years with the ionisation level being determined by cosmic rays. However, the interstellar far-ultraviolet radiation field ($6 \text{ eV} \leq h\nu \leq 13.6 \text{ eV}$) also permeates a significant fraction of the cloud (to optical depths $A_V \approx$ a few), and only well shielded cores, representing a few percent of the cloud can collapse to form stars (McKee 1989).

The composition of the ISM is complex. The molecular gas is typically at a temperature $T \approx 10$ K and a density $n \approx 10^3$ cm^{-3} and is concentrated in self-gravitating molecular clouds (McKee et al. 1991). The gas is predominantly atomic H with a smaller amount of He ($\approx 10\%$ by number) and trace amounts of heavier elements (less than 0.1% by number). Some of the heavier elements or metals are attached to small dust grains that range in size from less than 1 nm to about 100 nm. Tying all these components together is a magnetic field that has a typical strength of a few microgauss, although it is stronger in denser regions (Spitzer 1978). The magnetic field is perhaps the most difficult of the interstellar parameters to determine. Some observational methods have included the analysis of pulsar rotation and dispersion measures, the detection of the Zeeman effect, and the comparison of Galactic synchrotron emission with the Galactic cosmic-ray electron spectrum at high energies (Heiles 1976; Troland et al. 1986). When individual GMCs turn a fraction of their mass (≈ 5%) into OB stars, they generate ionised regions (HII regions) that rapidly begin to disrupt the ambient cloud. The energetic far-ultraviolet photons produced in this way are capable of ionising hydrogen and therefore signal the ending of the star formation era.

Each forming star experiences vigorous episodes of mass loss during its formation and evolution to the main sequence. As a consequence, massive bipolar outflows are generated that impact back on the surrounding molecular medium producing powerful shock waves that travel at supersonic speeds. These outflows seem to be driven by strong stellar winds (with velocities of up to 10^3 km s^{-1}) whose observable manifestations include rapidly moving Herbig-Haro (HH) objects (Bachiller et al. 1990; Bally et al. 1991; Eislöffel et al. 1992), high velocity water maser sources, shock excited H_2 emission regions (Hartigan et al. 1989; Solf et al. 1987), and optically visible jets that appear to originate from the vicinity of the circumstellar environment of the young stars (Brand et al. 1988; Burton et al. 1989; Garden et al. 1986; Geballe et al. 1990). Young stars also generate enormous fluxes of ionising radiation, causing the gas to heat and expand at velocities of tens of kilometres per second (McKee and Draine 1991). The molecular gas that is exposed to this energetic radiation is dissociated to within a few optical depths ($A_v \leq 3$), thus creating a photodissociation region (PDR) (Tielens et al. 1985). Similarly to shocks, PDRs are powerful emitters of H_2 radiation, and therefore it is important to discriminate between the two H_2 excitation processes by using, for example, infrared diagnostic lines.

The remaining of this chapter deals with the physics of shock waves (section 1.2); a summary of the different shock structures is presented in section 1.3 and the properties and excitation conditions of the hydrogen molecule is discussed in sections 1.4 and 1.5. Particular emphasis is given to the different excitation conditions in photodissociation regions and shocks (section 1.6). The last section presents the main motives and objectives that formed the basis for this work.

1.2 Physics and dynamics of shocks

Shock waves are driven into molecular clouds by a variety of mechanisms. For example, fast moving clouds generate supersonic gas motions, young stars create powerful outflows, stellar winds and in their late stages stars can blow their contents back to the interstellar medium as supernovae. Shocks are also associated with expanding HII regions and Herbig-Haro objects (Lada 1985; Shull et al. 1987). Because the shock propagates faster than the characteristic signal velocity — local sound speed, the medium ahead of the shock cannot respond dynamically to the shock until this strikes. This creates a discontinuity between the pre-shock and the post-shock gas and the shock front works as a hydrodynamic surprise (McKee et al. 1980; Shull and Draine 1987). The shock then compresses, heats and accelerates the ambient gas and dust producing an increase of entropy across the shock front either by collisions between the shocked and unshocked fluids — collisional shock — or by the generation and dissipation of plasma turbulence — collisionless shock. In a collisionless shock, the shock front will be much thinner than the mean free path due to the low gas density. In consequence, dissipation of energy is accomplished by turbulent processes and magnetic fields rather than collisions (McKee and Hollenbach 1980).

In collisional shocks, the heating of the gas by the conversion of the supersonic motion kinetic energy to thermal energy, excites the vibrational, rotational and electronic degrees of freedom of atoms and molecules. In the dense molecular environments, the absorption of radiation by dust particles makes observations at optical and ultra-violet wavelengths extremely hard. Moreover, most of the emission from these regions arises in the infrared (e.g. lines of H_2) and radio wavelengths (e.g. lines of CO) which makes these spectral regions suitable for study. The emission process by radiative decay from the excited levels of atoms and molecules contributes to the cooling of the gas. In opaque cloud cores ($T \approx 10$–30 K), low rotational lines of CO are the dominant coolant. In the photodissociated surfaces of molecular clouds, fine structure emission from [OI] (63 μm) and [CII] (158 μm) usually dominates the cooling. If the gas is heated to 1000 K or greater, as occurs in shocked regions, then the H_2 line emission is a significant coolant. Since H_2 is the main constituent of the molecular gas, its excitation process is an important tool to diagnose and probe the physics in these regions in which these molecules are collisionally excited into a vibrational-rotational quantum state. Since all these phenomena occur at large optical depths, the only effective observation techniques are in the infrared and radio wavebands. Additionally, the near-infrared region of the spectrum is fairly transparent, i.e., is not heavily absorbed by the earth atmosphere. Some strong transitions that occur in the near-infrared (1-5 μm) are widely used as diagnostics of the shock physics and the H_2 line ratios can be directly compared with the predictions of shock models.

A shock occurs when the medium is disturbed at a speed greater than that of all relevant signal speeds. There are several signal speeds in dense molecular clouds:

- The neutral *speed of sound* :

$$c_s = \sqrt{\frac{\gamma p_0}{\rho_0}} = \sqrt{\frac{\gamma k T_0}{\mu_0 m_{\mathrm{H}}}} \approx 0.1\sqrt{T_0} \ \ \mathrm{kms^{-1}} \tag{1.1}$$

where T is the gas temperature measured in Kelvin, $\mu_0 m_H = 3.9 \times 10^{-24}$ g is the average mass per particle in molecular gas with a helium abundance $n(He)/n_p = 0.1$ and where $n_p = n(H) + 2n(H_2)$. Sound waves are compressional disturbances in which the gas pressure serves as the restoring force.

- The *Alfven speed* :

$$c_A = \sqrt{\frac{B^2}{4\pi\rho}} = 1.8b \ \ \mathrm{km\ s^{-1}} \tag{1.2}$$

where B is the magnetic field (measured in Gauss) and ρ is the total mass density of the molecular material. The variation of B with density in the interstellar medium is approximately given as $B = b\sqrt{n_0}\ \mu$G where n_0 is the density of hydrogen nuclei. In molecular clouds, the Alfven velocity is of the order of a few kilometres per second (Meyers et al. 1988), so b is of order unity. Pure Alfven waves are transverse disturbances in which the magnetic tension serves as a restoring force.

Compressional waves in which both the magnetic pressure and gas pressure provide the restoring force are termed magnetosonic waves and propagate at a velocity $c_{\mathrm{ms}} = \sqrt{c_{\mathrm{s}}^2 + c_{\mathrm{A}}^2}$ (Chernoff et al. 1990).

- The neutral *ion-Alfven speed* :

$$c_{\mathrm{iA}} = \sqrt{\frac{B^2}{4\pi\rho_{\mathrm{i}}}} = \sqrt{\frac{c_{\mathrm{A}}}{\mathrm{x_i}}} \ \mathrm{km\ s^{-1}} \tag{1.3}$$

where ρ_i is the ion mass density and $\mathrm{x_i} = \rho_{\mathrm{i}} / \rho$ is the ion mass fraction. Ion-Alfven waves propagate in the ion gas component only. This speed is much larger than the Alfven speed because the associated inertia is smaller than that associated with the neutral component ($\rho_{\mathrm{i}} << \rho$).

An analysis of wave propagation in molecular cloud material shows that the gas plus field supports modes that involve all of these characteristic velocities (Chernoff 1987). Usually, the sound speed is smaller than the Alfven speed which in turn is smaller than the ionic Alfven speed, i.e., $c_{\mathrm{S}} \le c_{\mathrm{A}} << c_{\mathrm{iA}}$, because the ion fraction is so small in dense molecular clouds, $\mathrm{x_i} \approx 10^{-6} - 10^{-8}$ (Langer 1985). Assuming the velocity of the shock $\mathrm{V_s}$ satisfies $c_{\mathrm{S}} \le c_{\mathrm{A}} < \mathrm{V_s} < c_{\mathrm{iA}}$, then neither normal sound waves nor Alfven waves in the composite medium are capable of transmitting information of the disturbance ahead of the its arrival, but the ion-Alfven waves can. However, the ion-Alfven waves are subject to damping through collisions with the abundant neutrals. Hence, when a disturbance propagates through the medium at a velocity $\mathrm{V_s}$ there are two competing effects taking place simultaneously. First, a signal is transmitted upstream of the disturbance by the ion-Alfven waves that travel ahead of the disturbance — the precursor — because $\mathrm{V_s} < c_{\mathrm{iA}}$. Second, that signal is damped by the ion's collisional coupling to the neutrals, which are slow to respond to any changes. If the signal propagates sufficiently far upstream, then the neutral flow can be heated and slowed so that the neutrals effectively respond to the disturbance upstream — otherwise a shock in the neutrals results.

1.3 Types of shock structures

The structure of interstellar shocks in molecular gas can be divided into two main groups: (a) the non-magnetic jump shock or J-shock and (b) the magnetically moderated continuous shock (MHD) or C-shock. This distinction was first noted by (Draine 1980). Shocks travelling at a velocity exceeding 25 km s^{-1} are usually dissociative and are of J-type (Kwan 1977) whereas shocks propagating into a medium where the magnetic field is dynamically important are of C-type and are non-dissociative. In J-shocks the ions and neutrals are coupled together by collisions and the bulk kinetic energy of the supersonic gas is dissipated into thermal energy. This occurs in an adiabatic transition layer with a lengthscale of the order of the mean free path ($l_{col} \approx {}^{1}/_{n\sigma_{col}}$). The gas then cools radiatively in an extended region behind, which is long compared with the shock front. The first models of J-shocks were simple hydrodynamic fronts and reproduced accurately the H_2 intensities from observations made of a few emission lines. In particular the diagnostic 1-0 S(1) (2.122 μm) to 2-1 S(1) (2.248μm) line ratio was found close to 10 and implied a shock travelling at a speed close to 15 km s^{-1} into a medium of density ≈ 10^5 cm^{-3}. The excitation temperature calculated from the 1-0 S(1) / 2-1 S(1) ratio, suggested that most of the emitting gas is at a temperature close to 2000 K. The major problem facing J-shock models is that they lacked the ability to reproduce the broad line profiles (> 100 km s^{-1}) which are observed in these regions (Brand et al. 1989a Nadeau et al. 1979). In addition, the observations of CO rotational emission lines with J > 30, appeared to be ≈ 2 orders of magnitude stronger than any J-shock model could predict (Watson et al. 1985).

In C-shocks, the ions and electrons are tied to the magnetic field lines and are weakly coupled to the neutrals by collisions. In this case, the bulk kinetic energy is dissipated by ambipolar diffusion with the ions slipping past ahead of the neutrals in a magnetic precursor. Then, the gas variables change continuously in the flow in a transition region that is long compared with the cooling length ($L \approx (v_A/V_s)^2\, l_{col}$). This type of shock occurs for small fractional ionisation levels, where the ion-Alfven velocity is greater than the shock velocity. C-shock models have also been proposed to explain the emission from Orion and accounted successfully for the absolute and relative intensities of H_2 lines emitted from the low vibrational levels, which then were the only ones that could be observed (Chernoff et al. 1982; Draine et al. 1982). When more lines of H_2 originating from upper levels as high as 25000 K (4-3 S(3)) could finally be observed, it was quickly realised that C-shocks provided a poor match. The large column densities observed for these lines could not be obtained with the simple planar C-shock that featured a flat temperature profile and thus this suggested that a more complex shock geometry could be made to fit the data. Fig. 1.1 shows a comparison of the two types of shock structures.

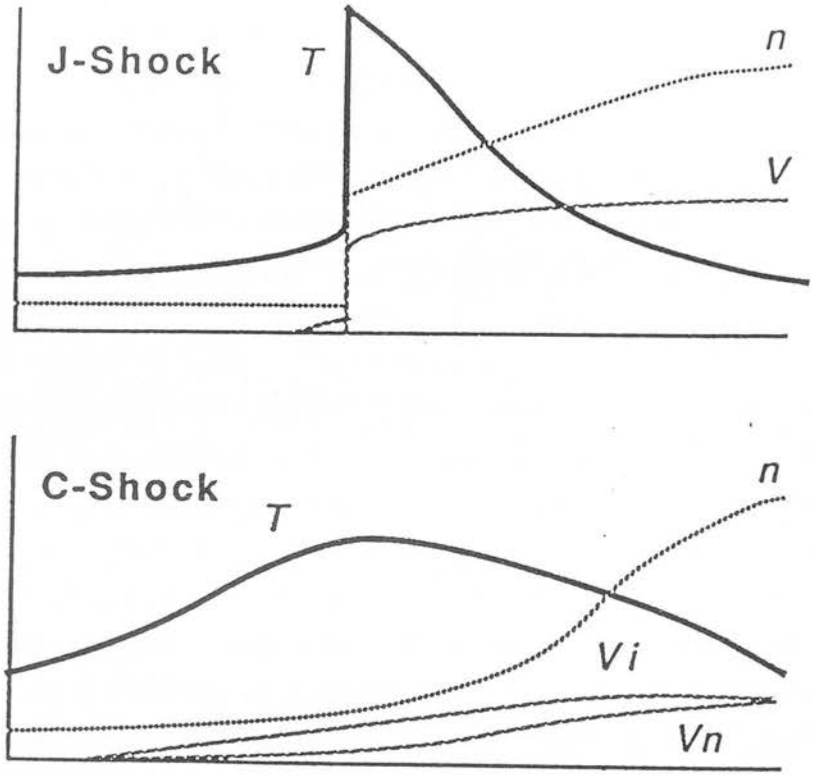

Figure 1.1: The two different types of J- and C-shock structures are shown for comparison. The characteristic profiles of temperature T (thick line), density n (dotted line) and flow velocity V (dashed line) in the ambient gas reference frame are shown to be fundamentally different. In the C-shock case, the relative ion drift past the neutrals is depicted by the two characteristic velocities; V_i (ions) and V_n (neutrals). The neutral gas slowly responds to this motion by collisions and eventually catches up with the ionised component when the cooling has rid the gas of most of the energy and the temperature has dropped to close to the pre-shocked value.

1.4 The importance of H_2 in the interstellar medium

The strongest emission lines from molecular hydrogen occur in the infrared and ultraviolet wavebands. Its detection in the infrared in the interstellar medium was first reported by Treffers et al. (1976) and Gautier et al. (1976). Until then, the interstellar medium was thought to be quiescent and the predictions that had been made for the H_2 line emission (Black and Dalgarno 1976) were due to the rotational-vibrational cascade following electronic excitation by a UV photon – H_2 fluorescence. The new data showed, especially in the Orion molecular cloud, that the emission had a thermal origin implying high gas densities and excitation temperatures of about 2000 K. The passage of a shock wave travelling at a few tens of km s^{-1} appeared to produce a good fit to the observations. Infrared fluorescence was discovered only 11 years later by Gatley et al. (1987) in the Orion nebula. H_2 line emission has also been mapped in various massive outflows, for example, in DR 21 and NGC 2071 (Garden et al. 1990).

Although H_2 is the dominant gaseous component of molecular clouds it is usually difficult to detect directly. This is because of the intrinsic weakness of quadrupole transitions and the negligible rate of collisional excitation at the typical gas temperatures (≤ 100 K) of cold quiescent molecular clouds. Its emission is thus associated with star forming regions where the gas is subject to intense radiation fields and shock waves. Unlike other star formation tracers like CO, the emission lines from H_2 are usually optically thin, which greatly simplifies the radiative transfer modelling in these obscured regions. The line optical depth for an H_2 line is given by

$$\tau_\lambda = \frac{1}{8\pi}\left(\frac{A\lambda^3}{\Delta v}\right)\exp\left(\frac{hc}{k\lambda T_{ex}}\right)N_{upper} \qquad (1.4)$$

where A is the transition probability of a line occurring at wavelength λ, Δv is the characteristic velocity width of the line, T_{ex} is the gas excitation temperature, N_{upper} is the column density of the upper level of the transition, h is the Planck constant and k is the Boltzmann constant. Using the strong 1-0 S(1) infrared transition at 2.122 μm, a typical value for τ can be found,

$$\tau\ (\lambda{=}2.122\mu\mathrm{m}) = 10^{-27}\ N_{upper}[\mathrm{m}^{-2}] \tag{1.5}$$

Hence, a column density of order 10^{27} m^2 is needed to produce an optical depth of unity. Commonly observed column densities are of the order of 10^{22} m^2 or less and therefore these regions are essentially transparent to the H_2 radiation. Therefore, the observation of a line leads directly to a determination of the upper level column density that can then be compared to model predictions for the excitation process at work.

There is a critical density for each level above which that level is thermalised, i.e., for $n > n_{crit}$ the collisional de-excitation by H atoms and H_2 molecules can proceed faster than radiative decay. The critical density for any level of H_2 is given by $n_{crit} = A/C_d$, where C_d (cm^{-3} s^{-1}) is the de-excitation collisional cross section and A (s^{-1}) is the spontaneous decay probability for the transition. Typical H_2 critical densities are of order 10^5—10^6 cm^{-3} because of the slow spontaneous decay rates of most H_2 transitions that are observed in the near-infrared ($A \approx 10^{-7}$ s^{-1}). Immediately we can see the enormous advantage of observing H_2; the levels will be populated according to the well-known Boltzmann distribution for densities as low as a few × 10^5 cm^{-3}, which are easily achievable in the post-shock dense layers. The same is not valid for other molecules such as CO, which has comparatively large decay rates (≈ seconds) and critical densities of order 10^{13} cm^3.

We can now write an expression for the intensity of an H_2 line. The intensity of a line (I_{ij}) is directly proportional to the energy transition gap ($h\nu_{ij}$), the spontaneous decay probability (A_{ij}) and the column of excited molecules in the upper level of the transition (N_i). An additional term is required to account for the foreground dust extinction in the line of sight (τ_{ij}). The observed intensity can be written as

$$I_{ij} = \frac{1}{4\pi} h\nu_{ij}\, A_{ij}\, N_i \exp(-\tau_{ij}) \tag{1.6}$$

The subscripts "ij" refer to a transition between upper level "i" and lower level "j". This formula is used throughout this thesis to calculate the column densities from the observed H_2 line intensities.

1.5 The excitation properties of H_2

Because molecular hydrogen is the main observational tool used in this thesis, the most important aspects concerning its structure and excitation properties are briefly discussed. A complete quantum mechanical description of this molecule can be found in Hertzberg (1950). The energy level structure of molecular hydrogen is displayed in Fig. 1.2. The ground electronic state is subdivided in to fifteen bound vibrational levels which are labelled by the quantum number v. Associated with each vibrational level is a series of rotational levels that are labelled by the quantum number J. The infrared H_2 emission lines that are observed in astronomical objects are due to transitions between the vibrational and rotational levels. The excitation of H_2 requires very energetic phenomena to significantly populate its upper levels due to the molecule low moment of inertia. The lowest rotational level of H_2 lies at 510 Kelvin above the ground state whereas the lowest vibrational level lies at 6000 K. Because of this level separation, the molecule is only excited in regions of energetic activity and thus its emission is often associated with protostellar environments.

The separation between adjacent vibrational levels decreases with increasing v due to the anharmonicity of the electronic potential curve. Because H_2 is homonuclear, i.e., formed out of two identical hydrogen atoms, electric dipole radiative transitions are forbidden. Only electric quadrupole transitions are allowed between the rotational-vibrational levels whose probabilities are hence very small, for instance, the rates of the $\Delta v=1$ transitions are of the order of 10^{-7} s^{-1}. The quadrupole selection rules require that during radiative transitions the rotational quantum number change by 2, 0 or -2. Transitions from (v', J=0) —> (v'', J=0) are excluded but there is no restriction on the change in the vibrational quantum number.

A rotational-vibrational transition is commonly identified by the upper and the lower vibrational quantum number of the transition followed by the letters S(J), Q(J) and O(J) depending on whether the rotational quantum number J of the lower level of the transition is smaller than, equal to, or greater than that of the upper level of the transition. For example, the H_2 emission line at 2.122 μm occurs from a transition from level (v =1, J=3) to level (v=0, J=1). Thus the notation used for this line, 1-0 S(1), reflects the change in vibrational quantum number $\Delta v = 1$ and rotational quantum number $\Delta J = -2$. Transition rates for the vibration-rotation states of the ground electronic state of the H_2 molecule have been calculated by Turner et al. (1977).

The statistical weight associated with each level is a function of the rotational quantum number J and the nuclear spin. Since the two nuclei of the H_2 molecule are identical fermions, only one combination of nuclear spins is possible for each rotational level within an electronic state. In the ground electronic state, all the levels with odd J are nuclear triplet states (ortho-hydrogen), and all levels of even J are singlet states (para-hydrogen). The statistical weight of a level J in the ground state is 3 (2J +1) for odd J and (2J +1) for even J.

1.5.1 Formation of H_2

It is a common belief that H_2 forms on the surfaces of dust grains in dense molecular clouds (Duley et al. 1986; Hollenbach et al. 1971). The reason for this is that the radiative association of two H atoms is forbidden by dipole selection rules. When two H atoms collide with a grain and stick, they migrate and eject an H_2 molecule with substantial kinetic, vibrational and rotational energy (Hollenbach and Salpeter 1971). The formation rate (in units of $cm^{-3}\ s^{-1}$) is written as Rnn(H I), where n and n(H I) are densities of total hydrogen and H I, respectively, and where R is a rate coefficient. Molecule formation occurs for grain temperatures of less than a critical value, $T_{cr} \approx 75$ K; above this value, atoms evaporate from the grain surface before forming H_2 (Duley and Williams 1986). Since the composition and structure of grain surfaces are highly uncertain, it is difficult to calculate the exact value of the rate coefficient R. This coefficient depends on the grain cross section per hydrogen nucleus, the atom grain collision frequency, and the efficiency with which molecules are formed per atom-grain collision.(Hollenbach and Salpeter 1971). For typical gas-to-dust ratios, R ≈ 1-3 × 10^{-17} cm^{-3} s^{-1}. This value is also suggested by the *Copernicus* UV data (Jura 1974).

1.5.2 Heating and cooling by H_2

Molecular hydrogen plays a decisive role in establishing thermal balance of both diffuse clouds (T ≈ 100 K) and shocked molecular clouds (T ≈ 2000 K). The H_2 radiative cooling function has been computed by (Shull et al. 1978, see Fig. 1.3) and recently by (Lepp et al. 1983) using appropriate de-excitation rates for collisions with both H atoms and H_2 molecules. Because of the collisional de-excitation of excited levels, the cooling rate is density dependent. The critical density for de-excitation ranges from $n_{crit} \approx 10$ cm^{-3} for transitions with $J = 2 \rightarrow 0$ to $n_{crit} \approx 10^{4-5}$ cm^{-3} for $J \geq 7$ and most vibrational lines. For $n \geq 10^6$ cm^{-3}, most rotational and vibrational levels are populated in the near-thermal equilibrium and the volume cooling rate (ergs cm^{-3} s^{-1}) is proportional to $n(H_2)$, rather than to the square of $n(H_2)$.

Dissociative cooling is also sensitive to density. Since dissociation is dominated by collisions from high vibrational levels, radiative decay results in a low-density ($n \ll 10^6$ cm^{-3}) dissociation rate orders of magnitude less than the thermal equilibrium values. On the other hand, the heating produced by H_2 depends on the density, temperature, molecular fraction, ionisation fraction and also on the UV and X-ray radiation fields. Collisional de-excitation of levels excited by UV absorption may also transfer energy from the radiation field to the gas.

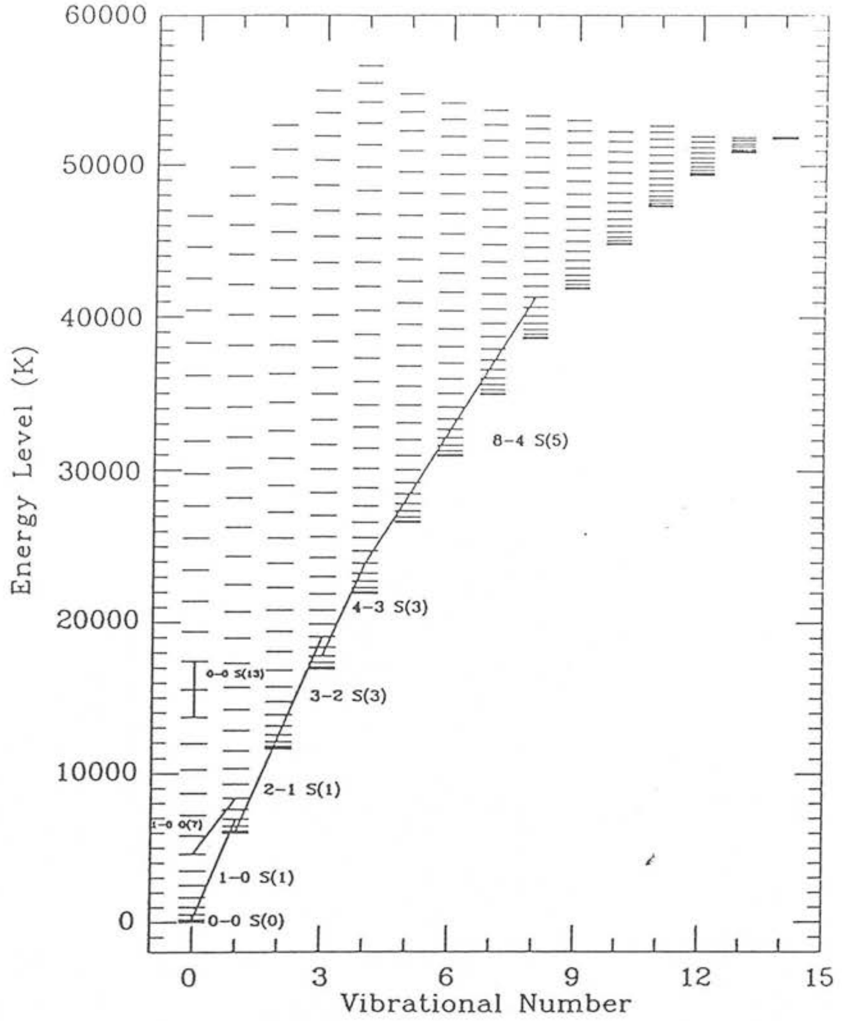

FIGURE 1.2: Energy level structure for the ground electronic state of the H_2 molecule. The x axis displays the vibrational number, from v= 0 to 14. The energy of a specific excited state in level (v, J) is shown by a horizontal dash in the diagram. The y axis is in units of energy T = E/k (1eV = 11600 K). Common transitions that are usually observed, are shown in the diagram by their labels; e.g. 1-0 S(1) line occurring 2.122μm, 2-1 S(1) at 2.248μm, 3-2 S(3) at 2.201μm and the 4-3 S(3) at 2.345μm. See text for an explanation of the label notation for the lines. Adapted from Burton (1992).

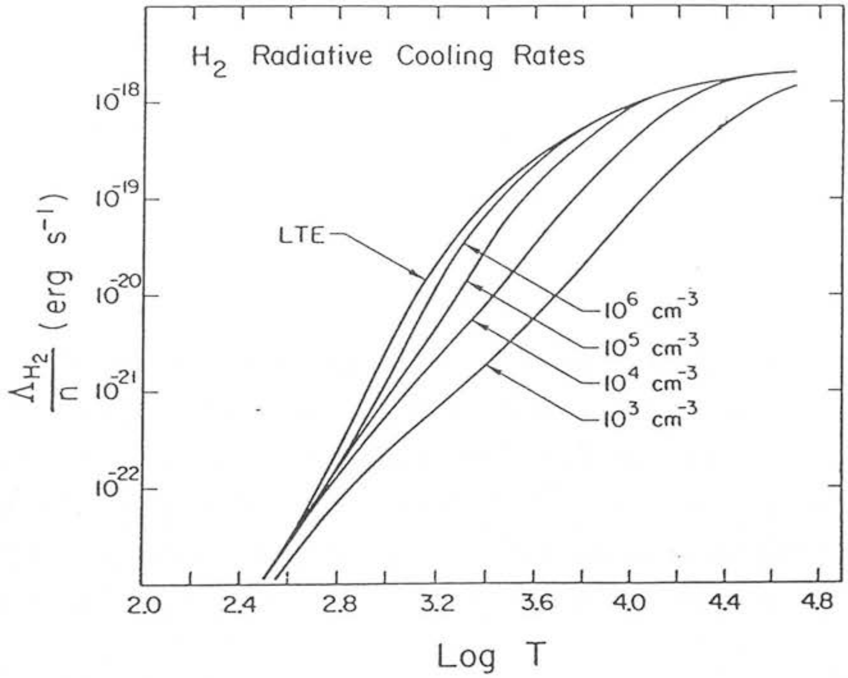

FIGURE 1.3: H_2 radiative cooling rates in a molecular cloud. The cooling is due to the quadrupole transitions from the vibrational and rotational excited states of the molecule. The level population is solved at each temperature for H_2 densities in the range $10^3 - 10^6$ cm^{-3}. The high density limit for which the levels are distributed according the Boltzmann equilibrium is labelled LTE. The non-LTE cooling rates are substantially lower than the LTE values because the levels are populated sub-thermally. Adapted from Shull and Hollenbach (1978).

1.6 Shocks *versus* photodissociation regions

The detection of H_2 in excited rotational, vibrational, or electronic states is a valuable diagnostic of conditions in the interstellar medium once the source of excitation is known. We have seen that both shocks and photodissociation regions are strong emitters in the infrared. Then, how can we discriminate between them on an observational basis? A discussion of the different excitation mechanism is presented in the next two sections followed by a comparison of the various observational line diagnostics often used to discriminate between shocks and PDRs.

1.6.1 Shock excitation

The best studied example of an infrared emission source is Orion. The relative level populations indicate a region in approximate thermal equilibrium with $T \approx 2000$ K, while the line profiles exhibit velocities of up to 150 km s^{-1} (Brand, Toner et al. 1989a). These observations, together with the theoretical considerations of explaining such a source of heating or excitation, have been taken as evidence of shock waves originating in the cores of the Orion molecular cloud.

Early shock models with a plane-parallel geometry were used to explain Orion's data (Hollenbach et al. 1977; Kwan 1977; London et al. 1977). These models were characterised by two parameters: the pre-shock density n_0 (molecules cm^{-3}), and the shock velocity V_s (km s^{-1}). The magnetic field B_0 and fractional ionisation are not meaningful parameters in these single fluid shocks. Collisional dissociation becomes important for $V_s > 15$ km s^{-1} if the density is high enough ($n_0 \geq 10^5$ cm^{-3}). For a frame of reference comoving with the shock, several separate layers can be outlined for the shock structure: (1) the pre-shock zone where the gas ahead of the front is irradiated possibly by a UV precursor; (2) a region where the pre-shock flow is randomised into thermal (translational) energy; (3) the region where the rotational and vibrational levels are collisionally excited and (4) the region in which the post-shock gas is radiatively cooled and compressed. Since the H_2 elastic cross sections are one or two orders of magnitude greater than the inelastic cross sections, region (2) may be considered to be a discontinuity in all the thermodynamical variables. At high densities ($n_0 \geq 10^5$ cm^{-3}), region (3) may also be treated as a discontinuity, in which a thermal population of rotational and vibrational states is produced before the H_2 loses appreciably energy through radiative processes. At low densities, regions (3) and (4) are coincident, since each inelastic collision results in a significant radiative loss.

1.6.2 H_2 fluorescent emission

Molecular hydrogen may also be excited non-thermally in photodissociation regions either by the absorption of UV photons, collisions with high-energy electrons, or by resonance fluorescence of H_2 with Lyα and Lyβ. In these regions, the strength of the UV continuum radiation field is usually parametrised by G_0, the ratio of the external continuum UV flux to the average interstellar flux near 1000 Å (Jura 1974). The infrared emission cascade occurs after the molecule has absorbed UV photons longward of 91.2 nm in lines of the Lyman and Werner bands which produces electronically excited H_2 (Sternberg et al. 1989). The molecule rapidly decays into some vibrational-rotational state of the ground electronic state (about 90% of the time) or to the continuum of the ground electronic state, thus leading to the dissociation of the molecule (occurring approximately 10% of the time). This initiates a cascade of slow quadrupole radiative decays through bound states, v and J, of the fundamental electronic state and thus produces the observed infrared emission. This occurs at a rate of 1 decay per year. The expected H_2 1-0 S(1) / 2-1 S(1) line ratio from a pure fluorescent source is about 2. However, if the density is high enough ($n > n_{crit} \approx 10^5$ cm^{-3}), the effect of collisional de-excitation by H atoms tends to bring the level population to near-LTE. The spectral signature is now modified from the pure fluorescence case and can now resemble a shocked spectrum. This can be seen by comparing Figs. 1.4 and 1.5. These diagrams show the segregation of the H_2 levels when the column density is plotted against upper level energy. In the shock case, all the vibrational levels radiate in LTE, and this is shown by the smoothness of the line connecting all the levels with the characteristic Boltzmann signature.

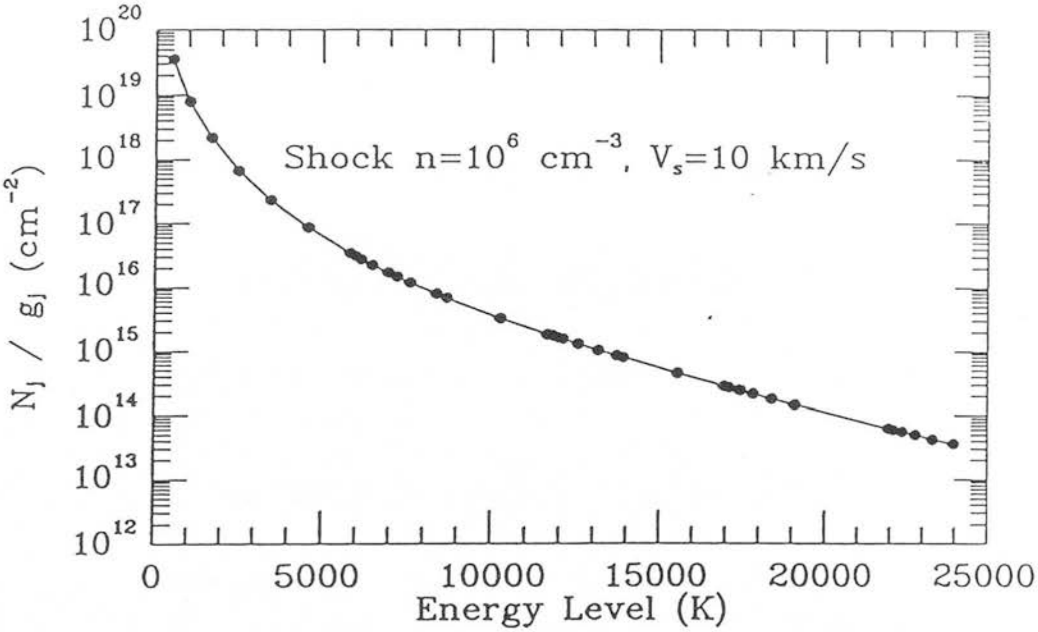

FIGURE 1.4: Plot of H_2 column densities divided by the level statistical weight against upper energy level of the transitions (in Kelvin) for a J-shock model with a pre-shock density $n = 10^6$ cm^{-3}, and for a shock velocity $V_s = 10$ km s^{-1}. Since in a shock the H_2 levels are thermalised, the column densities of the H_2 population follow a smooth curve in this diagram.

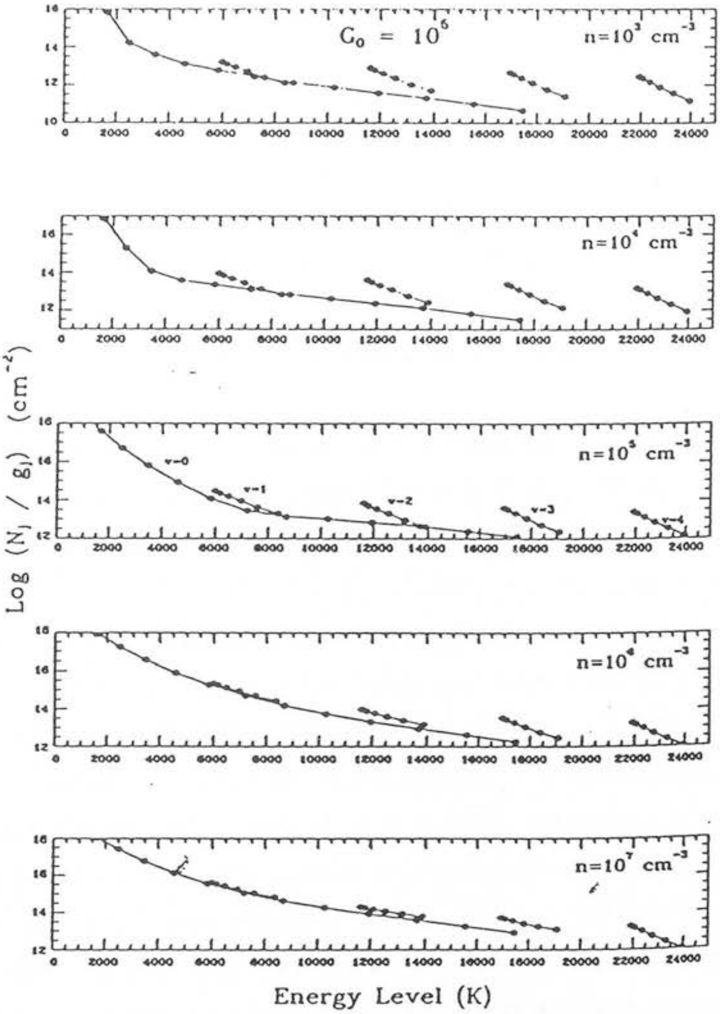

FIGURE 1.5: H_2 column densities predicted from a PDR with $G_0 = 10^5$, as a function of energy level. The five diagrams cover densities of 10^3–10^7 cm^{-3}, and show that in dense PDRs, the lines are pushed towards thermal equilibrium and the spectral signature begins to appear of shocked nature (cf. Fig. 1.4). From Burton et al. (1990).

1.6.3 Emission line diagnostics

The violence of a J-shock produces infrared emission from ionised species ([NeII], [FeII], [SiII], hydrogen recombination lines) that are absent in the spectra of C-shocks. Furthermore, C-shocks feature a much larger column density of moderately high temperature (≈ 1000 K) molecular gas, resulting in a relatively high ratio of far-infrared CO to near-infrared H_2 cooling. Another way of distinguishing J- from C-shocks is from the line profiles. Narrow line profiles are expected from J-shocks since the emission arises from cooling gas that has been accelerated and displaced from the velocity of the quiescent cloud. In C-shocks, a broad emission profile centered on the velocity of the cloud is expected as most of the emission arises from the gas that has just been accelerated (Genzel 1991).

An important indicator of a photodissociation region versus an ionising J-shock is the absolute and relative intensities of the [CII] 158 μm and [OI] 63 μm fine structure lines. Shocks feature weak or no [CII] emission but strong [OI] emission (I[OI] / I[CII] ›› 10). In C-shocks, the [CII] to H_2 line ratio is small because the fractional ionisation must remain low and the gas phase carbon remains in molecular form, with carbon monoxide (CO) being the most abundant molecule. Another commonly used method is the ratio of H_2 2-1 S(1) to 1-0 S(1) line fluxes. A small ratio (≤ 0.1) indicates that the excitation mechanism is of shocked nature. If the ratio is ≥ 0.5, then the emission is ascribed to a PDR. However, this diagnostic can be flawed because the small ratio merely indicates a thermal origin for the emission, a situation that is commonly found in dense ($n(H_2) \gg 10^5$ cm^{-3}) photodissociation regions (Sternberg 1988; Sternberg and Dalgarno 1989). In UV heated regions the populations of molecules in very high lying vibrational levels are enhanced by UV pumping. Therefore, the intensities of lines emitted from high vibrational levels (such as the 6-4 Q-branch lines at 1.6 μm) relative to lines emitted from the v=1 levels are much greater in warm dense PDRs than in non-dissociative shock heated regions where the molecular excitation occurs collisionally (see Table 1.1). Thus, the faint fluorescent emission associated with LTE H_2 emission, is a signature of UV heated gas. Table 1.1 presents a comparison of the diagnostic lines.

TABLE 1.1: Diagnostic line intensity ratios

	1-0 S(1) (2.12μm)	2-1 S(1) (2.25μm)	6-4 Q-branch (1.6 μm)	CII (158μm)	$\frac{\text{CII } 158\mu\text{m}}{\text{OI } 63\mu\text{m}}$
C-shock 20-40 km s^{-1}	$10^{-3} - 10^{-1}$ (cgs)	≤ 0.1	$\approx 10^{-5}$	$\ll 1$	$\ll 1$
J-shock reformation 60-150 km s^{-1}	$10^{-4} - 10^{-3}$ (cgs)	≈ 1	≈ 0.5	≤ 1	≤ 0.1
PDR $G_0 \approx$ few $\times 10^4$ $y_F = 0.01 - 1$	$10^{-4} - 10^{-2}$ (cgs)	≤ 0.1	$\approx 10^{-3}$	1 - 100	≥ 0.1

The range of absolute intensities (in cgs units of ergs s^{-1} cm^{-2} sr^{-1}) of the 1-0 S(1) 2.12 μm line expected from the dense ($n = 10^6$ cm^{-3}) C and J shocks and photodissociation regions is listed in column 2. Line intensities relative to the 1-0 S(1) line are listed in columns 3 through 5. The expected values of the CII to OI fine structure line ratio is listed in column 6. G_0 is the scaling factor that determines the intensity of the far-UV field. It is defined as equal to unity for the average interstellar UV field in the solar neighbourhood. Adapted from Sternberg (1988).

1.7 Motivation and objectives for the thesis

The work presented in this thesis is concerned with the physics of shock waves in molecular clouds, studying the physical processes and the dynamics of the gas. This is accomplished by observing many near-infrared H_2 emission lines arising from the cooling of the gas behind a shock front which propagates into dense molecular material. The main motivation for studying the high-velocity phenomena in shocked molecular gas in these dense interstellar regions is their close association with the star formation process. The extremely broad profiles observed toward star forming regions suggests that many energetic phenomena occurring in the interstellar medium are due to shock waves (Hollenbach et al. 1988). However, there are still some fundamental problems in producing a shock theory that fits all the observations. In particular, there is no general agreement about the physical and chemical conditions in these molecular clouds. Are magnetic fields dynamically important? If they are, how do they affect the shock structure? We have now the means and technology to measure emission lines with a high signal-to-noise ratio to constrain current models of shocked and fluorescent emission. The multi-line spectroscopic study that is presented in this thesis aims to provide an insight into the physical processes in these regions by investigating the near-infrared H_2 emission from two star forming regions. Its ultimate goal is to devise a method to discriminate between J and C-shock structures.

Chapter 2

The structure of shock waves in the interstellar medium

The study of the internal structure of shock waves is of interest for many reasons. From a theoretical point of view, its solutions help to understand the physical mechanism of shock compression in gasdynamics. Also, shock waves are employed in laboratories with the aim of obtaining high temperatures and of studying various processes that take place in gases at high temperatures, as for example, vibrational excitation of molecules, molecular dissociation, chemical reactions, ionisation and radiation processes (Zel'dovich and Raizer 1967). The study of the structure of very strong shock waves in which radiation plays an important role in the dynamics of the cooling gas, is discussed in this chapter and applied to high velocity flows in dense molecular gas clouds. The presence of high magnetic fields changes the structure of the shock and produces a radiatively different signature that can be probed by observations. These magneto-hydrodynamic type of shocks are commonly termed continuous shocks or C-shocks as opposed to the non-magnetic type of jump shocks, or J-shocks.

2.1 Introduction

When a disturbance of increased pressure and appreciable amplitude propagates through a gas, the shock front tends to steepen because the sound velocity is higher in the compressed region. This steepening progresses until a nearly discontinuous shock front is formed. Such shock fronts generally appear whenever supersonic motions are present and must therefore be expected in the interstellar gas, where the cloud velocities are often much greater than the sound speed. In cold molecular gas where the sound speed is small (typically 0.1–2 km s^{-1}) and the magnetic field does not play a major role in the dynamics of the gas, the pressure disturbance will travel faster than the sound speed, thus creating a shock wave. This shock wave then generates a thermodynamically irreversible transition since the dissipative processes (viscosity and heat conduction) within the shock front dramatically increase the entropy of the gas by converting the flow kinetic energy into random thermal motion of the particles. Once shocked, radiation from the excited atoms and molecules behind the shock front will cool the gas as this is compressed to maintain a nearly constant pressure. Compared with strong shocks, $V_s > 50$ km s^{-1}, in dense molecular clouds, $n(H_2) > 10^5$ cm^{-3}, the emission from dust grains is small (Genzel 1991). The study of interstellar shock waves is usually done by observing the radiation from infrared and submillimeter lines of molecules, atoms and ions. When the first near-infrared H_2 emission lines were discovered (Gautier et al. 1976), simple J-shock models were used to explain the line ratios (Hollenbach and Shull 1977; Kwan 1977; London et al. 1977). These models solved the basic hydrodynamic equations (section 2.2) at the shock front and followed the cooling function behind the shock front, from where the emission arises. Further observations of extremely supersonic line profiles, extending up to 150 km s^{-1} (Nadeau and Geballe 1979), together with the inconsistently high model predictions for the CO rotational submillimeter line intensities, created problems for the J-shock model.

A different type of shock was therefore required to account for the new body of data. The idea of a magnetically moderated shock was then introduced (Draine, 1980 ; Chernoff et al. 1982 , Draine et al. 1983). This magneto-hydrodynamic (MHD) shock wave, commonly designated as a C-shock, was introduced to solve the problems associated with the large observed line widths seen in both the H_2 and CO lines, and the very high column densities seen in CO lines. In this type of shock, the ionised gas component (ions and electrons) is coupled to the magnetic field, and changes in the momentum and entropy in the neutral gas are due to friction associated with neutral-ion slip or ambipolar diffusion. The shock front travels at a lower velocity than the Alfven velocity, assuming the ionisation fraction to remain small, which then allows a propagation of a pressure wave ahead of the disturbance. Therefore, the ions begin to accelerate first and subsequently the friction between the ion wave and the neutrals causes gas heating in the leading section of the flow.

Shocks can be classified in two main categories: *radiative* and *non-radiative* or adiabatic. If the post-shock gas can radiate away its energy in a time short compared to the flow time, the temperature drops and the post-shock gas is compressed to maintain approximately constant total pressure, therefore forming a radiative shock wave (Shull and Draine 1987). On the other hand, if the shocked column density of excited molecules is less than the characteristic cooling column density, so that the emitted radiation does not affect the dynamics of the gas, no energy will be lost in the shock front and an adiabatic shock is formed (McKee and Hollenbach 1980). Typical examples of adiabatic shocks occur at the peripheries of young supernova remnants (where the shock velocity is extremely high) and in regions of high velocity stellar winds in early type stars. This thesis is concerned with the study of radiative shocks since these occur more frequently in dense molecular clouds and since both the emitted radiation and the chemistry occurring in these shocks are directly observable.

Shock waves are always compressive, regardless of their structural type. However, the excitation conditions of the shocked layer are quite different for J- and C-shocks, since the emission from the hot shocked gas is sensitive to the dissipational mechanism and the gas cooling function. In this chapter we will discuss the different types of shock structures that are expected in dense molecular gas environments near regions of recent star formation. For simplicity, we will assume that the structure is steady (i.e. $\partial/\partial t = 0$), i.e. the time that takes the fluid to go from the pre-shock initial state to the post-shock state is much shorter than the characteristic times over which the flow variables change in the continuous flow regions behind the shock front. We also adopt a reference frame where the shock front is stationary relative to the observer and limit our analysis to the idealised case of plane-parallel shock fronts ($\partial/\partial y = \partial/\partial z = 0$) propagating through a homogeneous medium of a perfect gas with a constant velocity V_S (see Fig. 2.1).

2.2 Shock front structure

In non-magnetic collisional shocks, the shock front is a discontinuity (McKee and Hollenbach 1980) in which the unshocked and shocked fluids interact by collisions. The shock thickness, λ_s, is of the order of the mean free path in the shocked fluid: $\lambda_s = {}^{1}\!/_{n\sigma}$, where σ is the collisional cross section, and n is the post-shock density (Spitzer 1978). For example, for a typical post-shock density of 10^5 cm^{-3} and a collisional cross section of order 10^{-15} cm^2, the shock thickness is of order 10^{10} cm. In hydromagnetic shocks, the weak coupling between the ions and neutrals will ensure a smooth shock transition in which the slow drift, or ambipolar diffusion, heats the gas through ion-neutral collisional processes. The thickness of this layer can be estimated by balancing the magnetic pressure ${}^{B^2}\!/_{8\pi}$, against the drag force exerted upon the neutrals (Spitzer 1978),

$$\frac{dP}{dt} = \frac{B^2}{8\pi\lambda_s} = n_n n_i m_H \langle \sigma v \rangle V_s \qquad (2.1)$$

in which the relative ion-neutral velocity drift is approximated by V_s because of the ions higher inertia. As the gas cools and compresses downstream from the shock front, the increasing strength of the magnetic field ($B \propto \rho$) forces the ions upstream. Thus, there is a net drag force directed upstream which causes the neutrals to decelerate through collisions. The characteristic length scales, L_n and L_i, over which the neutrals and ions are significantly decelerated are typically $L_n = 2L_0/M$ and $L_i = L_0/M^2$ (Smith and Brand 1990a), where $L_0 = 1/n_i\sigma$, and M is the neutral Alfven Mach number defined as $M = V_s/c_0$, (c_0 is the sound speed). For typical values; M = 3, n = 3×10^6 cm^{-3} and ionisation fraction of 3×10^{-7}, the neutral length scale is $\approx 4 \times 10^{14}$ cm (Smith et al. 1991b).

2.3 Survival of H_2 in a shock

One important question which should be addressed is how fast can shocks propagate through the dense interstellar gas without dissociating the molecules. The speed to which H_2 can be driven by a J-shock has been calculated under various conditions. At high densities ($n > 10^4$ cm^{-3}), collisional dissociation provides a limit of ≈ 22 km s^{-1} for hydrodynamic shocks (Kwan 1977). A similar value was also found by London et al. (1977) of ≈ 21 km s^{-1} in the high density regime. This limit is imposed by the property that ≈ 4.48 eV are removed from the gas each time a molecule dissociates. This velocity can be roughly estimated by equating $0.5m(H_2)V_s^2 = 4.48$ eV and assuming that the dominant cooling mechanism is dissociation. For the high density hydromagnetic shocks, with a field strength $B = 0.8\,(n_0)^{0.33}$ μG, a limit of ≈ 25 km s^{-1} still holds (Hollenbach and McKee 1980). In the low density regime, the speed limit was found to be higher, reaching ≈ 50 km s^{-1} for $n < 500$ cm^{-3} and an Alfven speed of ≈ 10 km s^{-1}. The speed limit is then no longer provided by collisional dissociation but by electronic dissociation, important only when the post-shock temperature reaches $T \approx 5 \times 10^5$ K, or $V_s > 50$ km s^{-1} (Hollenbach and McKee 1980). On the other hand, in C-shocks the speed limit increases with the field strength (Draine et al. 1983; Smith and Brand 1990a). The limit is now imposed by the relative drift velocity between the streaming ions and the neutrals. Complete dissociation of H_2 will be attained for $V_{crit} = (V_i - V_n) \geq 40$–50 km s^{-1} (Draine et al. 1983). This can be seen in Table 2.1, which shows the critical speed to which H_2 can be accelerated without wholesale dissociation.

TABLE 2.1: Critical shock speed: V_{crit}

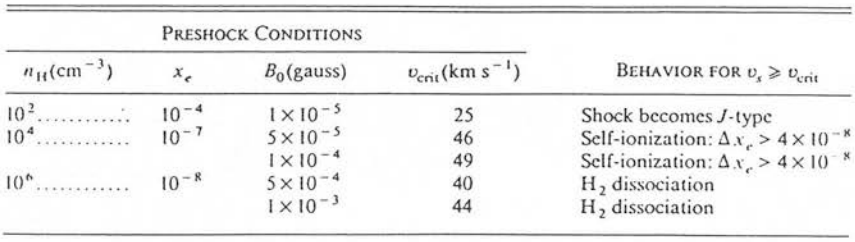

PRESHOCK CONDITIONS				
n_H(cm^{-3})	x_e	B_0(gauss)	v_{crit}(km s^{-1})	BEHAVIOR FOR $v_s \geqslant v_{crit}$
10^2...........	10^{-4}	1×10^{-5}	25	Shock becomes J-type
10^4...........	10^{-7}	5×10^{-5}	46	Self-ionization: $\Delta x_e > 4 \times 10^{-8}$
		1×10^{-4}	49	Self-ionization: $\Delta x_e > 4 \times 10^{-8}$
10^6...........	10^{-8}	5×10^{-4}	40	H_2 dissociation
		1×10^{-3}	44	H_2 dissociation

2.4 J-shocks

High velocity gas dynamic J-shocks dissociate most molecules and ionise atoms. The hydrodynamic structure of a plane-parallel strong shock is shown in Fig. 2.1. It illustrates the typical jump in the gas variables, temperature, density and velocity at the shock front transition. The subscript "0" refers to the properties ahead of the shock and V_S is the speed of the upstream gas relative to the shock. In the shock frame, the pre-shock gas approaching from the left is irradiated by the photons emitted from the hot shocked gas. This radiation can heat and pre-ionise the pre-shock gas – radiative precursor – and change the pre-shock conditions in such a way (greater ionisation implies smaller Alfven speed) that the stability and continuity of the C-shock front is directly dependent on the effect of this radiation (see section 2.5.3.1).

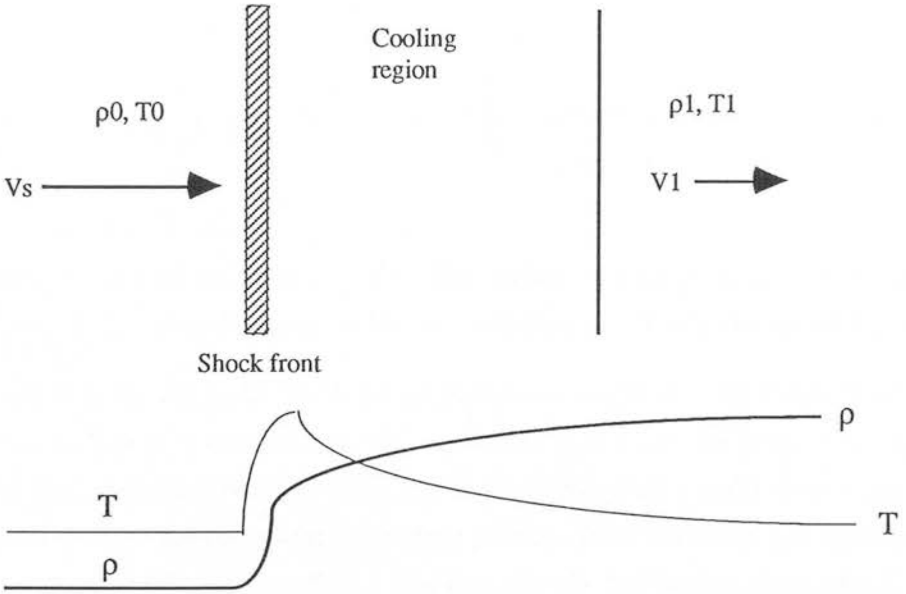

FIGURE 2.1: Schematic diagram of a radiating shock. In the upper diagram the fluid is shown moving from left to right. As the fluid crosses the shock front, it undergoes a discontinuous jump in density and temperature, and reaches the maximum temperature just behind the front by converting flow kinetic energy into random thermal motion of the particles. The changes in temperature and density are indicated schematically in the lower figure.

The adiabatic shock theory involves solving the fundamental equations of fluid dynamics and can be applied to molecular flows (Landau and Lifshitz 1987). These equations provide the solution for the thermal structure behind a shock and are therefore essential for determining the excitation conditions in the shocked gas. At the shock transition, mass and momentum are conserved, and if the shock front is adiabatic (non-radiative), energy will also be conserved across the shock front. In the shock front reference frame the fluid equations valid at any point in the flow can be written as,

$$\frac{d}{dx}(\rho v) = 0 \tag{2.1}$$

$$\frac{d}{dx}\left(\rho v^2 + P + \frac{B^2}{8\pi}\right) = 0 \tag{2.2}$$

$$\frac{d}{dx}\left[\rho v\left(\frac{1}{2}v^2 + \frac{P}{\rho} + E_{int} + \frac{B^2}{4\pi\rho}\right)\right] = \text{Heating} - \text{Cooling} \tag{2.3}$$

where ρ, v and P are the gas density, velocity and pressure, respectively; $E_{int} = \frac{1}{\gamma - 1}\frac{P}{\rho}$ (for a perfect gas) is the internal energy density and γ is the adiabatic index and B is the magnetic field. These equations are correct for single fluid flows, where the velocity is common to every particle in the gas. In C-shocks, the ionic flow attains a different velocity from the neutrals and thus a multi-fluid treatment is required. For that, we can write separate equations for the neutral gas and the ionic component with additional equations that describe the ion-neutral interaction.

2.4.1 Rankine-Hugoniot conditions

The temperature, density and velocity just behind the shock are given by the solution of the conservation equations (2.1–2.3). The flow variables ahead of the shock (subscript 0) and behind (subscript 1) are then related by the laws of conservation of matter and momentum,

$$\rho_0 V_s = \rho_1 v_1 \tag{2.4}$$

$$P_0 + \rho_0 V_s^2 = P_1 + \rho_1 v_1{}^2 \tag{2.5}$$

and the energy equation becomes,

$$\frac{d}{dt}\left(\sum_k h_k + \frac{1}{2}v^2\right) = -\frac{\Gamma}{\rho} \tag{2.6}$$

where h_k is the enthalpy per species k, and the summation is over the species H, H_2 and He, being the only species that contribute significantly to the left hand side of equation (2.6) (Brand 1991) and Γ is the rate of energy loss per unit volume. Together with the equation of state $P \propto \rho^\gamma$, the equations (2.4) and (2.5) can be manipulated to give the relationship between pre- and post-shock values. In a perfect gas where B=0, the large scale properties of a shock can be described by two ratios ρ_0/ρ_1, P_0/P_1 and the maximum temperature reached behind the shock front :

$$\frac{\rho_0}{\rho_1} = \frac{v_1}{V_s} = \frac{\gamma - 1}{\gamma + 1} + \frac{2}{\gamma + 1}\frac{1}{M^2} \tag{2.7}$$

$$\frac{P_1}{P_0} = \frac{2\gamma}{\gamma + 1}M^2 - \frac{\gamma - 1}{\gamma + 1} \tag{2.8}$$

$$T_{max} = \frac{2(\gamma - 1)}{(\gamma + 1)^2}\frac{\mu m_p V_s^2}{k} \tag{2.9}$$

M is the Mach number : $M = V_s / C_s$

where μm_p is the mass per particle and k is the Boltzmann constant. For the simple case of a strong shock with $M \gg 1$, the thermal pressure P_0 is negligible compared with the ram pressure $\rho_0 V_s{}^2$. The compression ratio is then limited to a value of 4 for $\gamma=5/3$ and the velocity drops by the inverse of that value by conserving mass (equation 2.7). The pressure just behind the shock is $P_1 = 3/4\ \rho_0 V_s^2$ (equation 2.8), while further downstream it equals the ram pressure $\rho_0 V_s^2$. So, the post-shock relaxation layer can be considered as isobaric for most computation purposes. T_{max} is the temperature reached behind the shock (for molecular gas $\mu m_p = 0.6 m_H$; equation 2.9),

$$T_{max} = 5.3 \times 10^5 \left(\frac{V_s}{100 \text{ km s}^{-1}}\right)^2 \text{ Kelvin.} \tag{2.10}$$

For example, a fast dissociating shock travelling at a velocity $V_s = 30$ km s^{-1} will attain a maximum temperature of ≈ 48 000 K whereas a partially dissociative shock ($V_s < 22$ km s^{-1}) will have a maximum temperature < 25 000 K.

2.4.2 The gas cooling function

As we have assumed the pre-shock gas to be molecular, with 10% of helium by number, the primary coolant will be H_2 dissociation in the hottest part of the flow and H_2 line emission from the cooler region ($T \leq 3000$ K) downstream from the shock. For shocks that completely dissociate H_2 ($V_s > 22$ km s^{-1}), the gas cools by recombination radiation of atomic lines while farther downstream, the re-formation of H_2 molecules on the surfaces of dust grains provides an extra source of heating at about 400 K (the re-formation plateau) and subsequently cools down by line emission (McKee and Hollenbach 1980). Other important coolants are the rotational and vibrational lines of CO and H_2O. The physical conditions behind the shock are well described by the Boltzmann equilibrium because the density is high and collisions proceed at a faster rate than radiative transitions. The H_2 line cooling function can be approximated by (Burton 1986),

$$\frac{\Gamma}{n(H_2)} = \begin{cases} 2.59 \times 10^{-42}\, T^{4.66}, & 200 \text{ K} < T < 2000 \text{ K} \\ 2.03 \times 10^{-25}\, e^{-7700/T}, & 2000 \text{ K} < T < 20000 \text{ K} \end{cases} \tag{2.11}$$

and is given in units of Watts per molecule. The dissociation cooling is taken from Roberge & Dalgarno (1982) and can be written as,

$$\frac{\Gamma_d}{n(H_2)} = E_d\,R = E_d\left[n(H)\langle\sigma v\rangle_H + n(H_2)\langle\sigma v\rangle_{H_2}\right] \qquad (2.12)$$

where E_d is the energy released to the gas for every dissociation of an H_2 molecule (E_d = 4.48 eV) and $\langle\sigma v\rangle_H$ and $\langle\sigma v\rangle_{H_2}$ are the rate coefficients for collisions with H atoms and H_2 molecules, respectively. An analytic expression for R can be obtained by fitting the curves presented by Roberge and Dalgarno (1982):

$$R = 8.7 \times 10^{-9}\, n_{tot} n(H_2) e^{-54700/T} \quad \mathrm{cm^3\ s^{-1}} \qquad (2.13)$$

The cooling profile in a partially dissociative J-shock is displayed in Fig. 2.2. Note how dissociation of H_2 dominates when the temperature is near the maximum. Also, from this graph we can see that H_2O is the dominant coolant after the temperature has come down to about 4000 K. The strong cooling by H_2O molecules completely dominates the emission signature from J-shocks and is in conflict with the observed H_2 line ratios (Brand et al. 1988). Hence, it is necessary to reduce significantly the abundance of water in the J-shock models to produce a good fit to the observed H_2 line intensities. Below ≈ 3000 K, the gas cools by line emission from H_2 and CO. Fig. 2.3 shows the dissociated fraction attained in the post-shock relaxation layer for various shock values of pre-shock density and velocity. The plot is only accurate for densities greater than about 10^5 cm^{-3}, which is when the gas reaches LTE.

2.4.3 The H_2 emission spectrum

The emission spectrum expected from a partially dissociative J-shock is different from that of a dissociative shock because in this case the emission arises from reformed H_2. Since the gas cools to about 4000 K by H_2 dissociation regardless of the shock speed (which determines T_{max}), the H_2 emission spectrum is purely determined by the shock pressure and the nature of the coolants. Fig. 2.4 elucidates this point by showing the column density (proportional to line emission) expected from the H_2 1-0 S(1) line for several densities and shock speeds. The intensity of this line is dependent on the shock pressure but is independent on the shock speed. This implies that provided the shock is hot (fast) enough, the H_2 line ratios are purely determined by the shock pressure and the cooling function, which define the run of column density versus level of energy.

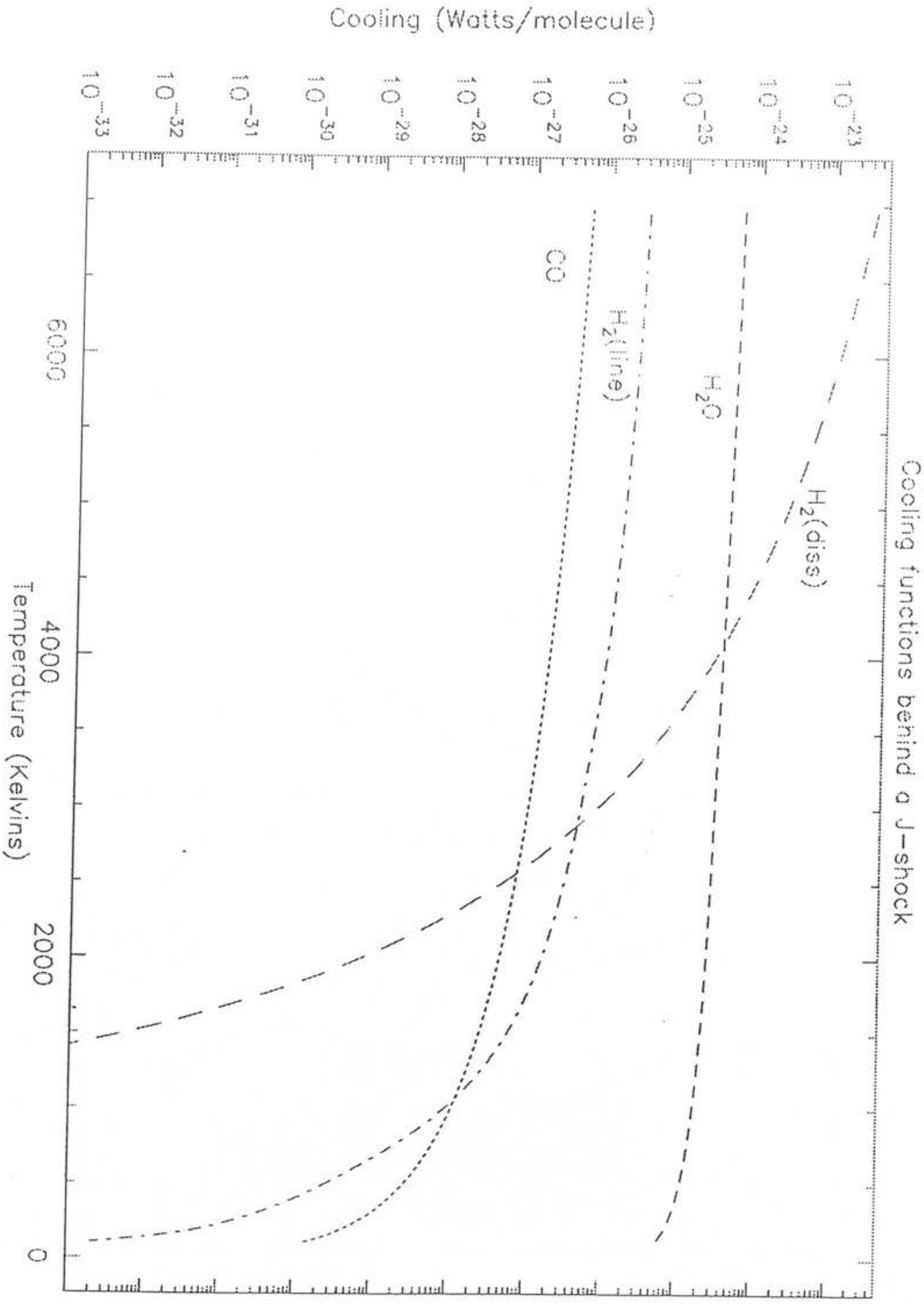

FIGURE 2.2: Cooling function behind a partially dissociative J-shock. The shock front is at left of the diagram. Several molecules, H_2, CO and H_2O provide the cooling in the post-shocked layers. Cooling by H_2 dissociation dominates at high temperatures while at lower temperatures the main coolant is H_2O or H_2 and CO line emission if the water abundance is negligible.

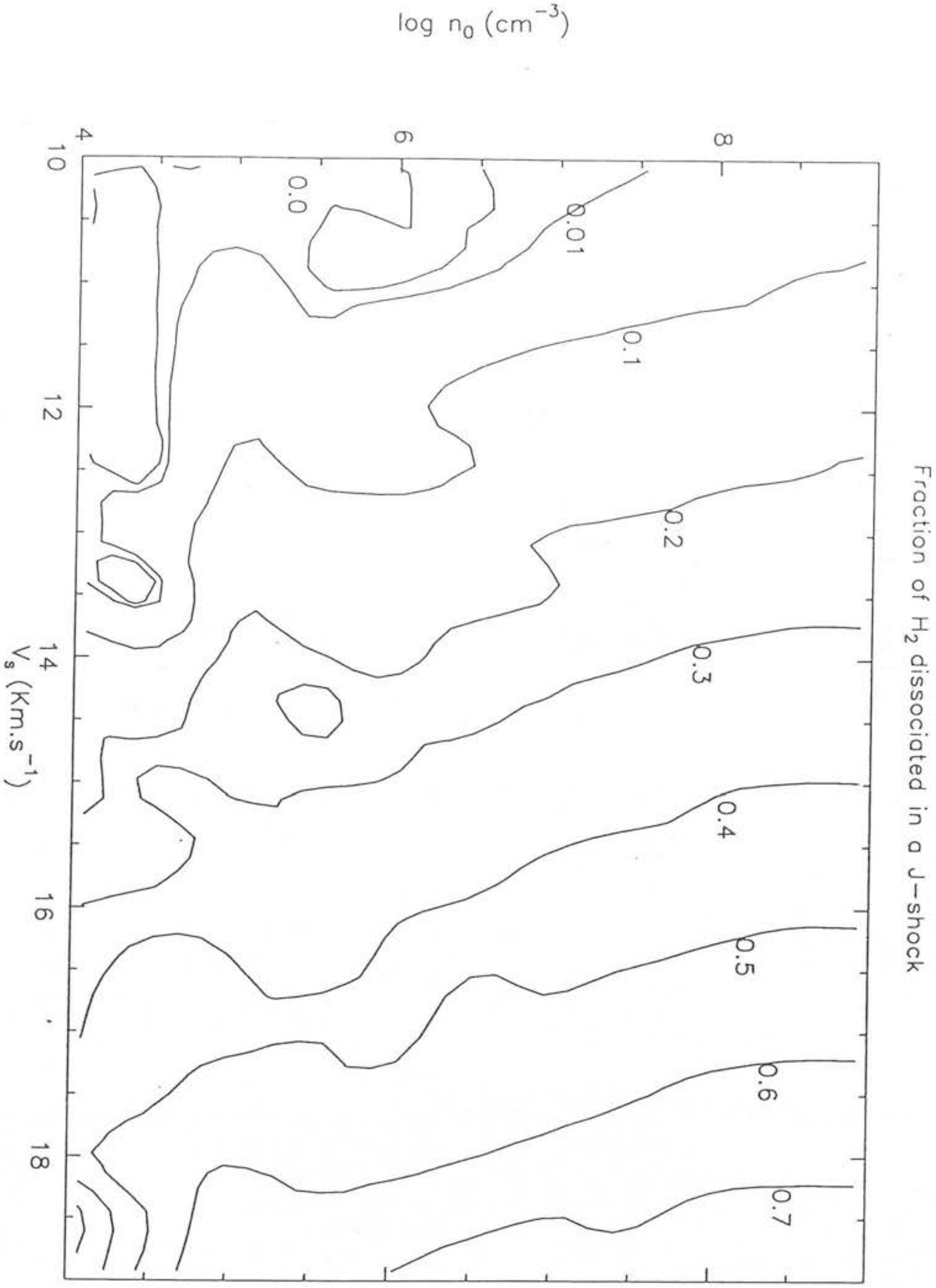

FIGURE 2.3: Contour plot of the dissociated fraction in a partially dissociative J-shock for gas in Boltzmann equilibrium for different shock speeds. Strong shocks ($V_s \approx 18$ km s^{-1}) will dissociate more molecules and therefore produce less H_2 line emission.

To calculate the H_2 line emission, we first assume that the gas is in Boltzmann equilibrium locally. Then, the number of molecules in any state (i) is given by,

$$n_i \propto g_i \exp\left(-\frac{E_i}{kT}\right) \tag{2.14}$$

where g_i is the degeneracy of level (i) and E_i (= kT_i) is the level's energy. If the partition function is Q(T) and for an ortho to para ratio of 3 to 1, an approximation for Q(T) is (Brand 1993),

$$Q(T) = \sum_i g_i \exp\left(-\frac{E_i}{kT}\right) \approx \frac{T/39.5\ \mathrm{K}}{1 - \exp(-6000/T)}\,. \tag{2.15}$$

Then, the level population in level (i) is determined by,

$$n_i = \frac{n(H_2)\, g_i \exp\left(-\frac{T_i}{T}\right)}{Q(T)} \tag{2.16}$$

The observed column density through the shock is given by summing n_i in the line of sight,

$$N_i = \int n_i\, dx \tag{2.17}$$

and since the element length through the shock is $dx = v\, dt$,

$$\frac{N_i}{g_i} = \int \frac{n(H_2)\, v \exp(-T_i/T)}{Q(T)}\, dt \tag{2.18}$$

Now, using the cooling function (section 2.4.2) to substitute dt in equation (2.18), $dT/dt = f(\Gamma, \Gamma_d)$, we get after some algebraic manipulation,

$$\frac{N_i}{g_i} = k n_1 V_s \int \Phi(T) \frac{\exp(-T_i/T)}{Q(T)\, \Gamma/n_p} dT \tag{2.19}$$

In the above, the constancy of $nv = n_p V_s$ has been used. $\Phi(T)$ is a function of the fractional ionisation, which changes through the shock. This expression (equation 2.17) can be further approximated (Brand et al. 1988) to yield,

$$\frac{N_i}{g_i} \propto T_i^{-s} - (T_i + 6000)^{-s} \tag{2.20}$$

where s is the local temperature exponent of the cooling function (see equation 2.11). It is clear from this approximation that the column density depends on the cooling function through the exponent s, and on the energy level in question, but not on maximum temperature, shock speed or density, except that the density must be sufficiently high to maintain the Boltzmann equilibrium. Since dissociation cooling depends on density squared while line cooling depends only on density (for $n > n_{crit}$, i.e. in LTE), shocks at a given speed in low densities will cool less by dissociation of H_2, and a greater column density at high temperatures will result. Hence, the slope of the derived column density versus energy of the upper level of the H_2 lines will be less negative for the emission from low density shocks. This slope can then be used as a barometer in partially dissociative J-shocks. For velocities greater than ≈ 22 km s^{-1}, dissociation goes to completion and no hot H_2 emission will be expected because of the low temperatures of the reformation layer ($T < 500$ K). This is in contrast to what has been observed (Fig. 2.5) by Brand et al. (1988) in OMC-1.

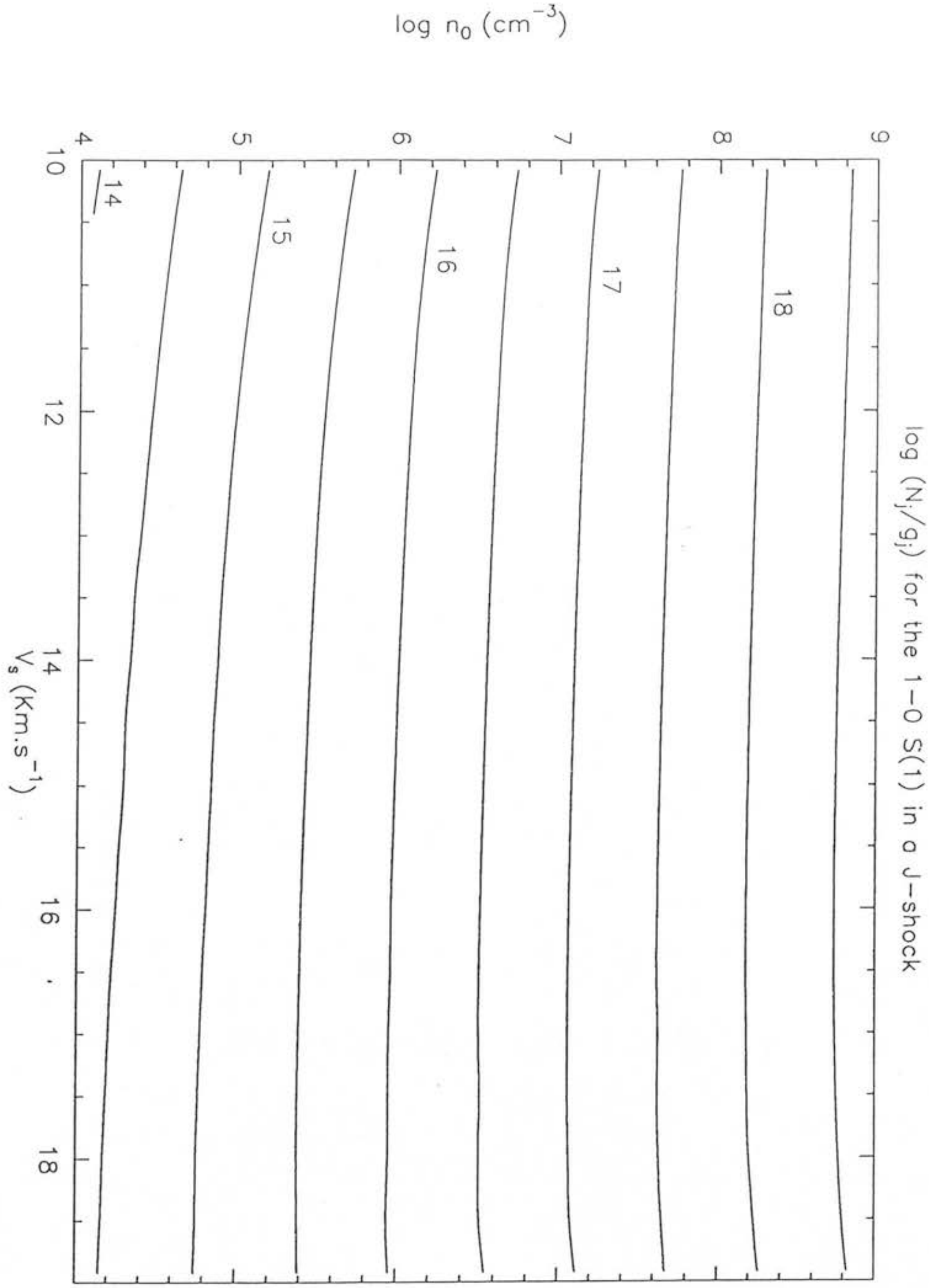

FIGURE 2.4: Logarithmic plot of the column density for the 1-0 S(1) line of H_2. It is shown that for most of the parameter space in velocity the predicted intensity (or column density) is nearly constant for a specific pre-shock density n_0, and thus the model is independent of shock speed.

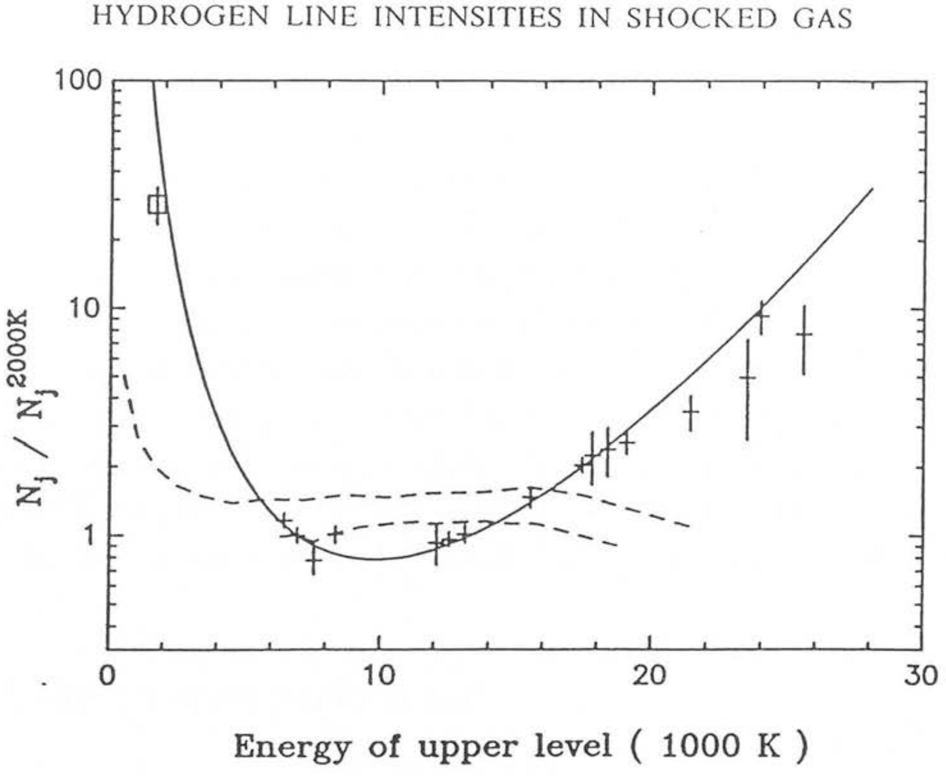

FIGURE 2.5: Column density diagram for the Orion OMC-1 data (Brand et al. 1988). The ratios of the observed, dereddened H_2 emission column densities are normalised in this diagram to the 1-0 S(1) line and divided by those of a Boltzmann distribution at 2000 K. The choice of this normalisation is intended to show the deviation of the data from a single temperature environment, which would be a straight line in the diagram.

2.4.4 Difficulties with the J-shock model

2.4.4.1 H_2O abundance

The simple model described above was used by Brand et al. (1988) to calculate the H_2 spectrum of non-dissociative shocks. A more complex code to treat hydrodynamic J-shocks has been produced by Hollenbach & McKee (1989) and incorporates a substantially elaborate network of chemical reactions which models the compressed and hot post-shock relaxation layer. Particularly important in these models is the formation of H_2O, which can dominate the cooling for pre-shock densities of $n_0 \geq 10^5$ cm^{-3}. It is clear from Fig. 2.2 that the H_2O abundance in J-shocks will greatly influence the H_2 excitation state deduced from a J-shock. Fig. 2.6 shows the prediction for a J-shock travelling at V_s =15 km s^{-1} into gas of density n=10^8 cm^{-3}. The curves are for different H_2O abundances: 0 (full), 10^{-6} (short-dashed), and 10^{-5} (long-dashed). From this we can see that, unless H_2O emission can be considered negligible, the good agreement between the observed H_2 line ratios in OMC-1 and the J-shock model is lost. Since all gas phase oxygen that is not converted into CO is bound to form H_2O in the warm post-shock gas (Draine 1991), this presents some problems to the *no-H_2O* J-shock models. Despite this, as argued by Brand et al. (1988), the *no-H_2O* J-shock model still provides the best fit to the observed H_2 spectrum in a number of sources, and especially in the bright source OMC-1.

2.4.4.2 Velocity profile widths

The extremely supersonic speeds observed in shocked H_2 regions also pose a serious problem to the applicability of J-shocks (Nadeau and Geballe 1979). The velocity profiles predicted by these models are intrinsically narrow whereas observations of the OMC-1 shock (Brand et al. 1989a; Moorhouse et al. 1990b) show emission extending up to widths in excess of ≈ 140 km s^{-1} in several high excitation lines (Fig. 2.6). These large widths are impossible to explain with planar shocks. An investigation of hydromagnetic J-shocks has been carried out by Smith (private communication) who found that fast bow shocks possess an oblique tail where most of the H_2 emission comes from. For these paraboloidal surfaces, a significant fraction of H_2 emission of low excitation is produced where the normal shock speed is in the range 8–10 km s^{-1} which reduces the total excitation temperature. The OMC-1 data can be modelled with $n_0 = 10^7$ cm^{-3} and a shock produced H_2O abundance of $\approx 3 \times 10^{-5}$. However, this still falls short by about an order of magnitude of the assumed solar abundances (Hollenbach and McKee 1989).

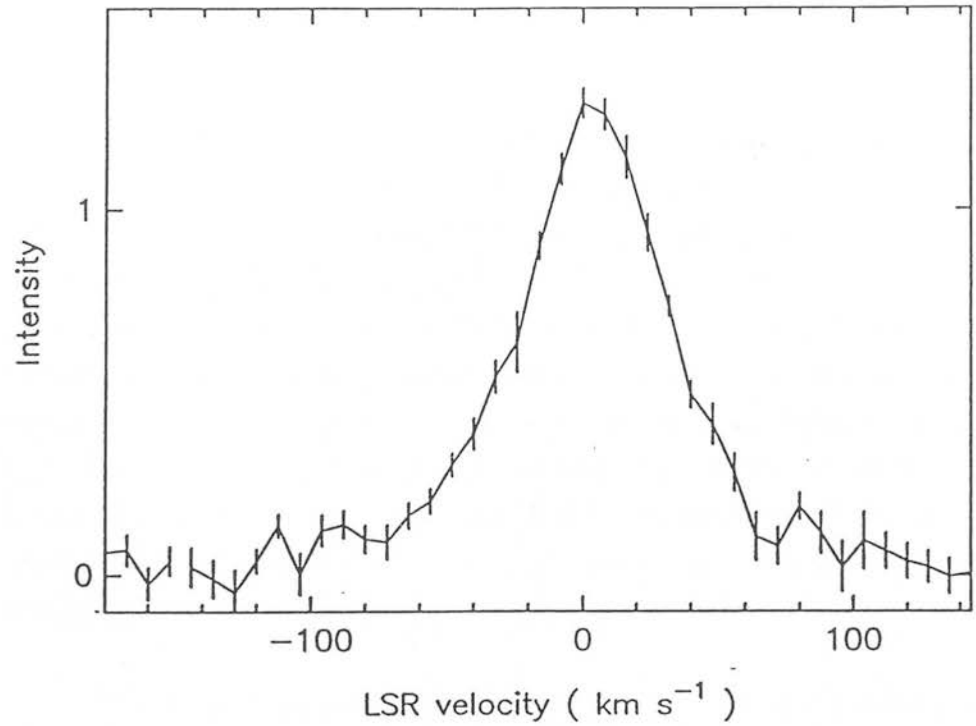

FIGURE 2.6: Velocity profile of the 1-0 S(1) line of H_2 observed in OMC-1 (Brand et al. 1989a).

2.4.5 Hydromagnetic J-shock — Magnetic precursors

A hydromagnetic J-shock occurs as a result of the steepening of a compressional wave. This is also a jump shock – the discontinuous change in the flow speed and temperature that represents the fact that a thin shock front exists through which energy of bulk motion is dissipated into thermal energy. The magnetic field is assumed to be frozen-in to the gas so that the gas cannot cross field lines (Smith 1991b) and hence, the magnetic field is compressed with the gas (Spitzer 1978) :

$$\frac{B_0}{\rho_0} = \frac{B_1}{\rho_1} \tag{2.21}$$

The bulk energy lost is partially converted into magnetic energy, which softens the impact of the thermal component. If the ionisation level is low, strong cushioning is possible for the neutrals through fast ion-magnetosonic waves and ion-neutral collisions. The J-front is then preceded by a *magnetic precursor* in which the neutrals are pre-heated (Draine 1980). Its structure can be characterised by a leading C-shock section followed by a strong J-front. If the precursor is sufficiently strong and provided the shock speed is below some critical value, the shock reverts to C-type (Draine et al. 1983). Magnetic precursors to $V_s \approx 100$ km s^{-1} shocks have been proposed to explain the origin of the shocked H_2 emission from Herbig-Haro objects (Hartigan et al. 1989) and also from several filaments in the Cygnus Loop supernova remnant (Graham et al. 1991).

The magnetic precursor model effectively increases the limiting breakdown speed from ≈ 22 km s^{-1} to about 40–50 km s^{-1} (Chernoff and McKee 1990; Smith and Brand 1990a). Although this model seems to offer an attractive explanation for the observed broad velocity profiles in some sources, there are still some problems the model fails to explain. Firstly, the large streaming velocities $\approx V_s/2 \geq 50$ km s^{-1} predicted seem to be extremely large and close to the critical ionisation velocity (Draine and McKee 1993). Thus, it is possible that precursors to such fast shocks will be truncated by the breakdown speed once $(V_i - V_n)$ reaches ≈ 40 km s^{-1}. Secondly, the Alfven speed for the charged particles $(\rho_n/\rho_i)^{0.5} v_A$ has to exceed V_s at the leading edge of the precursor which requires the fractional ionisation to remain very low. These conditions seem to be realised for shock speeds $V_s \geq 100$ km s^{-1} and thus raises several questions about the significance of the magnetic precursor. Future work on the heating, chemistry and ionisation in the precursor region will help to clarify this situation.

2.5 C-shocks

Early observations of extremely broad 1-0 S(1) line profiles, with emission at $V_s > 100$ km s^{-1} (Nadeau and Geballe 1979), have prompted the development of magnetically moderated (continuous) C-shock models (Chernoff et al. 1982; Draine 1980; Draine et al. 1983). This type of shock introduces the soft shock transition, in which changes in the momentum and entropy take place via drag friction with a magnetically coupled ionised component. This coupling between both fluids is due to the elastic scattering between ions and neutrals, charge exchange and scattering by charged dust grains (Draine and McKee 1993). The ion-neutral slip (ambipolar diffusion) provides a frictional mechanism that converts the flow kinetic energy of the upstream fluid into heat at a rate which (because of the low ionisation level) is low enough that the radiative cooling may be able to maintain the fluids at temperatures far below the temperature which would have been attained in the absence of cooling. Thus, the molecules can now be accelerated to higher velocities without being thermally dissociated. A useful approximation for which we can derive meaningful parameters, is that of cool C-shocks (Smith and Brand 1990a). In these shocks the gas remains cool relative to the J-shock of equivalent velocity in which rapid heating occurs. In this case, $kT_n \ll m_n V_s^2$ and the momentum equation reads :

$$\frac{d}{dx}\left(n_n m_n v_n^2 + \frac{B^2}{8\pi}\right) = 0 \tag{2.22}$$

Integration of this equation yields a simple formula that relates the ion and neutral velocities in the flow (Smith and Brand 1990a),

$$\frac{v_n}{V_s} = 1 + \left[1 - \left(\frac{v_i}{V_s}\right)^{-2}\right]\frac{1}{2M_A{}^2} \tag{2.23}$$

where $v_i/V_s = B_0/B$ with B_0 being the undisturbed field strength. From this we can derive the maximum streaming speed in a cool C-shock :

$$\frac{v_{ni}}{V_s} = 1 + \frac{1}{2M_A^2} - \frac{3}{2M_A^{2/3}} \qquad (2.24)$$

Thus the amount of heating, which is proportional to the square of the drift velocity, can be estimated. High streaming speeds in excess of $0.7V_s$ are possible for $M_A >$ 12. The nature of a C-shock significantly changes with Mach number. High Mach numbers imply that only a few collisions are necessary to reduce the flow momentum. This is shown in Fig. 2.7, where the upper diagram (Fig. 2.7a) represents the behaviour of a low Mach number shock and the lower diagram (Fig. 2.7b) represents a high M_A shock. If the field pressure (nkT) is comparable to the thrust ($n_n m_n V_s^2$), the neutral deceleration must closely follow the field compression (Fig. 2.7a). On the other hand, if the flow is *cool*, i.e. highly supersonic, then a large change in the field is necessary to produce a small change in the thrust and both the field and ion density are considerably amplified upstream (Fig. 2.7b).

The temperature profile is nearly flat topped in a C-shock because the heating rate initially grows (due to differential velocity between ions and neutrals) and then decreases with time since cooling competes with the heating throughout the C-front. This single temperature environment for C-shocks is in contrast to the range of temperatures that can be achieved behind a J-shock front. Then, the peak post-shock temperature in C-shocks increases with shock velocity to temperatures of order 4000 K (or $V_s \approx 40$ km s^{-1}) so that the distribution of column densities of H_2 is velocity dependent. For velocities exceeding ≈ 40 km s^{-1}, the H_2 dissociates and the C-shock breaks down to form a dissociative J-shock. The predicted line widths are still narrow (typically half the shock velocity) if H_2O dominates the cooling (Smith and Brand 1989). Although H_2 cooling produces wider emission lines (typically 90% of the shock velocity), these models are still constrained by the limit on the breakdown speed of ≤ 45 km s^{-1}. These properties appear to rule out planar C-shocks in virtue of the observed range of temperatures and excitation conditions (Brand et al. 1988; Moorhouse et al. 1990b).

2.5.1 Bow shocks

The development of a theory for bow shock structures has been suggested by the observations of the morphology of some shocked sources, especially Herbig-Haro objects. This configuration is shown schematically in Fig. 2.8. In this bow structure, the shock strength varies along the bow surface and the shocked gas is refracted downstream. At the head of the bow, the molecular gas may be completely dissociated because there the shock normal is at a maximum. Further downstream in the bow wings, the shock obliquity increases, which softens the impact, and the gas reaches only moderate temperatures. A range of temperatures within the observed aperture beam can now be achieved if we observe the bow as a whole and thus we sample a large range of shock speeds. In bow J-shocks the velocity deflection down in the wings appears to be too small to detect and does not provide the observed large range in velocity in the line of sight (Brand 1993).

It is possible to find a geometric shape that fits the observed H_2 line ratios and provides a large velocity range if the magnetic field is high enough (Smith and Brand 1990b). Several bow shock geometries have been investigated such as paraboloids, hemispherical caps and cones and their emission properties calculated. The extension from planar C-shocks to bow C-shocks can be summarised :

- A planar approximation is assumed to be valid locally, i.e. the bow size is considered to be greater than the cooling length for the warm H_2. The typical sizes found for Herbig-Haro bow structures are a few × 10^{16} cm and these are normally sufficiently large to treat them with the planar element analysis (section 2.2);

- The breakdown speed is a function of the angle between the field and the shock normal, so that it varies from location to location on the bow surface;

- Although generally the magnetic field is not perpendicular to the shock front, a scaling law can be used to replace the oblique shock front with a perpendicular one that has the same expected properties. A simple law of the form $B_{\perp} = B\left(\sin \zeta\right)^{\tau}$ with $\tau = 0.5$ has been suggested by Wardle & Draine (1987).

2.5.2 H_2 line strengths

The calculation of the line strengths from the bow is accomplished by integrating the emission from all the different annuli (each with a specific normal shock velocity). Then each annulus is divided into segments that can be treated as individual planar shocks. The H_2 line ratios derived from bow shocks are independent of the bow velocity once the bow is moving faster than the breakdown speed (Smith et al. 1991b) since the only effect of changing velocity is to shift the H_2 line emitting section to the wings of the bow. The line ratios are sensitive to the shape of the bow, H_2O abundance and pre-shock density (Smith et al. 1991a). In comparison, no-H_2O J-shock models produce similar line ratios but with the shock pressure as the critical parameter.

The determination of C-shock line strengths requires normally an extensive multi-fluid code that follows the chemistry and the physical interactions between the charged particles and the neutrals throughout the shock. A useful approximation to the column densities of H_2 lines derived for planar C-shocks can be written as (Smith and Brand 1989; Smith et al. 1991b) :

$$\frac{N_j}{g_j} = 44 n_0 L_0 \left(\frac{T_{max}}{T_j} + 0.1 \right) \frac{\exp\left(-\frac{T_j}{T_{max}} \right)}{T_{max}\, M_A} \qquad (2.25)$$

where T_j represents the energy of the state j, T_{max} is the peak temperature, n_0 is the pre-shock H_2 number density and L_0 is the length scale factor given by $L_0 = 1/(n_0 \sigma_0 \chi)$, where $\sigma_0 \approx 10^{-15}$ cm^2 and χ is the ionised fraction (typically $\leq 10^{-5}$). The first term in brackets represents the downstream cooling flow while the second term is the contribution from the peak temperature region.

2.5.3 Instabilities

It is important to analyse the stability of shock fronts since under certain conditions some shock-induced disturbances can grow and completely alter the shock structure. Here, we briefly mention some of the perturbations to the medium that may make the shock unstable.

2.5.3.1 UV radiation

Strong shocks will produce copious UV radiation from the shock front. This radiation can travel upstream and alter the ionisation level of the pre-shock medium. At the head of a bow shock, the strength of the shock will normally dissociate and ionise the particles and thus generate photons with energies exceeding 13.6 eV. A column density of $N_H \approx 10^{18}$ cm^{-2} is normally required to shield the rest of the bow from this UV radiation (Smith and Brand 1990b). Hollenbach and McKee (1989) have demonstrated that for such shocks this radiation is completely extinguished for neutral shock speeds $v_n < 120$ km s^{-1}. Hence, to maintain a low ionisation fraction requires significant depletion of the ionisable metals onto dust grains and column densities in excess of 10^{22} cm^{-2}.

2.5.3.2 Ion-neutral streaming

A different type of instability arises from the deformation of the magnetic field in the shocked layer (Wardle and Draine 1987). This instability occurs when a slight distortion of the field leads the ions to the magnetic *valleys*. This tends to increase the ion density in some locations, and as the drag force ($\propto \rho_n \rho_i (v_n - v_i)$) (Fig. 29). increases, the bend in the field lines will tend to grow further. Wardle (1991) has found from the linear stability analysis of the fluid equations that the stability in C-shock waves depends on the Alfven Mach number of the flow. Wardle's study suggests that MHD shocks are unstable for $M_A \geq 5$. As a result only low velocity shocks (≈ 10 km s^{-1}) appear to be stable. However, this limit is valid only to the linear stability analysis. A non-linear development of the instability is still lacking. The effects on the overall C-shock structure could prove significant if the instability grows to large amplitudes.

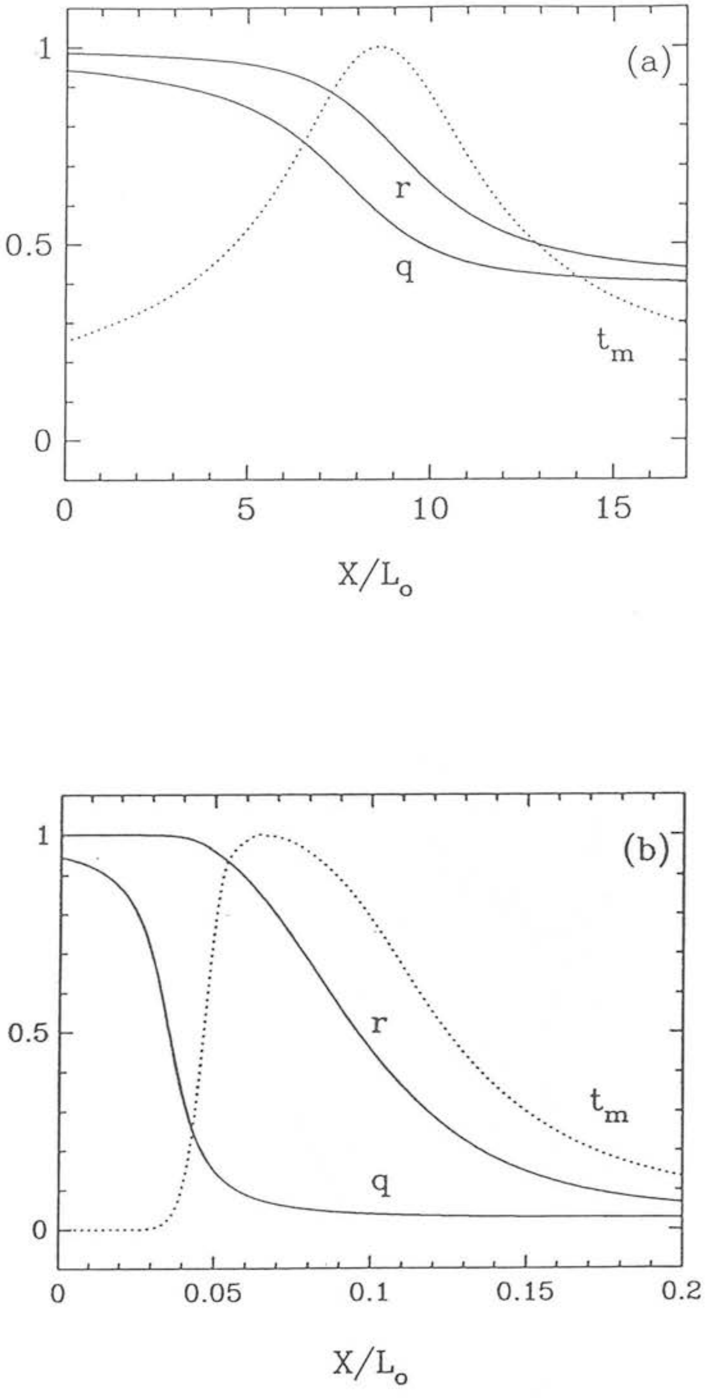

FIGURE 2.7: (a) The structure of a soft C-shock with $V_s = 198$ km s^{-1} and $v_A = 92.8$ km s^{-1} for an ionisation fraction of 3×10^{-7}. The neutral velocity is rv_S; the ion velocity is qv_S and the normalised neutral temperature $t_m = T/T_{max}$ are displayed. (b) The structure found for a cool C-shock with parameters $V_s = 39$ km s^{-1} and $v_A = 1.6$ km s^{-1}. Adapted from Smith (1991b).

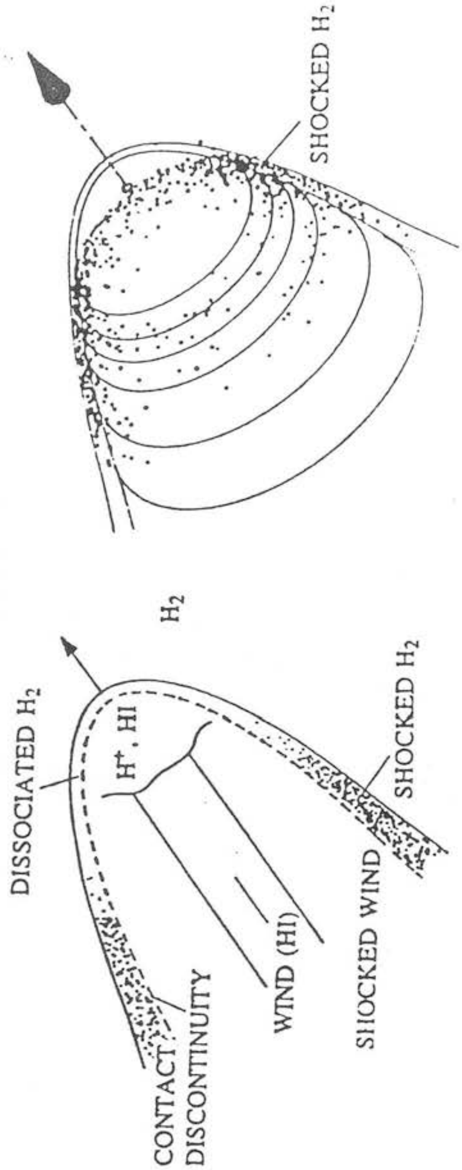

FIGURE 2.8: Structure of a bow shock. Different emission line regions are labelled by their main coolants. Adapted from Smith (1991c).

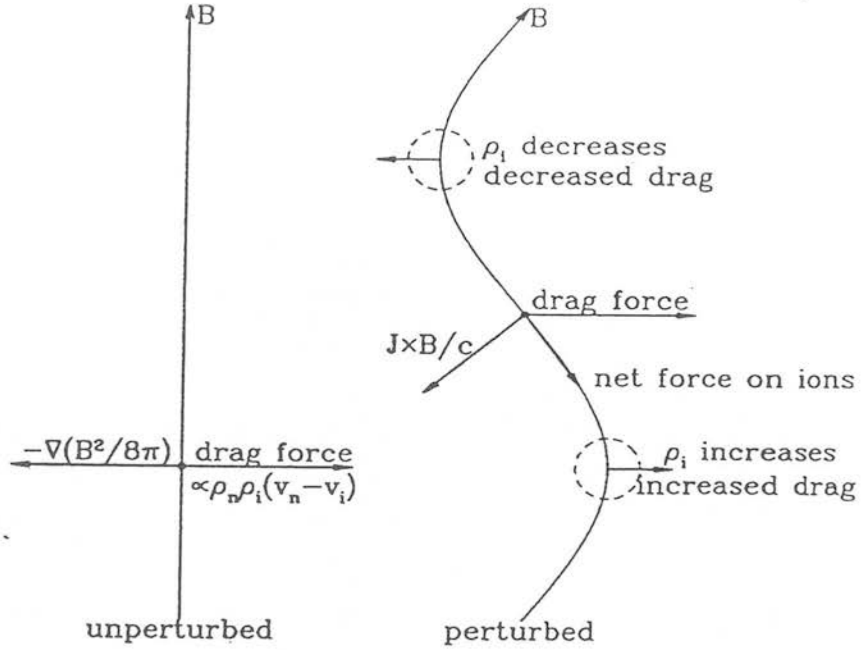

FIGURE 2.9: Wardle isntability in MHD C-shock waves. Adapted from Draine and McKee (1993).

Chapter 3

Near-infrared spectroscopy

The development of infrared astronomy has largely been dictated by technological advances in the detector materials and the miniaturisation of infrared detectors. Only a few wavebands are accessible for ground based observations due to the opacity of the earth's atmosphere. Because the radiation from the telescope and the optics plus the earth atmosphere are strong thermal emitters of infrared radiation, it is now a common practice to cool both the optics and detector with liquid nitrogen (77K) to reduce their infrared contribution. The observations contained in this dissertation were made with the United Kingdom Infrared Telescope (UKIRT) sited on top of Mauna Kea in Hawaii and the cooled grating spectrometer CGS4. This grating spectrometer has been recently commissioned with UKIRT and now provides a long slit capability, usually 1.5" × 90", and high spatial resolution near-infrared images (1.5 arcseconds pixel size). CGS4's increased sensitivity associated with the vast range of features explained in this chapter, makes it the most comprehensive spectroscopic facility for studies in the 1 μm – 5 μm region.

3.1 Introduction

Infrared astronomy spans the 1 μm to 1 mm wavelength region and is subdivided according to the differences in detector capabilities and observational difficulties. The near-infrared region covers the 1 μm to 5 μm waveband. This waveband is a rich spectroscopic region for infrared astronomy because many astronomical emission lines occur within that region. There are considerable advantages by observing in the infrared. Interstellar dust extinction is greatly reduced in the infrared compared to the optical, a factor of 10 for a normal extinction law ($R = 3.1$; see section 3.5.1), between 5500 Å and 2.2 μm. Thus, we are able to look into regions that are normally obscured to optical radiation. These regions are the birth places of new stars that are created in the dense cores of molecular clouds. By detecting the infrared radiation from these protostellar environments, we can explore the dynamic and violent interstellar medium at work using the many atomic and molecular lines that are radiated in the near-infrared wavelengths. An important step forward for infrared astronomy was accomplished in the mid 80s, when the Infrared Astronomical Satellite (IRAS) carried out the first complete survey of the far-infrared sky, revealing intense emission from massive regions of star-formation within our galaxy. Dust grains in the interstellar gas also play an important role in the infrared. Firstly, infrared radiation readily escapes from inside dense cloud cores that are obscured at optical wavelengths, therefore providing a fundamental tool to study these regions at high angular resolution. Secondly, dust re-processes the radiation from these regions by absorbing short wavelength radiation and emitting this energy at longer wavelengths.

Much of the early work in the infrared has been done with single element detectors. More recently, simple spectrometers using multiple detector elements that are scanned across the relevant waveband have been used. Such an example is CGSII; a cooled grating spectrometer built as a linear array of seven detector elements. Two dimensional infrared arrays have only recently been built and now provide improved spatial and spectral resolution and higher sensitivities, of which CGS4 is an example. This instrument is a two-dimensional cooled grating spectrometer that currently replaces CGSII at UKIRT (UK Infrared Telescope), sited on Mauna Kea, in Hawaii. The high signal-to-noise achieved for the observations presented in the following chapters of the objects Herbig-Haro 7 to 11 (about 70 times fainter than Orion peak 1) and of DR21 (about 10 times fainter than Orion), have been possible thanks to the greater sensitivity provided by the new spectrometer, which also mapped the HH 7-11 region with small pixel sizes of 1.5 and 3 arcseconds.

3.2 Signal-to-noise considerations

It is important to know the precision of measurements of the flux of infrared radiation. Due to its nature, astronomical signals are very weak when observed against the very strong noise background. Typical sources of noise are the thermal fluctuations on the detectors, fluctuations in the intensity of the sky background, Poisson noise, thermal instability of the telescope and optics, dark current in the detector and read out noise. Infrared technology has advanced enormously in recent years as to make most of the observations background limited, meaning that the dominant source of noise is the *sky + telescope* fluctuations in the background intensity. A source with a flux density N(ν) photons per square meter, per second, and per frequency band, which is observed for a time Δt in the waveband Δν and with an effective aperture telescope collecting area A, is detected with a signal of,

$$Signal = \mathrm{N}(\nu)\ \mathrm{A}\ \Delta\mathrm{t}\ \Delta\nu \quad \text{photons.} \tag{3.1}$$

If the intensity of the night sky is B(ν) photons per meter square, per second, per steradian and per frequency band, then we observe a signal from the sky of $\mathrm{B}(\nu).\mathrm{A}.\Delta\mathrm{t}.\Delta\nu.\Delta\Sigma$ through a solid angle ΔΣ subtended by the detector. So, for background limited observations of faint objects in the infrared waveband, the signal-to-noise is

$$\frac{Signal}{Noise} = \mathrm{N}(\nu)\sqrt{\frac{\mathrm{A}\ \Delta\mathrm{t}}{\mathrm{B}(\nu)\Delta\Sigma}}\,. \tag{3.2}$$

In practice, though, the seeing disk caused by thermal fluctuations in the atmosphere, compromises the spatial resolution by spreading the energy into adjacent pixels. This effect distorts the wave front and blurs the image, usually limiting the smallest $\Delta\Sigma$ achievable. In the infrared, the seeing disk is normally smaller than 1 arcsecond in a good photometric night. From equation (3.2), we see that to improve a particular astronomical observation we need to use longer integration times, or use a bigger collecting area telescope.

3.3 The CGS4 detector array

3.3.1 CGS4 capabilities and features

This section intends to give a brief summary of the CGS4 spectrometer and describe its main features. For a more detailed description the reader is referred to a report by Mountain et al. (1990). CGS4 (see Fig. 3.1) is a common user 1-5 μm grating spectrometer featuring a long slit capability and is now permanently located on the instrumental bench of the UK Infrared Telescope. The 2-dimensional InSb detector array that is installed in a cryostat and lodged inside CGS4's optical bench, is cooled with liquid nitrogen to a temperature of ≈ 77 K and maintained below 80 K by the first stage of a commercial closed cycle-cooler. The array is cooled separately by the second stage of the cooler motor to ≈ 35 K. At present, the array contains 58 × 62 pixels but is expected later this year to be replaced by a 256 × 256 InSb array. The array can be used in single or multiple non-destructive readout modes, with the latter resulting in lower read noises of 40-50 electrons for 20 second exposures. Two observing modes, stare and chop, are available; the latter is often employed for medium resolution at thermal wavelengths (beyond the K waveband). CGS4 provides a built-in calibration unit containing a black-body source for flat-fielding and several arc lamps (argon, krypton and xenon) used for wavelength calibration. The spectrometer uses a fast f/1.35 camera to illuminate a 3 mm × 10 mm focal plane, which corresponds to a 3″ × 90″ long slit. A second f/2.7 long camera is available to provide smaller pixel scales of 1.5 arcsecond/pixel. Resolving powers ($\lambda/\Delta\lambda$) in the range 300 – 20000 can be achieved by means of two internal gratings, mounted back to back. The available gratings are a 75 lines mm^{-1}, providing resolving powers of about 300 – 800, a 150 lines mm^{-1}, which provides resolving powers of about 1000 – 2000 and a 31 lines mm^{-1} echelle that provides a resolving power of about 8000 (38 km s^{-1}).

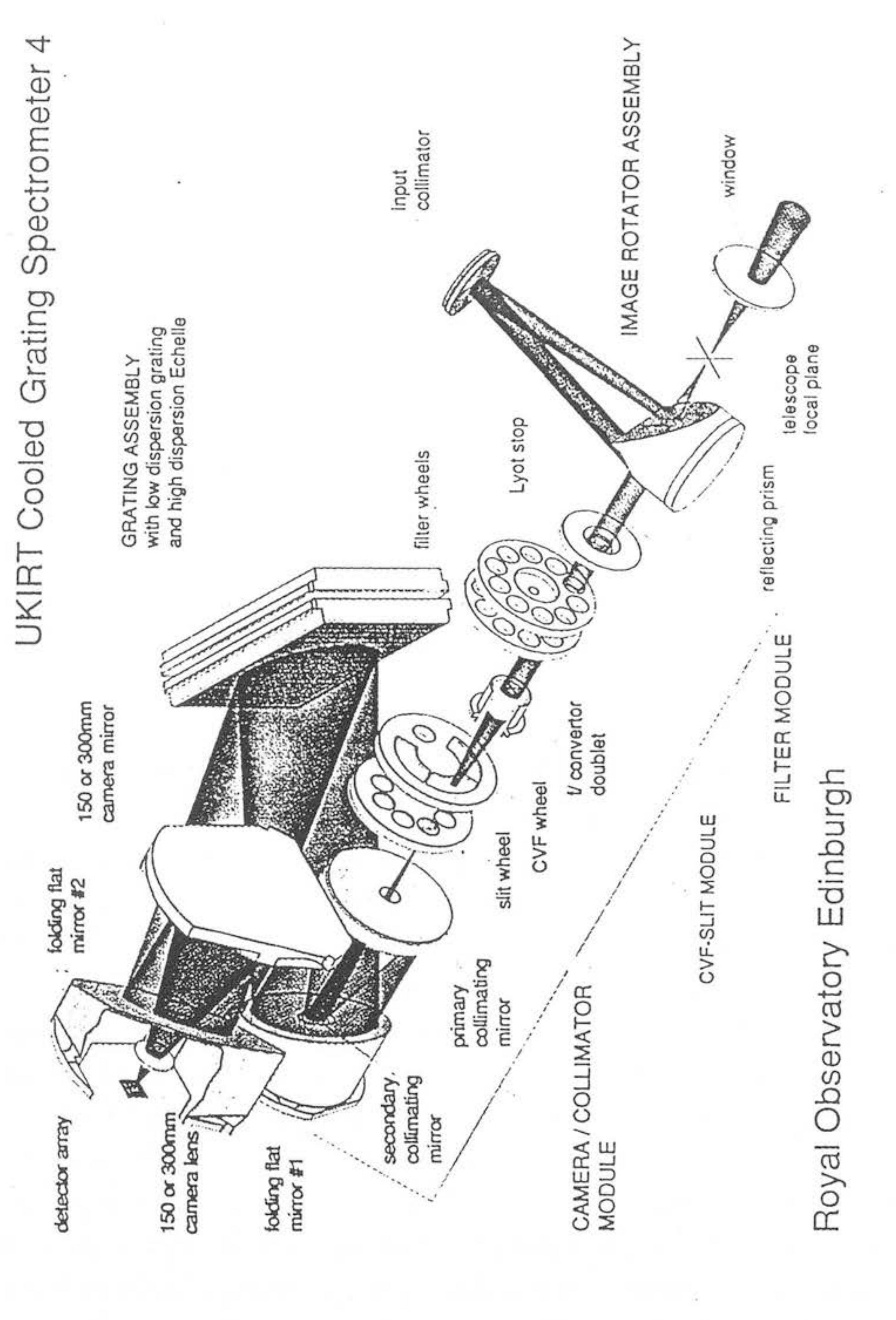

FIGURE 3.1: The CGS4 optical layout

These resolving powers are achieved using the standard 150 mm focal length camera optics (yielding a pixel size of 3″) whereas with the 300 mm focal length camera, the resolving powers are doubled and the pixel scales are halved.

A technique often used with the spectrometer is to over-sample the spectra by stepping the detector with a resolution of up to 1/10 of a pixel over 2.5 pixels. This procedure allows us to replace bad data obtained at wavelengths that correspond to bad pixels, with the data from adjacent good pixels. Thus, only pixels situated next to other bad pixels and at the edge of the array remain in the reduced data; the data from the good pixels are averaged. A significant advantage of CGS4 over-sampling technique is that its grating is in a fixed position, with the over-sampling being performed by sliding the detector. This results in a high degree of repeatability and ease in interleaving spectra.

3.3.2 Taking data frames

In order to obtain the final calibrated object frame, it is necessary to take other additional frames to subtract out the signal from the hot chip electronics and to ratio out the background sky signal. To do this, several data reduction steps are required to take the initial raw object frame and make a reduced object frame. These extra frames, which are normally called observational overheads, are commonly referred to as the bias frame, dark frames, flat-field frames and arc lamp frames and provide the necessary means to extract the data counts that arise exclusively from the object (see Table 3.1). The bias frame is exposed for milliseconds. This frame is subtracted from all observations and represents the intrinsic emission due to the array electronics. The bias frame is only required for observations taken in destructive readout mode. In non-destructive readout (NDR) mode, the periodic sampling of the accumulating signal during an integration renders lower readout noises since these samples are used to calculate the best fit to the slope of the integrating signal so reducing the uncertainty in the measurement. In addition, this strategy automatically compensates any correction to the DC level offset. Dark frames are taken with the shutter closed so that the array does not receive any light. The difference between this frame and the bias is the longer integration time used (few tens of seconds), so that we can measure the dark current present in the detector array. Currently, the array in CGS4 has a very low dark current level, about 2-3 electrons per second. Thus, the dark frames are not usually necessary but are often taken to monitor the array's performance.

TABLE 3.1: Typical CGS4 observation and data reduction sequence

Observation	**Reduction sequence**
BIAS	apply bad pixel mask
DARK	subtract bias
FLAT	subtract bias; normalise with (e.g. 3rd order) polynomial fit
ARC	subtract bias; flat field; interleave integrations
STANDARD STAR	each alternate object or sky: subtract bias; flat field; interleave; apply λ calibration; form object–sky pairs; co-add
SOURCE OBJECT	alternate object or sky: subtract bias; flat field; interleave; apply λ calibration; form object–sky pairs; subtract residual sky; co-add; divide by standard

Removing pixel-to-pixel variations within the array involves taking a frame of an object with a flat continuum (usually a blackbody lamp or the telescope dome) with the same exposure time and grating setting as the source object. This flatfield frame is a short exposure taken in destructive mode. Lastly, taking an arc lamp frame, will ensure accurate spectral calibration. The observation procedure is summarised in Table 3.1.

3.3.3 Data reduction technique

Because spectroscopy is an essential part of this work, the spectroscopic reduction procedure is briefly described here. With CGS4, the observations are stored separately for the object and the sky. These are later subtracted in pairs to form the raw object image. In addition, several measurements of a standard star with known magnitude are taken to calibrate the flux of the object. Normally, and to avoid excess overheads when observing, a star is chosen close to the object's airmass to provide both flux calibration and to remove the atmospheric absorption features. This procedure must be used with precaution however, since the very narrow absorption lines in the atmosphere can remove a significant fraction of the object's line flux in emission lines that are intrinsically narrow. In addition, several lamp lines are measured at the same grating positions to provide wavelength calibration. These arc frames are reduced by subtracting the bias and dividing by the appropriate flat-field — taken at the same wavelength and resolution. Two other important frames, the bias and the flatfield, must also be taken. The only operation carried out on the bias frame is the application of a bad pixel mask. The bad pixel mask is a map of all the dead and noisy pixels contained in the array; the locations of these are subsequently ignored in the reduction process. Flat-fields are reduced by subtraction of the bias. Further, they are normalised by a polynomial function to remove the spectral structure resulting from the black-body lamp. A normalised flatfield frame is then multiplied by the object's frame. Finally, there a signal known as the dark current signal that increases with exposure time. It is therefore necessary to remove this signal from every observation. The normal procedure is to take an exposure of the same length of time as the object's but with the shutter closed so that no radiation reaches the array. Then, any signal recorded by the detector is due to the *hot* electronics. Dark frames are reduced by subtraction of a bias frame. In practice, though, the procedure of subtracting object from sky effectively cancels out the dark current emission (Puxley et al. 1992).

3.4 Observational techniques

At infrared wavelengths the background seen by the detector is often bright and fluctuating. For $\lambda < 2.3$ μm, atmospheric OH^- emission lines contaminate the very faint signal and for $\lambda > 2.3$ μm, the thermal emission from the telescope and atmosphere dominate the noise. In the first regime ($\lambda < 2.3$ μm), short exposures, less than about 60s, are dominated by photon noise which follows a Poisson distribution, e.g. for N photons detected, the associated uncertainty is given by $\sqrt{N}$. For long exposures, there is significant large amplitude fluctuations in the OH emissivity (see Fig. 2 of Puxley et al. 1992). The amplitude of this fluctuation is on average of order 10%. At $\lambda > 2.3$ μm, the short exposures are again photon noise limited, but for long exposures, there are extreme fluctuations in the emissivity due to differences in temperature of the parcels of gas crossing the beam. By employing a non-destructive readout of the array detector, the readout noise is substantially reduced – the effective readout noise is reduced by $\sqrt{12/n}$ where n is the number of times the array is read non-destructively. This is accomplished by sampling the signal on each pixel without affecting the signal level (Chapman et al. 1990).

These limitations that have to be taken into account when observing at near-infrared wavelengths mean that relatively short exposures are required on both source and sky, separately. Observing blank regions of the sky to provide sky subtraction may be achieved by employing the technique of *chopping*, which is done by tilting the secondary mirror, or by *nodding* of the telescope primary. In addition, the intrinsic faintness of most astronomical objects together with the background variability, requires observing in sequences of short exposures and many observations are normally necessary to achieve a satisfactory signal-to-noise. Because of this, it is essential to see reduced data whilst observing to assess data quality.

3.5 Interstellar extinction

Dust grains play a crucial role in all astrophysical observations by reducing the intensity of radiation received from astronomical sources and thus determines the ultimate appearance of the observed data. The total to selective extinction ratio, $R = A_V / E_{B-V}$, is often used to characterise the visual to near-infrared part of the extinction curve and specifies the amount of extinction for particular star formation regions. It has been suggested that the origin of the variation of this ratio may arise from increasing grain size due to accretion or coagulation in dense regions or alternatively, to a change in the chemical composition of the grains (Duley and Whittet 1992). In the standard interpretation of wavelength dependence of interstellar extinction, the near-infrared extinction arises through a combination of scattering and absorption by relatively large interstellar silicate and graphite grains (Mathis et al. 1977).

3.5.1 The galactic near-infrared extinction law

The determination of the extinction law has been the subject of much work over the past few years because it was realised that it contained not only information about the scattering and absorption processes but also about the interstellar grain population. The interstellar extinction in the near-infrared, although about an order of magnitude less than the in the visible, is nevertheless often sufficiently high to require correction when investigating the spectral energy distribution of obscured sources in dense star forming regions. In addition, the extinction law in the near-infrared is sensitive to the large particle cut-off in the size distribution and thus provides a useful constraint on grain models (Mathis et al. 1977). In this wavelength regime (1-5 μm), the extinction curve changes in slope from the λ^{-1} law, produced by particles that are comparable in size with the wavelength of radiation (e.g. visible), to the small particle limit, where the radius of a grain is much less than λ and the spectral index of extinction is generally greater than unity.

Several techniques have been employed to determine the extinction curve law in the optical-infrared waveband. These include the study of the reddening of stars, hydrogen line ratios from HII regions and line ratios from vibrationaly excited H_2 in molecular shocks. There is some evidence for the variation of the interstellar extinction law from the visible to ultraviolet for different line of sight (Witt et al. 1984). Fig. 3.2 shows the average interstellar extinction law in the galaxy, and contains data from various independent studies (Draine 1988). A published study of the extinction law based on observations of reddened early-type stars within a 2-3 kpc of the sun in regions around the galactic plane that are mainly obscured by dust in diffuse clouds, leads to a mean value of $R = 3.05 \pm 0.05$ (Whittet 1988). The shape of the extinction curve in the near-infrared can be characterised by a law of the form,

$$A(\lambda) \propto \lambda^{-\alpha} \tag{3.3}$$

where α is the spectral index for near-infrared extinction. The best curve fit in the range 1.6 μm to 5 μm yields a slope of -1.70 ± 0.08 (Whittet 1988). A study of this curve in the range 1 to 13 μm has also been reported by Rieke & Lebofsky (1985), who have observed several reddened stars in the galactic center and find a ratio of total to selective extinction of 3.09 ± 0.03. A single power law fitted to the data set in Fig. 3.2 in the range 1 to 5 μm, has the analytic form :

$$\frac{A_\lambda}{E(J-K)} = 2.4\left(\frac{\lambda}{\mu m}\right)^{-1.75} . \qquad (3.4)$$

Although the spectral index (curve slope) appears to be well determined by the data, the scatter between the different data sets renders an uncertainty of around 10%. Given this uncertainty, a slope of –1.7 has been adopted in chapters 4 and 5 to calculate undereddened column densities from the observed H_2 line intensities. The following relationships were used :

$$\begin{array}{ll} \text{a)} & 1.1\tau_\lambda = A_\lambda \propto \lambda^{-1.7} \\ \text{b)} & I_\lambda = I_\lambda^0 \exp(-\tau_\lambda) \end{array} \qquad (3.5)$$

where I_λ is the observed intensity of radiation, I_λ^0 is the intrinsic (undereddened) intensity of the source, and τ_λ ($\approx 0.921\ A_\lambda$) is the optical depth at the wavelength λ.

3.5.2 Using H_2 line ratios to measure the extinction

Observations of the line emission from vibrationaly excited H_2 can in principle be used to study extinction since vibrationaly excited states with $J > 1$ each has three $\Delta v = -1$ ($\Delta J = -2$, 0 and +2) transitions arising at different wavelengths. The most often used lines of H_2 are the bright 1-0 S(1) at 2.1218 μm and the 1-0 Q(3) at 2.4237 μm, both of which arise from the same upper level state at 6956 K. Therefore, the intensity ratio from those two lines is dependent only on the wavelength (λ) or energy of the transitions, the Einstein coefficients (A) and the differential extinction between both wavelengths :

$$\frac{I_{S(1)}}{I_{Q(3)}} = \frac{\lambda_{Q(3)}}{\lambda_{S(1)}}\frac{A_{S(1)}}{A_{Q(3)}} \exp{-(\tau_{S(1)} - \tau_{Q(3)})} \qquad (3.6)$$

The most recent study of the extinction in the near-infrared, used a 5″ beam to observe the H_2 lines: 1-0 O(5) (at 3.235 μm), 1-0 Q(3) and 1-0 S(1) in Orion peak 1 (Brand et al. 1988). Their estimate of the extinction toward Orion, proved to be limited by their measurement errors but is consistent with the –1.7 power law. Since the 1-0 Q-branch transitions occur at the edge of the K window and are often observed blended together, the 1-0 Q(3) line intensity provides only a crude way to estimate the reddening and whenever possible, the resulting extinction should be compared with other independent estimates. Nevertheless, because these two lines arise in the bright K window and they are often observed together, they provide a very convenient way to estimate the extinction to the source in the absence of other extinction data.

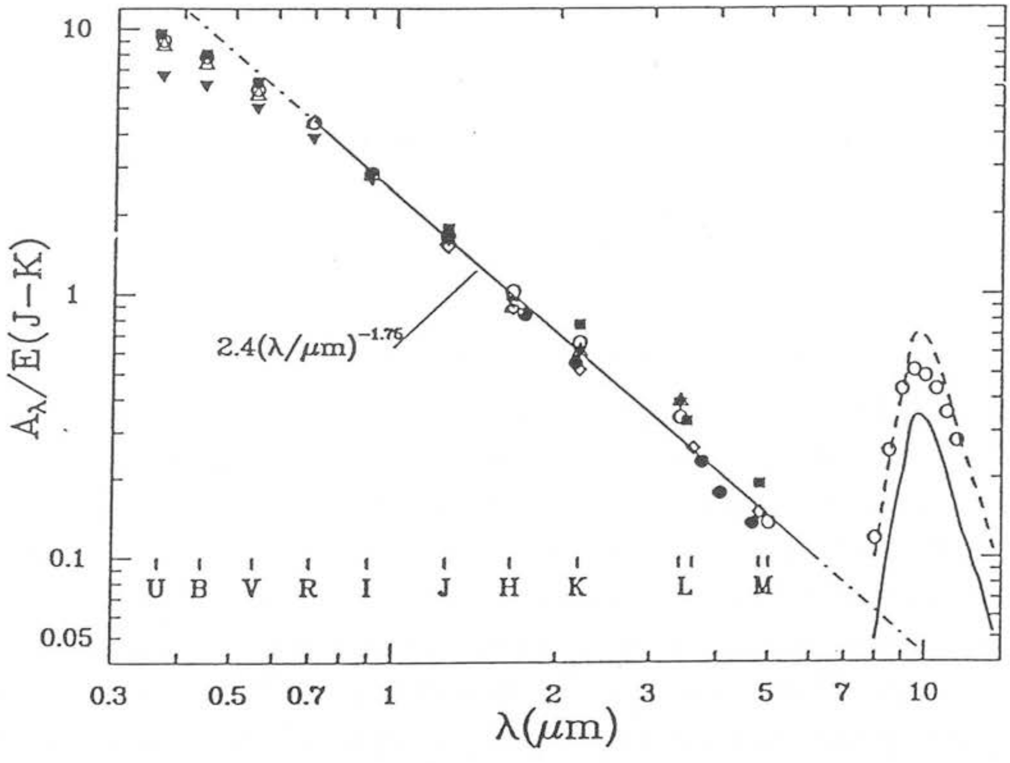

FIGURE 3.2: The interstellar extinction law in the Galaxy normalised to E(J–K). Different sets of data are plotted taken from independent studies (see main text). The straight line fit in this plot appears to be consistent with the observational data for 0.7 μm ≤ λ ≤ 5μm and yields a spectral index of –1.75. Adapted from Draine (1988).

Chapter 4

Shock diagnostics in Herbig-Haro 7: Evidence for H_2 fluorescence

---

Summary:

Near-infrared spectra from 2 μm to 2.5 μm in Herbig-Haro object 7 (HH 7) show emission lines of molecular hydrogen arising from a wide range of upper energy levels ranging from 6000 K to 25000 K. The high spatial resolution provided by CGS4 of 1.5 and 3 arcseconds per pixel has enabled measurement at six positions in HH 7. The bow geometry suggested for the shocked emission in HH 7 is investigated by comparing the H_2 column density ratios with predictions from J- and C-type shock models. It is shown that the small range allowed for the oblique angle over a section of the bow sampled by a 1.5″ pixel, fails to provide the large columns of warm gas measured in the high vibrational levels of H_2 compared to the low lying levels. It is suggested that the excess emission observed in the high-excitation lines may arise from H_2 fluorescence that is produced by Lyα resonance pumping in the hot post-shocked layers while the bulk of the H_2 emission would come from a Bow C-shock. We show that a shock-induced Far-UV radiation field with a strength of $G_0 = 10^2$–10^3 can account for the observed H_2 line ratios. An ortho to para ratio of 1.8 appears to be consistent with the H_2 fluorescent emission from HH 7.

4.1. Introduction

Herbig-Haro 7 is a bright emission object seen at the end of a chain of similarly shaped HH objects that are located in the B205 dark cloud (Herbig and Jones 1983). Directly aligned with this string of HH objects and located to the north-west, a young star, SSV13, is believed to be producing a supersonic wind that is shocking the surrounding molecular cloud and has produced the complex of Herbig-Haro objects known as HH 7-11 (Herbig and Jones 1983). These authors were the first to calculate proper motion vectors for these objects and found them consistent with gas motions directed away from SSV13. HH 7-11 are located in the blue lobe of a massive high-velocity CO outflow (Bachiller and Chernicharo 1990; Masson et al. 1990; Snell and Edwards 1981) which is possibly driven by a neutral atomic wind (Lizano et al. 1988; Rodríguez et al. 1990). The absence of emission in the redshifted lobe is certainly due to the higher dust extinction, as suggested by UV observations of H_2 (Cameron and Liseau 1990) and the high extinction value found for HH 7 (blue lobe) later in this chapter. The weak hydrogen recombination Hα emission line observed in HH 7 and HH 11 (Böhm et al. 1980; Solf and Böhm 1987) is indicative of a low degree of ionisation in the emitting gas, despite the observed large velocity dispersions (FWHM) seen in the optical lines of $\approx$ 50–100 km s^{-1} (Solf and Böhm 1987). These objects show [SII] λ4072 and [NI] λ5200 comparable to, or greater than Hβ and have [SII] λ6716/6731 and [OI] λ6300/6363 fluxes exceeding Hα. In addition, no [OIII] λ5007 emission is seen, the [NII] λ6583/6548 lines are weak and [CI] λ9850/9823 can be as much as 6 times stronger than Hβ (Hartigan et al. 1987). These observed characteristics are typical of low-excitation objects and impose severe constraints on any shock model that attempts to explain simultaneously the broad line profiles and the low-excitation spectra. Zinnecker et al. (1989) showed that the velocity structure observed in the H_2 lines appears similar to the higher excitation optical lines but with typically half the velocity dispersion. Their H_2 line ratios suggest shock velocities of 10–20 km s^{-1} and pre-shock densities greater than 10^5 cm^{-3}.

The 1-0 S(1) infrared emission map taken by Garden et al. (1990) shows considerable agreement with the Hα optical image (Solf and Böhm 1987), whose line profile suggests that HH 7 is a bow shock (Hartigan et al. 1987). The proper motions of Herbig and Jones (1983) together with the radial velocity information is consistent with the picture of a fast moving bow with the cylindrical axis of symmetry at approximately 45 degrees to the line of sight. The speed of the bow into its surroundings is possibly high enough (possibly $\geq$ 150 km s^{-1}) to completely dissociate H_2 at the bow front (*head*). However, the appearance of a tilted bow structure minus its *head* still gives the appearance of a complete bow (Bally and Lane 1991; Smith 1991a) due to the convexity of the far rim.

In this chapter we examine the vibrational–rotational emission of H_2 in several positions across the bow structure and compare it with predictions from bow shock models. The application of the bow C-shock model has so far been restricted to observation of complete bow structures, where the entire bow structure contributes to the spectrum. In this configuration, this model has been shown to successfully explain the OMC-1 data for the H_2 line ratios (Smith et al. 1991a) and the H_2 line profiles (Smith and Brand 1990b). The observations presented in this chapter dissect the bow structure in HH 7 and thus enable a stringent test of that hypothesis.

4.2. Observations

The observations of HH 7 have been obtained with the 3.8 meter United Kingdom Infrared Telescope (UKIRT), sited on Mauna Kea, Hawaii, and using the new cooled grating spectrometer with long slit capability CGS4 (Mountain et al. 1990). Two different data sets were taken of HH 7 in different observation nights. The first data set was obtained on the nights of 26–29 in November 1991. On these nights, the configuration chosen for CGS4 used the short focal length camera (F = 150 mm) and the 75 lines mm^{-1} grating, which yielded a resolving power ($R=\Delta\lambda/\lambda$) of about 340. At this resolution, a single grating position was required to make a complete coverage of the K window (2.1–2.45 μm). The 3 × 90 arcseconds long slit was oriented at 65 degrees west of north along the chain of Herbig-Haro objects HH 7 to HH 11 from the exciting source SSV13 that was used to accurately position the slit on HH 7 (Garden et al. 1990, R.A. = 3h 25m 58.1s, Decl. = 31° 5′ 45″). Two slit positions were measured, one along the axis of cylindrical symmetry of the bow (hereafter on-axis data) and the other offset 6″ south parallel to that axis (hereafter off-axis data). A total of 900 seconds of exposure time was obtained on-axis while for the fainter off-axis position the exposure time was 570 seconds.

A second data set was obtained for this source on the nights of 18–19 September 1992, with the large focal length camera (F = 300 mm) which provided a resolving power of ≈ 710 at 2.2 μm. In this configuration, the pixel size is 1.5″ and the array coverage is 0.2 μm requiring two grating positions to cover the K window. To calibrate the separate spectra, we measured the bright 1-0 S(0) emission line in both spectra. Because of the low spectral resolution of the data, the full width at half maximum (FWHM) of the H_2 emission lines was the instrumental FWHM (3.1×10^{-3} μm), which is equivalent to a velocity width of 420 km s^{-1}.

CGS4 provides an option to oversample the spectra by shifting the detector array by a fraction of a pixel. By sampling over two pixels, this technique ensures that bad pixels are replaced by good ones in the final spectra. The observations of HH 7 were taken by stepping the detector six times over two pixel positions. The log of the observations is presented in Table 4.1, including the observational parameters used with CGS4. The morphology of the HH 7-11 region in the infrared 1-0 Q(3) line of H_2 is shown in Fig. 4.1 (Stapelfeldt et al. 1991). Superposed on this map are the two observed slit positions cutting across the HH 7 bow.

4.3. Data reduction

4.3.1 First data set: 3 arcseconds pixel size

Sky frames were obtained by nodding the telescope to a non-emission region 30″ North-South from the object's position (middle slit position offset from SSV13 was 36″ E, 23.8″ S) for the on-axis slit position and 36″ N-S for the off-axis slit position, so that the same sky position was observed. The seeing conditions remained stable throughout the night, with an average seeing disk of 1 to 1.5 arcseconds. Periodic observations of the nearby star BS 788 (K magnitude = 3.60, R.A. = $2^h\,42^m\,14.9^s$, Decl. = +40° 11′ 38″, type F9V, $T_{eff} \approx 6000$ K) using the same experimental set-up of HH 7, were taken for two reasons: 1) to provide cancellation of telluric absorption lines and 2) to flux calibrate the final spectra. Wavelength calibration was achieved by measuring the emission lines of an argon lamp. By fitting these arc lines, we are able to calculate the deviation of the line centres from the actual centre wavelength listed in Outred (1978). A second order polynomial was fitted to the deviation curve and used to calibrate the wavelength scale of the reduced object's spectrum. This calibration is accurate to better than ≈ 0.1 pixels.

4.3.2 Second data set: 1.5 arcseconds pixel size

At the resolution employed to take this data set, two grating positions were required to completely cover the K window. The observations in the first grating position (2.03 μm to 2.24 μm) were made through unstable atmospheric conditions, including the presence of high cirrus clouds. As a result, the calibrated object minus sky spectra showed residual sky lines, which are due to the rapid variation of sky brightness from frame to frame. Residual sky subtraction was performed on this data set by using a region of blank sky that was observed within the object's frame. The standard star BS 718 (R.A. = $2^h\ 28^m\ 9.0^s$, Decl. = +8° 27′ 36″) lies close to the object's airmass and was observed routinely through the night to remove atmospheric absorption lines and the different pixel sensitivities of the detector array, using the star's colour temperature (spectral type B9III $\Rightarrow T_{eff} \approx 11000$ K). This star (K = 4.43) was also used as a flux standard to calibrate the object's flux. On the following night the weather conditions improved and remained stable throughout. The observations were taken in the second grating position (2.22 μm to 2.43 μm) with a total exposure time of 32 minutes on source, while this was 12 minutes for the first night's data (grating position 1). Observing in the second grating position (2.22 μm – 2.43 μm) resulted in a drop of flux, which was probably caused by the hot electronics (see Chapter 3). This effect was measured by comparing the 1-0 S(0) line flux observed in both grating positions. Because of this, we flux calibrated the spectrum taken in the second grating position (which had the brightest 1-0 S(0) line flux) and applied a correction factor to calibrate the line fluxes measured for the first grating position (2.03 μm – 2.24 μm). Several lines from a krypton lamp were measured at both wavelength ranges to provide wavelength calibration.

4.3.3 Reduction technique

The data reduction procedure has already been described in some detail in Chapter 3. The first step of the reduction process uses the off-line CGS4 data reduction software package for interleaving the detector scans and performing bias subtraction. The bias subtracted object frame is then divided by a flat field frame and subtracted by the closest sky frame. Several such frames are then added to increase the signal-to-noise ratio. The co-adding of the frames is done by calculating the average signal in each spectrum in the frame. Then, the error at each spectral point is calculated from the scatter of the spectral values from the average. This method of calculating the errors for each spectral point is more accurate in the eventuality of a cloud temporarily crossing the beam and reducing the flux in some frames.

The line fluxes for the H_2 lines were calculated by fitting the instrumental triangular profile. The triangular shape is due to the convolution of two top hat profiles that arise from the process of sliding the detector's square pixels over the rectangular slit. The minimum χ^2 method is used to calculate the individual line parameters: centre wavelength λ_c, height of the line h, full width half maximum (equivalent to half the base) FWHM and continuum level c. The FWHM is let as a free parameter only for the bright lines for which an accurate estimate can be derived. The faint lines are fitted by fixing FWHM at the instrumental FWHM profile. The best estimates for the line parameters are found by minimising the function χ^2 :

$$\chi^2 = \sum_i \left(\frac{f(i;\lambda_c,h,c,FWHM) - obs(i)}{\sigma_i} \right)^2 \qquad (4.1)$$

with respect to the four line parameters. In equation 4.1, obs(i) is the observed intensity value at spectral point i, σ_i is the error associated with point i and f is the triangular profile function defined by :

$$\begin{array}{ll} \frac{h_\lambda}{FWHM}(\lambda-\lambda_c) + h_\lambda + c_\lambda & \text{for } \lambda_c - FWHM < \lambda < \lambda_c \\ \frac{-h_\lambda}{FWHM}(\lambda-\lambda_c) + h_\lambda + c_\lambda & \text{for } \lambda_c < \lambda < \lambda_c + FWHM \\ 0 & \text{otherwise.} \end{array}$$

The routine used to minimise the χ^2 function uses Marquardt's method (Press et al. 1986). The intensity of a line is then given by the product of the FWHM and the height best-fit parameters. The error in the flux is calculated by adding in quadrature the errors in the FWHM and the height. However, this calculation overestimates the error on the flux, due to not taking into account the anti-correlation of the height and the FWHM line parameters. A way round this problem is to replace, for example, the height parameter by a line flux parameter, since we can write the line flux = height × FWHM. Then, the error on the new parameter line flux is calculated in the fitting process, which uses the correlation matrix to calculate the parameter's uncertainties.

The existence of many narrow CO_2 atmospheric absorption lines in the 2.07 µm wavelength region can affect the measurement of the 2-1 S(3) line flux at 2.0735 µm. To model this effect, we need to know the intrinsic line width of the line and convolve it with the atmospheric absorption profile. A program called HITRAN was used to compute the atmospheric transmission profile of Mauna Kea. The intrinsic line width of this line is unknown, but as a rough estimate it can be taken to be close to the 1-0 S(1) line width of $\approx$ 45 km s^{-1} (Carr 1993; Stapelfeldt et al. 1991). Convolving a gaussian of FWHM = 45 km s^{-1} with the atmospheric absorption profile we have calculated the extent of the line absorption to be $\approx$ 10%.

4.4. Analysis and Results

The final reduced spectra obtained for the first data set (3″ pixel size) are presented in Figs. 4.2a and 4.2b for the on-axis slit and the off-axis slit positions, respectively. The location of SSV13 is to the top of the image and the HH objects from top to bottom are: HH 10, HH 8 and HH 7. The spectrum extracted from row 34 (HH 7's intensity peak) is shown in Fig. 4.3. The H_2 lines are superposed on a very weak continuum and this shows that HH7-11 is a pure emission line source at K. The spectra shown in Figs. 4.4a and 4.4b are from the brightest H_2 emission position in HH 7 from the second data set (1.5″ pixel size). The various H_2 lines are labelled on these plots. The flux density is measured in a 2.25 arcsec^2 beam. The line parameters for all H_2 lines detected are recorded in Table 4.2.

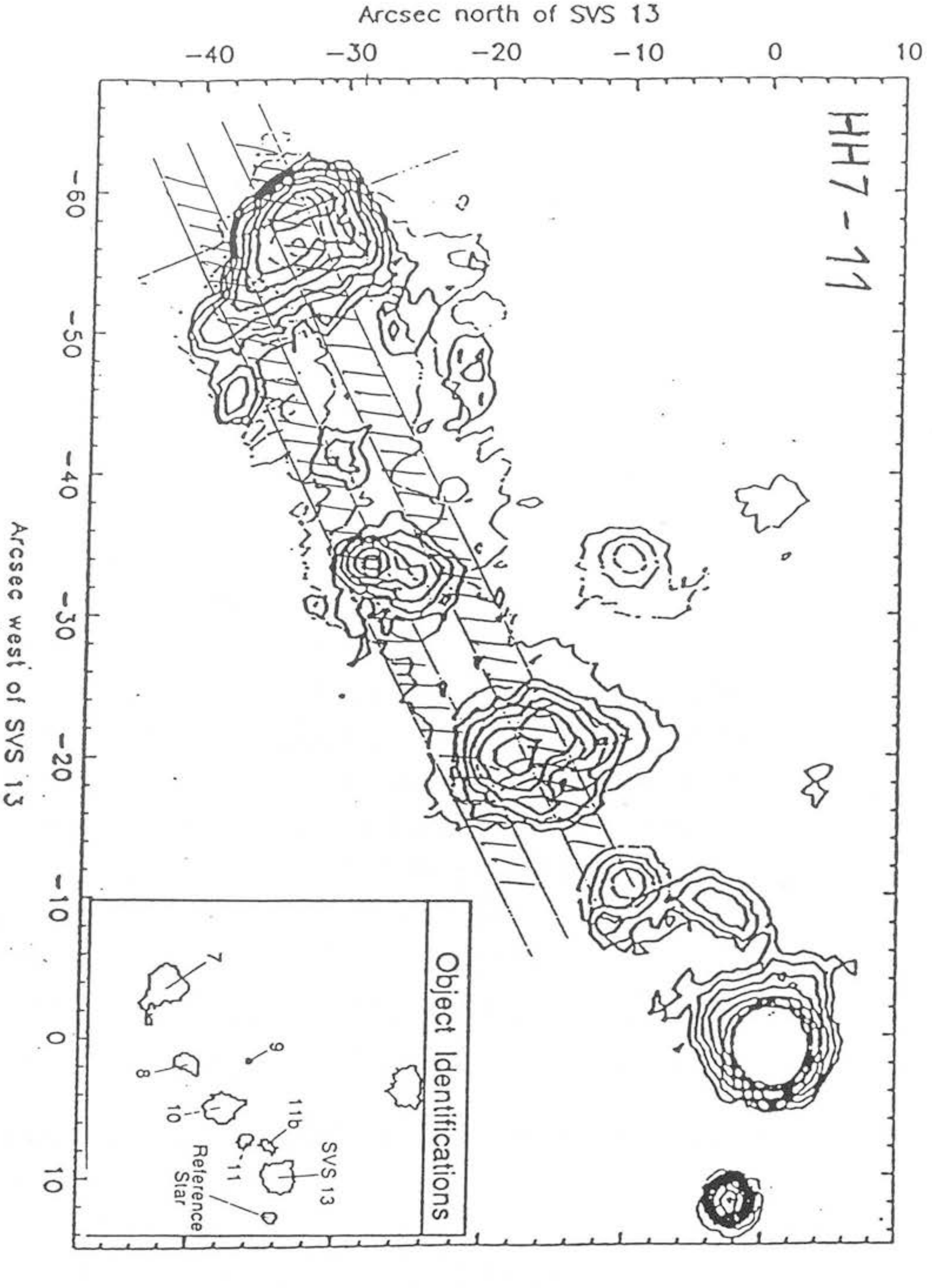

FIGURE 4.1: Overlay contour plot of the H_2 1-0 Q(3) emission from the HH 7-11 region taken by Stapelfeldt et al. (1991). The light contour represents 6717 Å [S II] emission. The measured slit positions are shown across HH 7.

TABLE 4.1: Observations log for HH 7

Observational parameters	**First data set** 26–29 November 1991	**Second data set** 18–19 September 1992
Grating	75 lines mm^{-1}	75 lines mm^{-1}
Observed grating positions	1: (2.03 μm – 2.43 μm)	1: (2.03 μm – 2.24 μm) 2: (2.22 μm – 2.43 μm)
Resolution ($\Delta\lambda/\lambda$)	340	710
Camera's focal length	150 mm	300 mm
Array coverage	0.4 μm	0.2 μm
FWHM (unresolved lines)	0.006 μm (420 km s^{-1})	0.003 μm (420 km s^{-1})
Slit on the sky	3″ × 90″ pixel size: 3″	1.5″ × 90″ pixel size: 1.5″
Orientation of slit	65 degrees N-W	65 degrees N-W
Measured slit positions: (offset from SSV13)†	2; separated by 6″ N-S 1) 36″ E, 23.8″ S 2) 6″ South of position 1	47″ E, 29″ S (overlap of position 1)
Exposure time (on source)	900 s - on-axis position 570 s - off-axis position	12 min (grating pos. 1) 32 min (grating pos. 2)
Standard star	BS 788 (K=3.60)	BS 718 (K=4.43)
Seeing	1″-1.5″	1″-1.5″

Note: †The SSV13 co-ordinates are: R.A. = $3^h\ 25^m\ 58.1^s$, Decl. = 31° 5′ 45″ (Garden et al. 1990).

TABLE 4.2: Line parameters for the observed H_2 lines

Transition label	Wavelength[a] (μm)	Energy (Kelvin)	g_J[b]	A[c] (10^{-7} s^{-1})
1-0 S(2)	2.0338	7584	9	3.98
2-1 S(3)	2.0735	13890	33	5.77
1-0 S(1)	2.1218	6956	21	3.47
2-1 S(2)	2.1542	13150	9	5.60
3-2 S(3)	2.2014	19086	33	5.63
1-0 S(0)	2.2235	6471	5	2.53
2-1 S(1)	2.2477	12550	21	4.98
3-2 S(2)	2.2870	18386	9	5.63
4-3 S(3)	2.3445	23956	33	4.58
2-1 S(0)	2.3556	12095	5	3.68
3-2 S(1)	2.3864	17818	21	5.14
1-0 Q(1)	2.4066	6149	9	4.29
1-0 Q(2)	2.4134	6471	5	3.03
1-0 Q(3)	2.4237	6956	21	2.78

Notes: a) Wavelength line centres are taken from Dabrowski (1984).

b) Assumes an ortho/para ratio of 3 for which $g_j = 3(2j+1)$.

c) Spontaneous decay probabilities are taken from Turner, Kirby-Docken & Dalgarno (1977).

a) NORTHERN SLIT

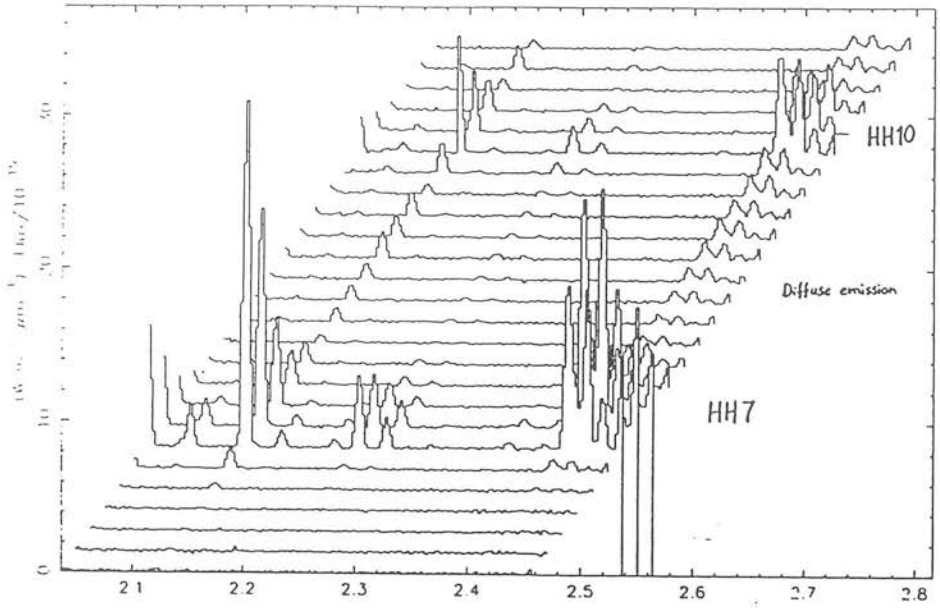

b) SOUTHERN SLIT

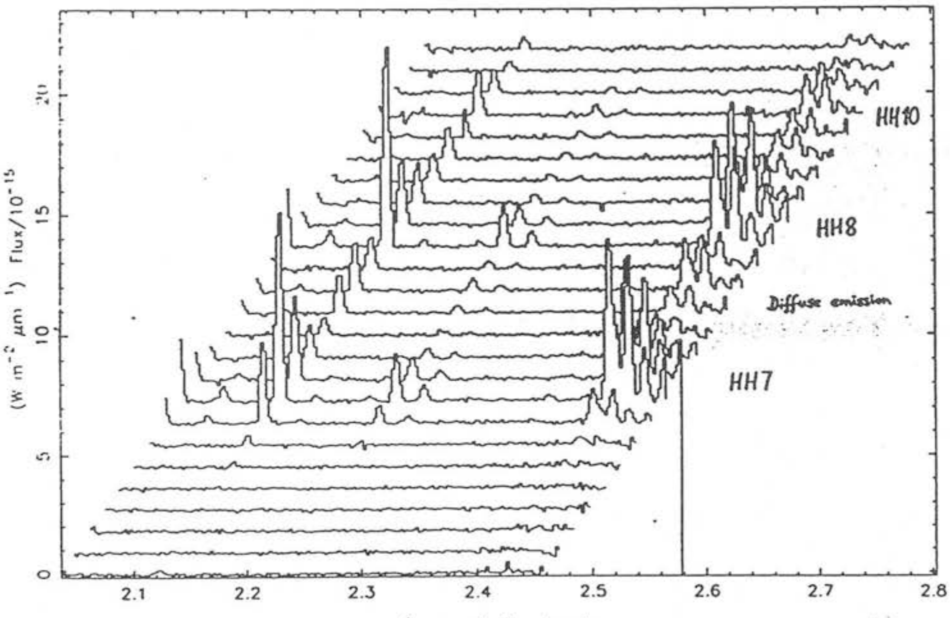

FIGURE 4.2: Intensity image of the whole array showing the spatial and spectral distribution of the H_2 emission in the HH 7-11 region for (a) the on-axis slit position and (b) the off-axis slit position.

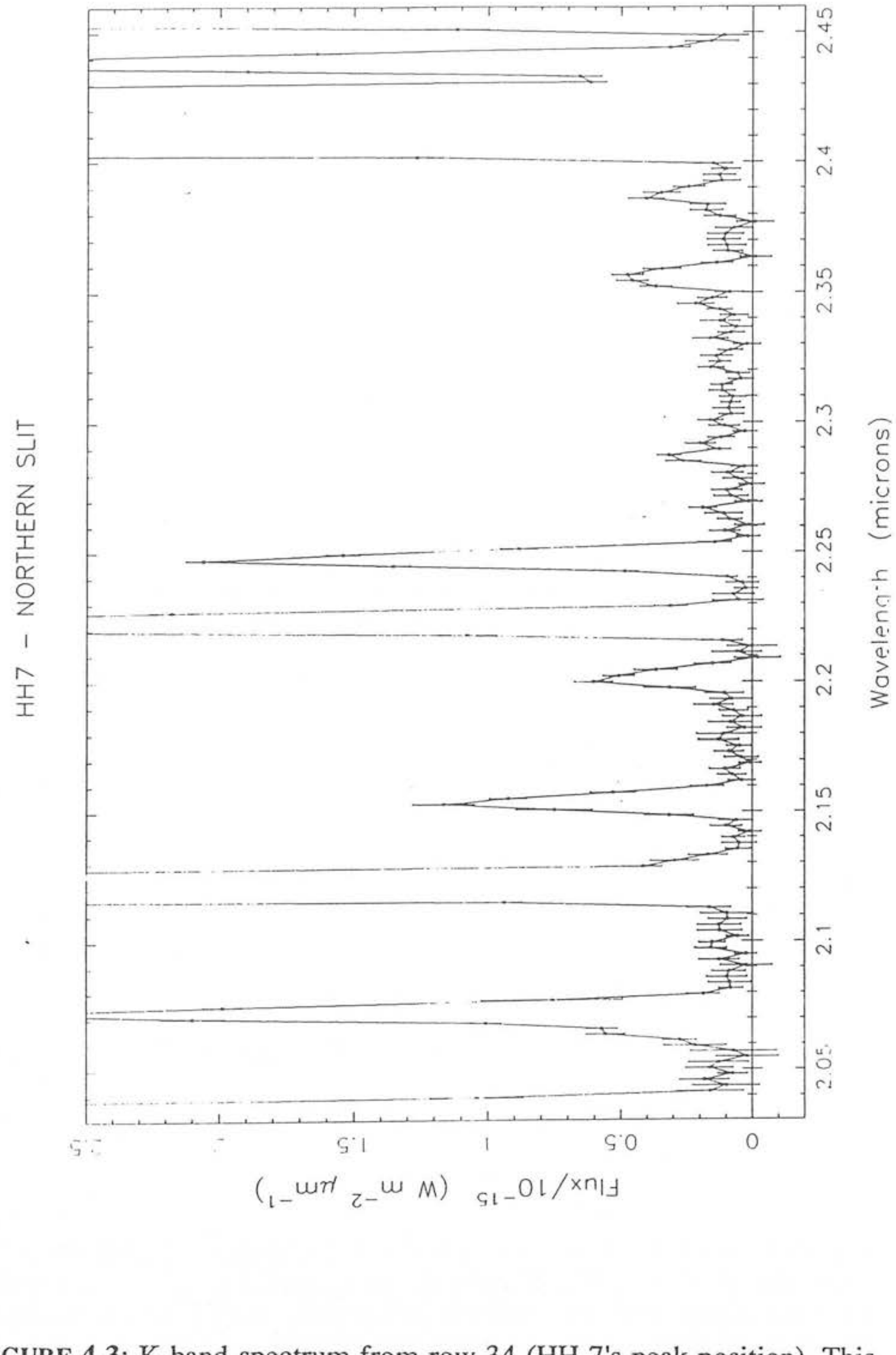

FIGURE 4.3: K band spectrum from row 34 (HH 7's peak position). This data is from the first data set (3 arcseconds resolution) and shows the relative intensities of the H_2 lines in the entire K window.

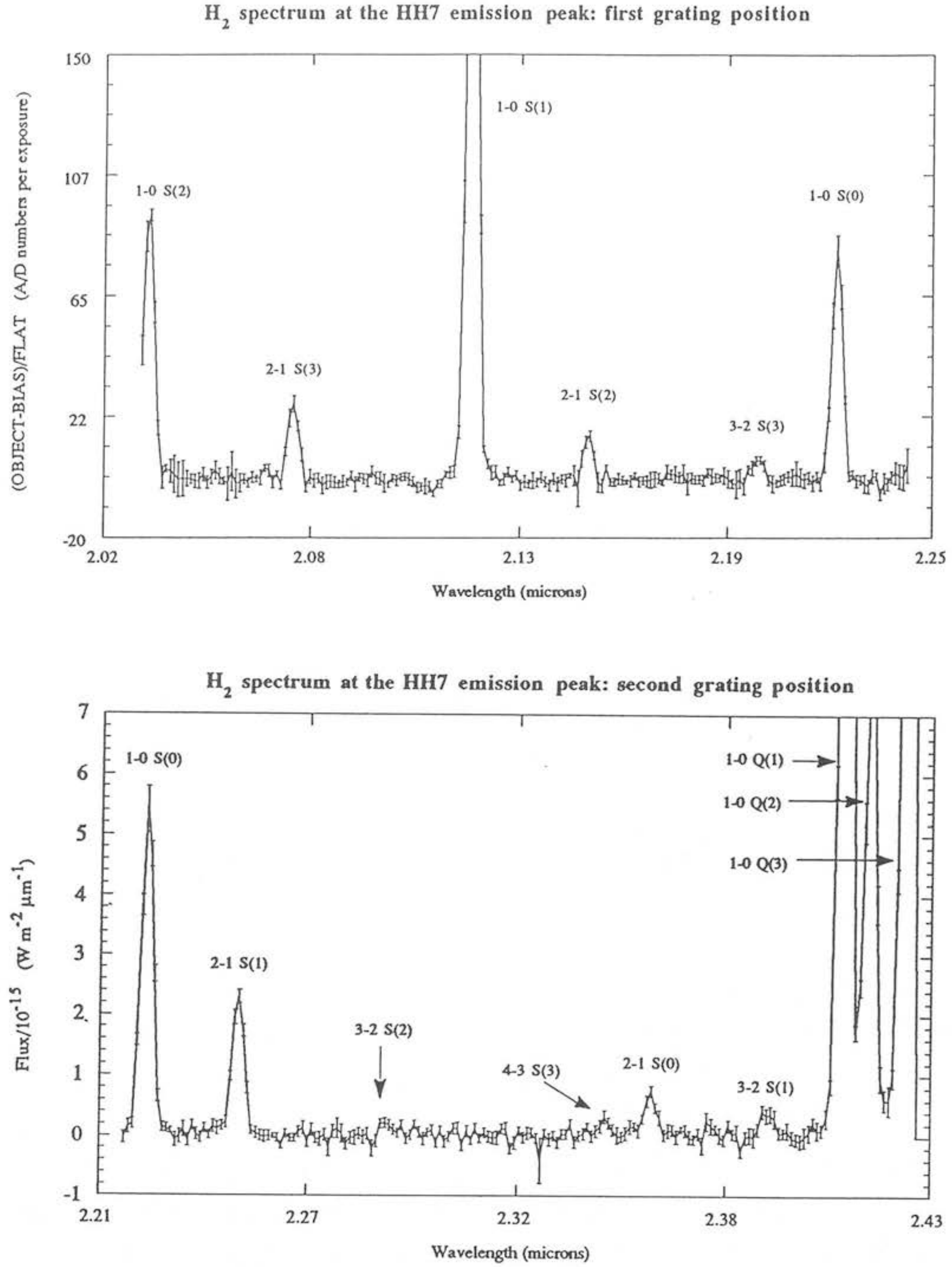

FIGURE 4.4: Characteristic H_2 spectrum taken at the HH 7 emission peak (detector row 34). (a) First grating position: 2–2.24 µm; (b) second grating position: 2.22–2.43 µm. The residual sky lines have been subtracted and all lines shown are of H_2. No flux calibration has been performed on the first grating position data (see main text).

4.4.1 Extinction measurements

The failure to detect the hydrogen recombination line Brackett-γ ($n=7 \rightarrow n=3$) at 2.166 μm, can be used to calculate a lower limit on the extinction. A 3σ upper limit for the Brγ flux is estimated to be $\approx 1.9 \times 10^{-18}$ Watts m^{-2} from the spectrum in Fig. 4.3. Using the Hα flux measured by Böhm et al. (1980) of 7.7×10^{-5} ergs cm^{-2} s^{-1} in a 3.5 arcseconds beam, the upper limit on the Brγ/Hα line ratio (not corrected for extinction) is 1.7. Assuming an extinction law of the form :

$$A_{\lambda} \propto \lambda^{-1.7} \tag{4.2}$$

over the wavelength range $0.7\ \mu m < \lambda < 7\ \mu m$ (Draine 1988; Whittet 1988) then,

$$A_{Br\gamma} = 0.13 A_{H\alpha} \tag{4.3}$$

and the Brγ/Hα line ratio can be written,

$$\frac{I(Br\gamma)}{I(H\alpha)} < \left.\frac{I(Br\gamma)}{I(H\alpha)}\right|_{observed} \times \exp\left(A_{Br\gamma} - A_{H\alpha}\right). \tag{4.4}$$

A lower limit can be found for the amount of extinction if we estimate the intrinsic Brγ/Hα line ratio. We will see that this puts some constraints on the possibility of observing UV fluorescent H_2 emission. The search for a fluorescent component in HH 7 has been carried out by Cameron and Liseau (1990) but no trace of H_2 fluorescence was found. Whether this is indicative of a high dust component in the line of sight blocking the H_2 UV line emission or that no fluorescent emission is produced in the cooling gas, is still unknown. Nevertheless, other Herbig-Haro objects with bright Hα emission have shown evidence for UV H_2 emission (see section 4.6.5.2).

Using the Brγ and Hα fluxes from the J-shock results in Hollenbach & McKee (1989) and equations 4.3 and 4.4, we derive that for a shock travelling into a medium with a density $\geq 10^5$ cm^{-3} with a speed $V_s \geq 60$ km s^{-1}, the extinction at the Brγ wavelength is $A_{Br\gamma} \lesssim 1.6$. This limit increases for shock speeds ≤ 60 km s^{-1}, e.g.

$V_s = 40$ km s^{-1} $\Rightarrow A_{Br\gamma} \lesssim 1.8$ and $V_s = 30$ km s^{-1} $\Rightarrow A_{Br\gamma} \lesssim 2.3$. In this calculation both recombination and collisional excitation processes are accounted for with recombinations dominating the spectrum for shock speeds greater than 60 km s^{-1} (Hollenbach and McKee 1989). Thus, the extinction at 2.2 μm is :

$$A_K \approx A_{Br\gamma} \lesssim 2.3. \tag{4.5}$$

The extinction can also in principle be estimated from the ratio of the 1-0 S(1) and 1-0 Q(3) H_2 lines. These two lines arise from the same (v = 1, J = 3) upper energy level of the molecule and therefore their intensity line ratio does not depend on the local level distribution, but on the transition branching ratio to other lower levels. The differential extinction between these wavelengths is given by :

$$A_{S(1)} - A_{Q(3)} = -2.5 \log \left(\frac{I_{S(1)} \lambda_{S(1)} P_{Q(3)}}{I_{Q(3)} \lambda_{Q(3)} P_{S(1)}} \right) \tag{4.6}$$

where P is the transition probability, I is the line intensity and λ is the wavelength of the transition. The extinction at K (2.2 μm) can then be derived using the extinction law in equation 4.2, giving :

$$A_K = \left(A_{S(1)} - A_{Q(3)}\right) \times \left[1 - \left(\frac{\lambda_{Q(3)}}{\lambda_{S(1)}} \right)^{-1.7} \right] \left(\frac{\lambda_{S(1)}}{\lambda_{Q(3)}} \right)^{-1.7} . \tag{4.7}$$

The combined effect of line blending and poor atmospheric transmission in the Q-branch region (situated at the right edge of the K window), compromises the accuracy with which the 1-0 Q(3) line flux can be measured and only a crude estimate of the amount of reddening is possible employing this method.

The extinction results derived from the 1-0 S(1) to 1-0 Q(3) line ratio are shown in Table 4.3 for the second data set; the extinction for the first data set will be dealt separately in the next section. It can be seen that the extinction estimates suffer from large uncertainties at each position (of order 50%) which is likely due to the low signal-to-noise of individual rows. A conservative value found from the average weighted with the errors is calculated to be 2.1 ± 0.6 magnitudes at 2.2 μm. This large value for the extinction in HH 7 is consistent with the previously calculated lower limit ($A_K \leq 2.3$, equation 4.5) and also with the apparent lack of UV H_2 emission from this source (Cameron and Liseau 1990).

TABLE 4.3: Extinction results from the 1-0 S(1) / 1-0 Q(3) ratio (1.5″/pixel HH 7 data)

Detector row	A_K (mag)
32	1.6 ± 1.0
33	2.4 ± 1.0
34	2.0 ± 1.1
35	3.5 ± 2.1
Average	2.1 ± 0.6

For the reasons already discussed in section 1.4, the H_2 column densities are calculated directly from the measured line intensities assuming optically thin emission. This can be written as :

$$N_j = \frac{4\pi}{hc} \frac{\lambda_j I_j}{P_j} 10^{0.4 A_{\lambda_j}} \tag{4.8}$$

where h is Planck's constant; c is the speed of light; P_j is the transition probability and I_j is the measured intensity of line j. The measured line intensities and the calculated column densities presented in Table 4.4 are for the four positions measured on-axis in Herbig-Haro 7 (1.5″/pixel data).

TABLE 4.4: H_2 column densities and line intensities for the four positions on-axis in HH 7 (1.5″ data set).

Transition	Column densities of the H_2 lines divided by the level degeneracy g_j N_j/g_j (10^{+14} cm^{-2})				Line intensities measured in a 1.5″ × 1.5″ beam I_j (10^{-18} Watts m^{-2})			
	Row 32	Row 33	Row 34	Row 35	Row 32	Row 33	Row 34	Row 35
1-0 S(2)	86.42 ± 10.04	105.37 ± 16.73	142.17 ± 11.15	64.12 ± 13.38	15.50 ± 1.80	18.90 ± 3.00	25.50 ± 2.00	11.50 ± 2.40
2-1 S(3)	5.56 ± 1.02	6.97 ± 0.91	7.03 ± 0.67	14.58 ± 1.35	5.57 ± 1.02	6.98 ± 0.91	7.04 ± 0.67	1.46 ± 1.35
1-0 S(1)	123.26 ± 9.63	132.15 ± 8.40	184.52 ± 14.82	74.84 ± 8.40	49.90 ± 3.90	53.50 ± 3.40	74.70 ± 6.00	30.30 ± 3.40
2-1 S(2)	6.42 ± 3.17	8.62 ± 2.76	13.90 ± 1.72	4.45 ± 3.48	1.86 ± 0.92	2.50 ± 0.80	4.03 ± 0.50	1.29 ± 1.01
3-2 S(3)	2.16 ± 0.52	1.95 ± 0.43	1.99 ± 0.36	1.93 ± 0.99	2.42 ± 0.58	2.19 ± 0.48	2.23 ± 0.40	2.16 ± 1.11
1-0 S(0)	170.72 ± 12.84	200.24 ± 14.12	265.70 ± 24.39	146.33 ± 19.25	13.30 ± 1.00	15.60 ± 1.10	20.70 ± 1.90	11.40 ± 1.50
2-1 S(1)	9.70 ± 0.59	11.72 ± 0.64	13.18 ± 0.70	6.47 ± 0.39	6.39 ± 0.39	7.72 ± 0.42	8.68 ± 0.46	4.26 ± 0.26
3-2 S(2)	1.76 ± 0.73	2.42 ± 0.73	2.12 ± 0.79	1.61 ± 1.03	0.58 ± 0.24	0.82 ± 0.24	0.70 ± 0.26	0.53 ± 0.34
4-3 S(3)	0.69 ± 0.32	0.54 ± 0.34	0.88 ± 0.30	0.43 ± 0.36	0.71 ± 0.33	0.56 ± 0.35	0.91 ± 0.31	0.44 ± 0.37
2-1 S(0)	9.08 ± 2.45	14.84 ± 3.00	17.45 ± 2.45	6.95 ± 3.87	1.15 ± 0.31	1.88 ± 0.38	2.21 ± 0.31	0.88 ± 0.49
3-2 S(1)	1.41 ± 0.49	1.78 ± 0.42	2.25 ± 0.47	1.30 ± 0.62	1.07 ± 0.37	1.35 ± 0.32	1.71 ± 0.36	0.99 ± 0.47
1-0 Q(1)	182.33 ± 6.89	213.86 ± 7.61	273.31 ± 7.97	160.22 ± 7.25	50.30 ± 1.90	59.00 ± 2.10	75.40 ± 2.20	44.20 ± 2.00
1-0 Q(2)	168.25 ± 14.71	226.18 ± 16.55	280.42 ± 17.47	169.17 ± 18.39	18.30 ± 1.60	24.60 ± 1.80	30.50 ± 1.90	18.40 ± 2.00
1-0 Q(3)	113.24 ± 4.98	142.15 ± 5.69	184.08 ± 6.40	100.92 ± 6.40	47.80 ± 2.10	60.00 ± 2.40	77.70 ± 2.70	42.60 ± 2.70

Notes:

The quoted uncertainties on the line intensities are the 1σ errors derived from the line fitting process. The errors on the column densities are derived by differentiating equation 4.8 and are given by $\Delta N/N = \Delta I/I$. The extinction law is assumed to be known exactly and to follow a law of the form $A_\lambda \propto \lambda^{-\alpha}$, with exponent $\alpha = -1.7$ (see main text).

4.4.2 Correction of the slit tilt in the 3″ data set

A tilt of roughly 0.4 degrees was known to exist between the detector array and the slit at the time of taking the first data set of HH 7 (Puxley, private communication). The tilted CGS4 optics have in this configuration the effect to spill-over flux from one row of the detector to another and hence make strong intensity gradients peak on different rows. This obviously affects the extinction estimates derived from the data, which uses the ratio of the 1-0 S(1) (2.1218 μm) and 1-0 Q(3) (2.4237 μm) H_2 lines that are widely separated on the spectra. If there is enough spill-over, e.g. at HH 7's emission peak, then the derived extinction value might even be negative, as demonstrated in Table 4.5 :

TABLE 4.5: Uncorrected extinction measurements for the 3″/pixel data in HH 7

Detector Row	A_K	error in A_K	Comments
35	–1.5	0.4	(poor S/N)
34	–2.2	0.1	1-0 S(1) peak
33	2.3	0.2	1-0 Q(3) peak
32	3.1	0.3	
31	3.2	0.5	(poor S/N)

Examination of Table 4.5 shows that the calculated extinction is negative at two positions, rows 34 and 35. For the on-axis slit position and at the intensity peak of HH 7 (row 34), the computed extinction is negative: –2.0 ± 0.1. Immediately behind that peak (3 arcseconds towards HH 10) the value for the extinction is positive: 2.3 ± 0.2. This behaviour was also observed in the off-axis slit position. Similarly, at the HH 7 intensity edge, the calculated extinction was negative: –2.8 ± 0.2, with a positive value of 0.3 ± 0.1 found for the inner position of HH 7. This trend was again observed at the intensity edge of HH 8, despite the low signal-to-noise. As a result, the existence of this misalignment between the slit and the detector, precludes an accurate determination of the extinction at each individual spatial position (3″ pixels). Hence, the line intensities and column densities cannot be correctly determined without applying a restoring algorithm to de-tilt the data.

We first present the results for the full spatial coadded emission for each object (equivalent of observing with a larger aperture) since this is independent of any small tilt. As the emission from HH 7 has the largest spatial extent (5 pixels) and a smoothly varying spatial intensity profile, it is the only object for which we attempt to model the effect of the tilt. The other HH objects would have their problem undetermined since for them, the model parameters (see Table 4.7) exceeds the no. of data bins (i.e., emission extent ≤ 3 pixels). In section 4.4.4, we employ a procedure to correct the tilted data in HH 7.

4.4.3 Large aperture beam extinction measurement

We can estimate the extinction over a larger area by adding the intensity from several rows encompassing the object. This has the disadvantage of averaging the spatial extinction gradient over the source but has the advantage of cancelling out the effect of flux spill-over between spectral rows and make the final result tilt independent.

For this exercise, the on-axis slit position was divided into three distinct regions: HH 7, HH 10 and the faint region between HH 7 and HH 10. The off-axis slit position was divided into four regions: HH 7, HH 8, HH 10 and the faint region between HH 7 and HH 8 (see Fig. 4.2). Then, the integrated emission of the 1-0 S(1) and Q(3) lines was calculated for each region by integrating the intensity over several rows that span the object. The results are presented in Table 4.6.

TABLE 4.6: Extinction results for the integrated object emission

On-axis slit position

Object	A_K	integrated rows
HH 7	0.9 ± 0.1	29 to 37
faint	0.2 ± 0.3	23 to 28
HH 10	3.0 ± 0.2	17 to 22

Off-axis slit position

Object	A_K	integrated rows
HH 7	1.0 ± 0.1	30 to 34
faint	(poor S/N)	27 to 29
HH 8	0.8 ± 0.2	22 to 26
HH 10	1.6 ± 0.5	16 to 21

The derived extinction values are always positive establishing the fact that the effect of the tilt has effectively been cancelled out. Both slit positions suggest ≈ 1 magnitude extinction at K for HH 7 whereas the faint region just behind HH 7 appears to have zero extinction, suggesting that the gap between HH 7 and HH 8 is real and *not* the result of foreground extinction. This result is consistent with the apparent similarity of spatial distributions seen in the Hα optical map (Solf and Böhm 1987) and in the infrared 1-0 S(1) map (Garden et al. 1990). The higher extinction towards HH 10 of 2–3 magnitudes plus its proximity to the source SSV13, suggests that this object is observed deeper into the cloud than the remainder HH objects and that the shocked material (traced by the H_2 emission) is ploughing through the dense molecular cloud and becoming visible as Herbig-Haro objects as they reach the cloud surface.

4.4.4 Emission model for HH 7

To correct the fluxes in each observed (pixel) bin requires the knowledge of (a) the amount of spill-over flux from adjacent rows as a function of wavelength and (b) the intrinsic emission (spatial) profile from the source. Since (a) and (b) are convolved in the spectra, we cannot separate their combined effects. However, if we can assume (b), it is possible to build an emission model for HH 7 that specifies the intensity at any given point in the spatial direction. As the emission from HH 7 is spatially unresolved, we model it as a continuous function of projected distance. The model must be able to reconstruct the observed (spatial) profile by emulating the detector's binning process of the incoming radiation. So, to model HH 7 we use the bright 1-0 S(1) and 1-0 Q(3) lines of H_2 (both with intrinsically similar spatial profiles) to fix (b) and have (a), i.e. the tilt angle, as the only free parameter. To do that, we need to calculate the fractional (spatial) shift between these two lines that has been produced by the tilt. As we shall see later, the tilt model will fully account for the negative extinction calculated from the raw data at the edge of HH 7. This also implies that any other possible mechanism that may contribute to this extinction trend, such as atmospheric absorption, should be negligible. The emission model used for HH 7 is described next.

First we assume that the extinction does not vary greatly on 3″ scales at the observed positions within HH 7 (i.e. there is no strong extinction gradients). Then, it is valid to use the average extinction value (Table 4.6) to deredden each spectral row. This is a reasonable assumption to make because, within the measured uncertainties, the extinction is the same towards HH 7 for both slit positions, which are separated by 6″.

Secondly, we use the observed 1-0 S(1) and Q(3) spatial emission profiles to calculate the relative spatial shift between their wavelengths. This is possible for these two lines because their profiles differ only by a factor that depends on extinction and the fractional shift. Now by assuming the extinction to be 1 magnitude (Table 4.6), the amount of shift can be computed.

Thirdly, we chose a function for the 1-0 S(1) spatial profile that when binned into detector pixels will match the observed profile. This is achieved by minimising the χ^2 function, defined as :

$$\chi^2 = \sum_{k}^{\text{all bins}} \left(\frac{S(1)_k^{\text{obs}} - S(1)_k^{\text{model}}}{\sigma_k} \right)^2 \qquad (4.9)$$

where $S(1)_k^{\text{obs}}$ is the observed intensity value in pixel k for the 1-0 S(1) line and σ_k is the 1σ uncertainty on the intensity. The required fractional shift is then given by shifting this profile to match the observed Q(3) profile. The results are presented for both slit positions in Figs. 4.5 (on-axis position) and 4.6 (off-axis position). Fig. 4.6(c) shows a cut through the observed 1-0 S(1) emission profile of HH 7. Several functions were fitted to this profile and the results are summarised in Table 4.7. This table shows that the *straight line* and *exponential* models fail to reproduce the observed 1-0 S(1) profile as their reduced χ^2 is large. By inspection of Fig. 4.6(c) we immediately see that the *straight line* model gives too much flux to the tail regions compared to the peak, whereas the *exponential* model gives too much emission in regions near the peak. The addition of a continuum plateau to the gaussian model, improves the fit substantially on the low signal-to-noise tail positions, which are the main contributors to χ^2. Thus, to calculate the fractional shift, we choose the *gaussian + continuum* model since this fits well at all observed positions. This model is displayed in Fig. 4.6(a). The result of binning this model function for first guess parameters is shown in Fig. 4.6(b) and the final binned result is shown in Fig. 4.6(d) for the best (minimum χ^2) fitted parameters.

TABLE 4.7: Parameters of the fitted functions to HH 7's spatial profile

Model designation	Equation profile		P†	χ_r^2	
				On-axis	Off-axis
Straight line	$A\frac{x}{x_0}$	$x < x_0$	2	463	–
	0	$x > x_0$			
Exponential	$A\exp\left(\frac{x-x_0}{\sigma}\right)$	$x < x_0$	3	97	–
	0	$x > x_0$			
Gaussian	$A\exp\left(-\frac{(x-x_0)^2}{2\sigma^2}\right)$	$x < x_0$	3	63	–
	0	$x > x_0$			
Gaussian + cont.	$A\exp\left(-\frac{(x-x_0)^2}{2\sigma^2}\right)$+cont.	$x < x_0$	4	4	5
	cont.	$x > x_0$			

Note: †P is the number of free parameters. χ_r^2 represents the reduced chi-square and is the value of χ^2 given in equation 4.9 divided by P.

Using the *gaussian + constant* model profile, we found the fractional shift between the 1-0 S(1) and 1-0 Q(3) lines to be *half* the pixel width. Table 4.8 shows the comparison between the model and the observations at each spatial position in HH 7. The results in this table show that the model fits best the higher signal-to-noise pixels (bins 3 and 4) at both slit positions. The model predicts consistent results for every bin belonging to the on-axis slit but breaks down at some positions on the off-axis slit. Therefore, the subsequent analysis of line ratios and its implications for the different types of shock, will be based on four positions from the on-axis slit: bins 1,2,3,4 and two positions from the off-axis slit: bins 3 and 4.

TABLE 4.8: Observed and model extinction values in HH 7

Spatial position	On-axis slit		Off-axis slit	
pixel/bin	Observed	Model	Observed	Model
1	2.3 ± 0.6	2.4	2.1 ± 1.1	1.6
2	3.1 ± 0.4	3.4	2.9 ± 0.8	3.8
3	3.2 ± 0.2	3.4	3.3 ± 0.4	3.2
4	2.5 ± 0.2	2.4	0.4 ± 0.1	0.4
5	–2.0 ± 0.1	–1.9	–2.8 ± 0.2	–6.7

We can now use the fact that the tilt is linear and interpolate the fractional shift to any other wavelength. In addition, the differential extinction between any two wavelengths is derived from the assumed extinction law, as shown in section 4.4.1. It is important to note however that the process of shifting different amounts for different lines, implies that the intensity line ratios will be calculated at *fractionally* different spatial positions. However, this does not pose a problem in interpreting the line ratios since the H_2 excitation conditions have been shown to vary smoothly on smaller 1.5″ scales (cf. Fig. 4.5). The corrected line ratios are shown in Table 4.9. These ratios have been normalised to the ratios expected from a 2000 K slab of gas. The reason for choosing 2000 K is because this seems to be the excitation temperature that is derived from the 1-0 S(1) / 2-1 S(1) line ratio in most shocked sources and is 2100 K ± 300 K for HH7. This normalisation choice is convenient because it allows a direct comparison of the physical processes that determines the local distribution of levels. From inspection of Table 4.9 we immediately see that all line ratios are greater than 1, with higher ratios from lines of higher energy levels. This deviation implies that there is hotter shocked gas than in a constant temperature Boltzmann distribution. In the next section, these data are analysed and the implications for the different shock models are discussed.

4.5. Discussion

Both planar J- and curved C-type shock models have been successful in explaining the slope of the data towards the high excitation end of the (N_j/g_j vs. E_j) diagram. Planar J-shocks, however, predict very narrow line profiles and are inconsistent with the broad velocity widths observed for the H_2 lines in HH 7 (Carr 1993; Zinnecker et al. 1989). Carr (1993) has found that the velocity field observed in the H_2 lines is that expected for a bow-shock structure. In addition, the breadths of these lines are found to have a FWHM of ≈ 40 km s^{-1}, typical of other HH objects (Zinnecker et al. 1989). The model investigated here for HH 7 is of a bow shock which probably results from the interaction of a collimated neutral wind from the young stellar object SSV13, with the surrounding molecular material (Rodríguez et al. 1990). This view is also consistent with the Hα velocity structure (Solf and Böhm 1987). Fig. 4.7 shows a schematic view of the bow structure proposed for HH 7.

The similarity of the H_2 line ratios shown in Tables 4.4 and 4.9 for all positions in HH7 is demonstrated in Table 4.10. We have fitted the slope on the (N_j/g_j vs. E_j) diagram for the high-excitation data points (v=2,3 and 4), with an exponential function of the form: $f(E_j) = \alpha \exp(\beta E_j)$. Typical fits are shown in Fig. 4.8 for rows 34 and 32. All data is consistent with a single average slope of 2.3 ± 0.2. The implication of this result for the different shock models is investigated next, by studying the emission properties from a J-type bow shock and from a C-type bow shock.

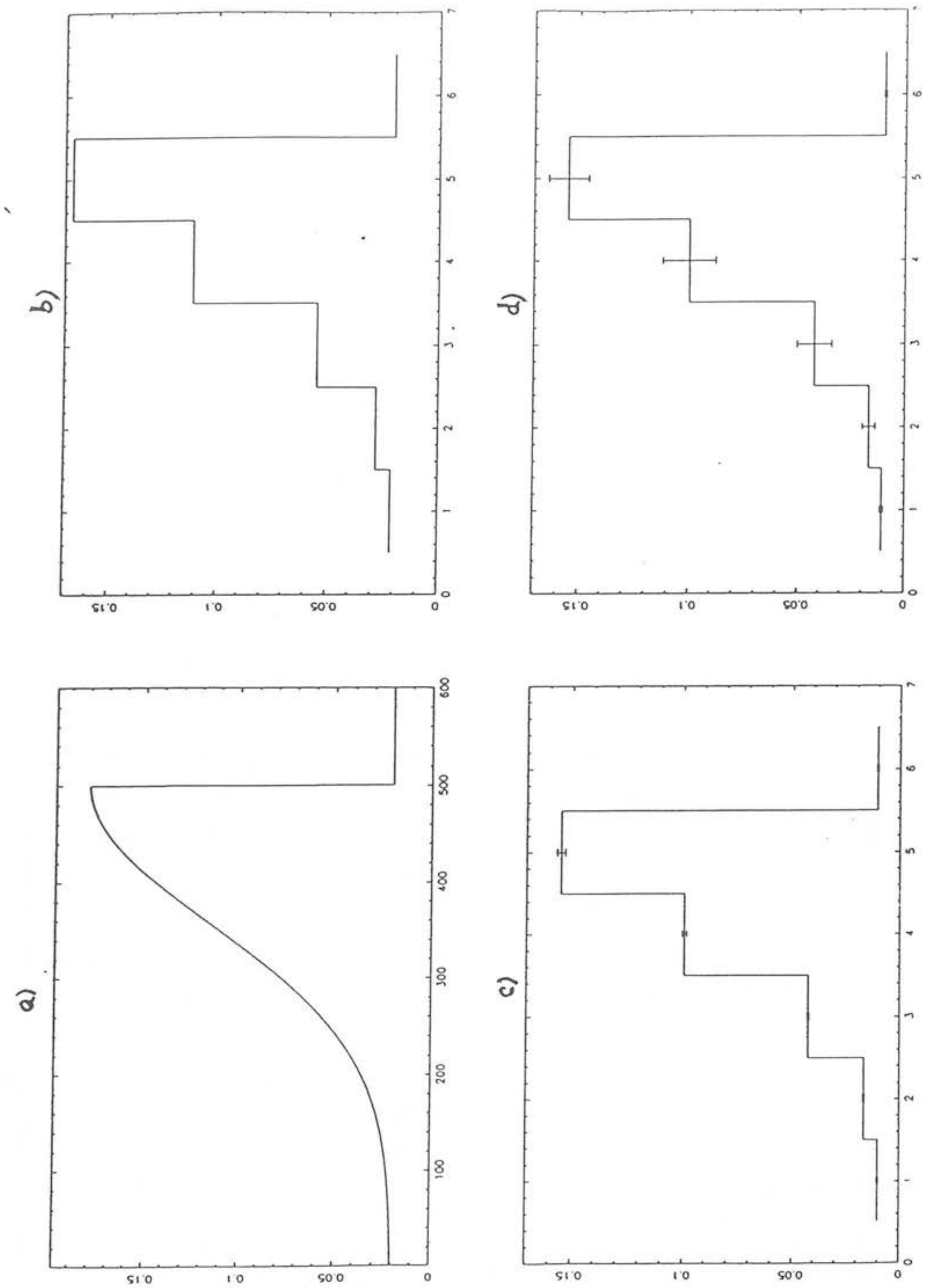

FIGURE 4.5: Emission model for the on-axis slit position; (a) Spatial profile of the 1-0 S(1) emission distribution; (b) Binned emission profile for first guess parameters; (c) Observed 1-0 S(1) emission profile and (d) Minimum χ^2 fit.

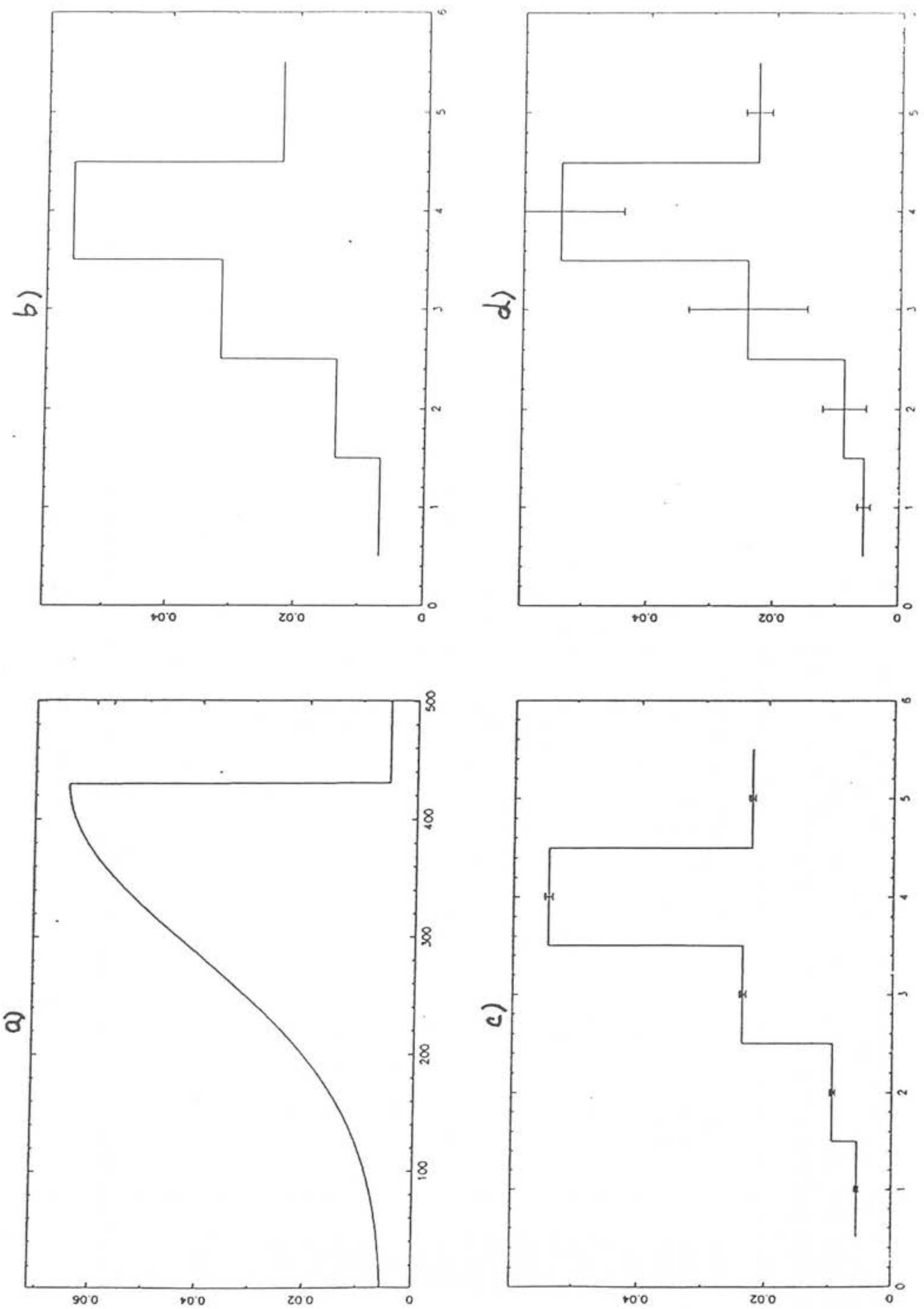

FIGURE 4.6: Diagrams similar to Fig. 4.5 but for the off-axis slit position.

TABLE 4.9: H_2 column density ratios for the 3″ data set

Line	Energy	On-axis slit position				Off-axis slit position	
name	(Kelvin)	Row 31 bin 1	Row 32 bin 2	Row 33 bin 3	Row 34 bin 4	Row S31 bin 3	Row S32 bin 4
1-0 S(1)	6956	1.00 ± 0.00	1.00 ± 0.00	1.00 ± 0.00	1.00 ± 0.00	1.00 ± 0.00	1.00 ± 0.00
1-0 S(2)	7584	1.24 ± 0.38	1.15 ± 0.29	1.13 ± 0.16	1.15 ± 0.09	1.25 ± 0.60	1.16 ± 0.25
3-2 S(5)†	20856			8.74 ± 1.79	8.54 ± 0.91		6.06 ± 2.45
2-1 S(3)	13890	1.35 ± 0.43	1.27 ± 0.30	1.52 ± 0.20	1.44 ± 0.09	0.98 ± 0.46	0.95 ± 0.21
3-2 S(4)†	19912			16.16 ± 5.43	24.55 ± 7.14		13.32 ± 10.28
2-1 S(2)	13150	2.14 ± 0.99	1.76 ± 0.47	1.60 ± 0.24	1.59 ± 0.14	0.88 ± 0.57	0.88 ± 0.30
3-2 S(3)	19086	6.97 ± 2.93	4.92 ± 1.31	5.63 ± 0.78	4.34 ± 0.48	3.54 ± 1.92	3.51 ± 1.14
1-0 S(0)	6471	1.06 ± 0.17	1.02 ± 0.17	1.00 ± 0.11	1.10 ± 0.08	1.04 ± 0.35	1.03 ± 0.17
2-1 S(1)	12550	1.16 ± 0.23	1.06 ± 0.18	1.22 ± 0.13	1.17 ± 0.09	0.97 ± 0.32	0.84 ± 0.15
3-2 S(2)	18386	11.52 ± 5.07	15.18 ± 4.42	3.43 ± 0.91	5.87 ± 0.77		4.34 ± 1.63
4-3 S(3)	23956		39.20 ± 11.54	22.24 ± 5.36	14.44 ± 6.08		11.07 ± 9.38
2-1 S(0)	12095	2.74 ± 0.68	1.29 ± 0.28	1.58 ± 0.20	1.52 ± 0.19	1.11 ± 0.45	1.43 ± 0.35
3-2 S(1)	17818	3.52 ± 1.92	4.02 ± 0.82	4.37 ± 0.60	3.45 ± 0.58	1.79 ± 1.65	3.71 ± 0.99
1-0 Q(1)‡	6149	1.00 ± 0.12	0.99 ± 0.12	1.00 ± 0.09	1.05 ± 0.11	1.12 ± 0.28	1.06 ± 0.20
1-0 Q(2)‡	6471	1.19 ± 0.15	1.18 ± 0.15	1.14 ± 0.11	1.17 ± 0.12	1.38 ± 0.35	1.31 ± 0.25
1-0 Q(3)‡	6956	0.99 ± 0.11	0.98 ± 0.12	1.00 ± 0.09	1.00 ± 0.11	1.04 ± 0.26	0.97 ± 0.19
1-0 Q(4)‡	7584	1.10 ± 0.14	1.12 ± 0.14	1.10 ± 0.10	1.15 ± 0.13	1.25 ± 0.30	1.21 ± 0.24
1-0 Q(5)‡	8365	0.58 ± 0.13	0.55 ± 0.07	0.66 ± 0.06	0.76 ± 0.10	0.57 ± 0.17	0.40 ± 0.09

Notes: For each row position, the first value gives the line ratio (relative to the 1-0 S(1)) and the second value is the 1σ uncertainty.

† These lines are blended with other brighter lines in the spectrum. The 3-2 S(4) is blended with the 1-0 S(1) and the 3-2 S(5) is blended with the 2-1 S(3) and so they are not used in the analysis.

‡ The 1-0 Q-branch lines are blended in the spectra at this resolution and are not used in the main text analysis.

TABLE 4.10: The slope in the high-excitation lines

Data set	Position (row no.)	Slope† β	Average Slope‡
3 arcseconds (On-axis)	32	2.4 ± 0.8	2.3 ± 0.1
	33	2.6 ± 0.3	
	34	2.3 ± 0.2	
	35	2.2 ± 0.2	
3 arcseconds (Off-axis)	S31	1.6 ± 0.4	2.3 ± 0.2
	S32	2.4 ± 0.3	
1.5 arcseconds	32	2.2 ± 0.3	2.2 ± 0.1
	33	1.9 ± 0.2	
	34	1.9 ± 0.3	
	35	2.5 ± 0.2	

Note: †The slope β is calculated from an exponential fit to the column density ratios: $f(E_j) = \alpha \exp(\beta E_j)$ in the high-excitation levels v=2,3 and 4. ‡The average slope is the weighted mean of the values to the left. Refer to Fig. 4.10 for row positions.

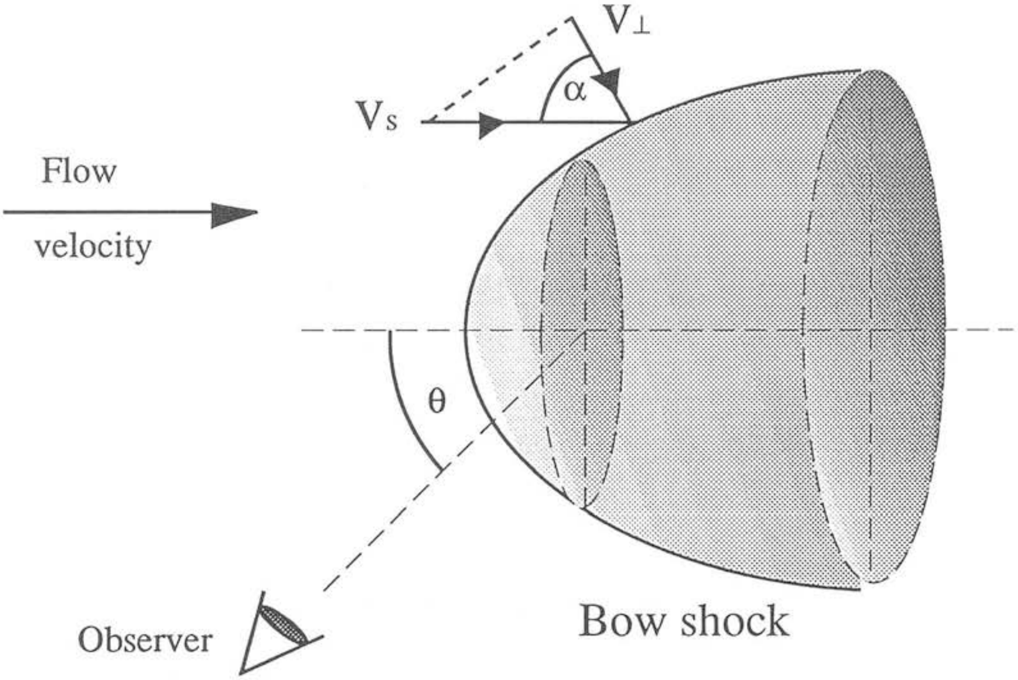

FIGURE 4.7: Sketch of the bow shock geometry. Molecular hydrogen dissociates in the area around the apex. The observer lies in the paper plane at angle θ to the horizontal-axis. The angle of incidence of the flow onto the bow surface is $\alpha = \cos^{-1} (V_\perp / V_S)$.

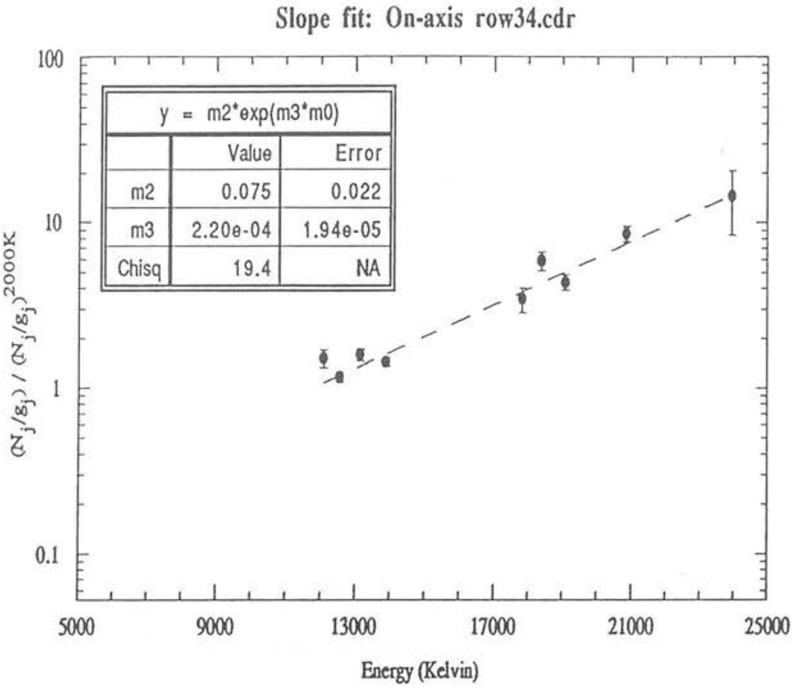

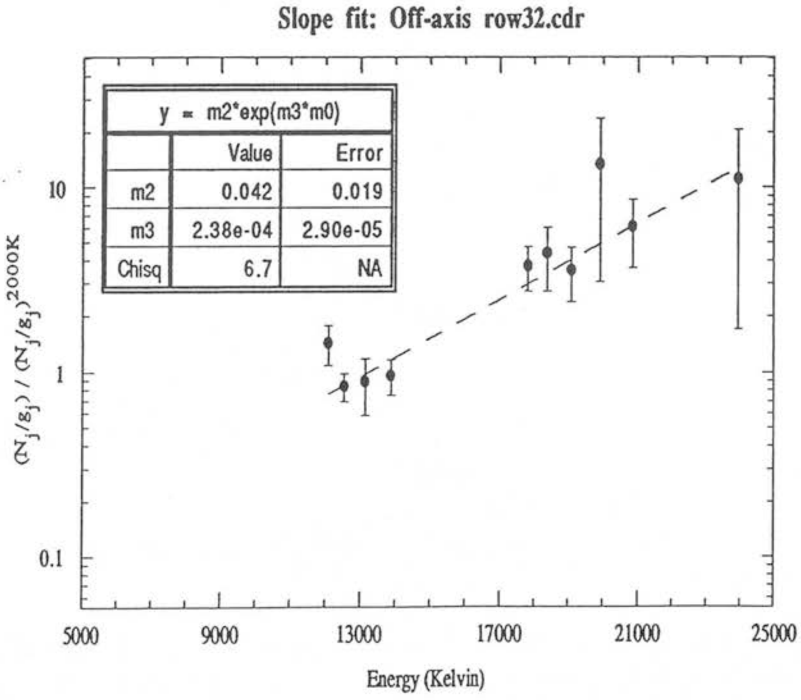

FIGURE 4.8: Typical fits to the slope in the high excitation lines of H_2. The fits for all data are consistent with a single average slope of 2.3 ± 0.2.

4.5.1 The Bow J-shock model

In this model, we assume that two J-shock cooling zones are located in the line of sight; one on each side of the curved surface of the bow. Further, we assume that the bow is transparent to the radiation of H_2 and that any pixel has contribution of the emission from the near and far emitting bow sections. This results directly from the fact that the H_2 radiation is optically thin for typical molecular gas densities ($n \approx 10^{4-6}$ cm^{-3}; see chapter 1). We can use a planar J-shock description for each pixel position as long as the thickness of the cooling layer is not greater than the projected pixel size. At the assumed distance for HH 7 of 350 pc (Herbig and Jones 1983), the 1.5″ pixel size subtends a projected length of 0.003 pc or 7.9×10^{15} cm. J-shocks have typical thicknesses $< 10^{15}$ cm and therefore would appear unresolved at our spatial resolution. This validates the planar approximation. Fig. 4.9 shows a schematic representation of this structure and shows the two H_2 emitting sections of the bow that are seen in the line of sight.

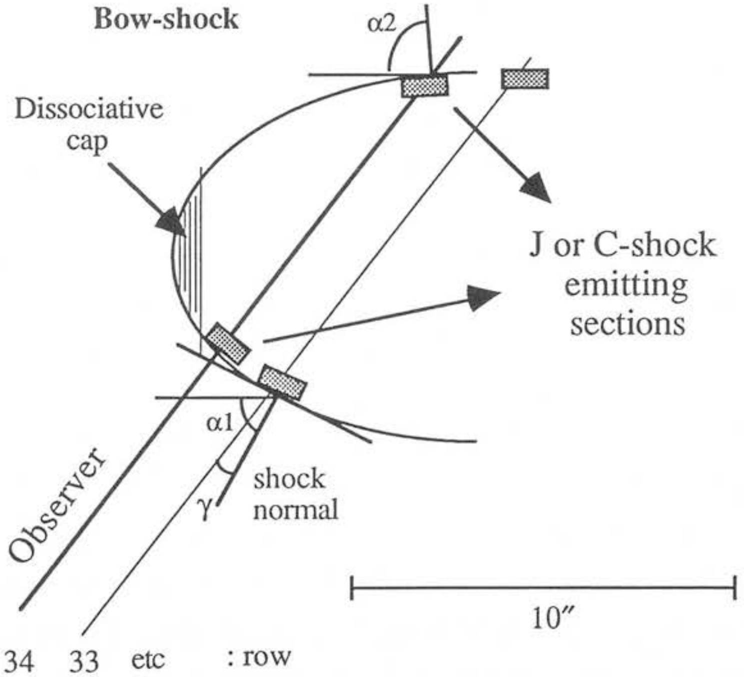

FIGURE 4.9: A cut through the bow structure in Fig. 4.7 showing the two sections of the bow that contribute to the line emission in any line of sight. Two lines of sight corresponding to rows 33 and 34 are shown by two straight lines crossing the bow diagonally.

The H_2 emission from Herbig-Haro 7 has been modelled using the simple J-shock model developed by Brand et al. (1988). In this model, the H_2 emission arises from the recombination region behind a non-dissociative J-shock front. This hydrodynamic model of a shock wave propagates supersonically in a molecular medium with a negligible magnetic field at a speed not greater than 25 km s^{-1} (dissociation limit, Kwan 1977). The gas is accelerated to near the shock speed and compressed by the inverse of that factor (thus conserving mass flux) in a scale length of the order of the collisional mean free path. The temperature peaks just behind the shock front, which is followed by a recombination region where the gas cools by dissociation to about 4000 K and then by radiation of molecular species (H_2, CO). Although this model ignores H_2O cooling, which is predicted to form in the post-shock dense gas, it has proved successful in explaining the observations at peak 1 in OMC-1 (Brand et al. 1988) and the in the SNR IC 443 (Moorhouse et al. 1990a).

The planar J-shock model is pressure sensitive with a high pressure reducing the column densities in the higher energy levels compared to the lower levels. This is reflected in the slope of the high energy part of the N_j/g_j vs. E_j curve. High pressure increases the relative contribution to cooling of H_2 dissociation and depresses the column density of levels with large E_j. The smooth run of N_j/g_j vs. E_j establishes in a model independent manner the local thermal nature of the excitation. The obliquity of the shock front (see Fig. 4.7) affects the strength of the J-shock by reducing the flow shock velocity: $V_\perp = V_s \cos \alpha$, where V_s is the flow velocity and α is the angle of incidence of the flow onto the bow surface. In the bow tail, for example, the angle α is large and indicates a small shock strength: $\rho V_\perp^2$. Fig. 4.10 shows the data from Table 4.4 (row 34) on a N_j/g_j vs. E_j diagram plotted together with selected J-shock models. The minimum χ^2 fit is shown by the small dashed line and has a pressure P $= 6 \times 10^{10}$ K cm^{-3} ($n = 2 \times 10^6$ cm^{-3}) for a typical shock velocity $V_s = 15$ km s^{-1}. This best fit pressure is also consistent with all other low signal-to-noise data since the slope has been shown to be nearly identical (see Table 4.10). From Fig. 4.10 we see that no single J-shock model is capable of reproducing the slope of the data points towards the high excitation lines ($T \geq 10000$ K) and therefore one cannot fit simultaneously the low and high-excitation lines.

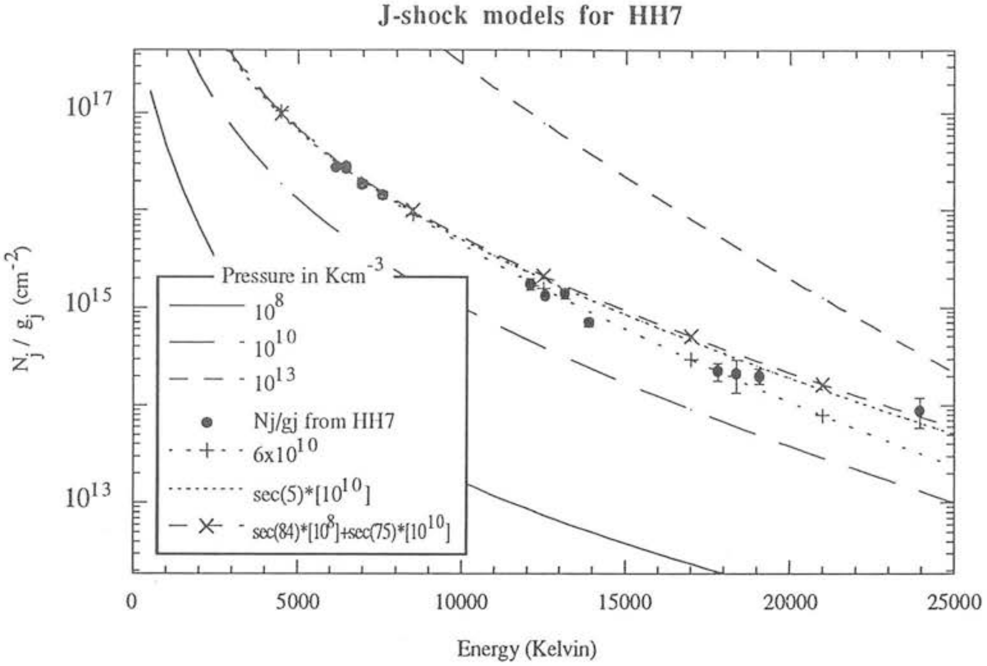

Figure 4.10: Column density vs. energy (Nj/gj vs. Ej) diagram showing the data from row 34 (1.5″ data set) superposed with selected J-shock models.

We now demonstrate that an oblique J-shock has the same observable emission properties as a non-oblique one. The column density (divided by the level degeneracy) of any H_2 line can be written as:

$$N_j/g_j = n_j/g_j \times L_j, \tag{4.10}$$

where L_j is the thickness of the layer emitting the line j. An oblique J-shock will be seen at an angle γ, which is the angle between the line of sight and the normal to the shock front. Thus, we have :

$$L_j = D_j \sec \gamma, \tag{4.11}$$

where D_j is the thickness of a non-oblique shock and sec γ is the factor that relates both line of sight pathlengths (or column densities) observed through the shock. This simple argument shows that despite predicting different absolute column densities (a factor sec γ larger), any oblique J-shock model will yield the same H_2 line ratios as the equivalent non-oblique model. Thus, the effect of the factor sec γ on the column densities of Fig 4.10 is to shift the line models vertically without affecting the slope. An oblique J-shock model with pressure $P = 1 \times 10^{10}$ K cm^{-3} and sec $\gamma = 5$, or $\gamma = 78$ degrees, is shown in Fig 4.10 by the short dashed line for comparison.

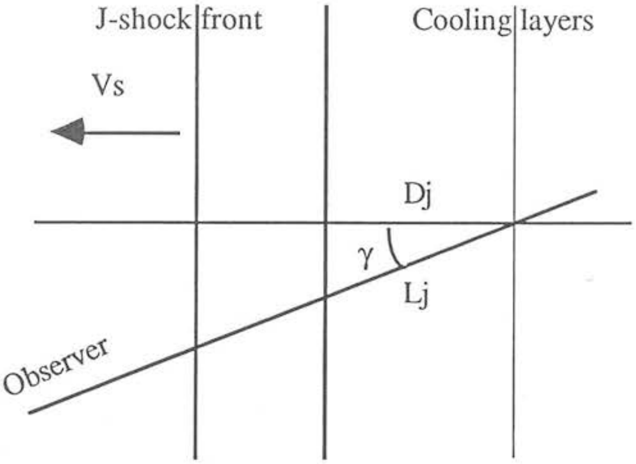

This model seems to fit better the high-excitation lines but fails to predict accurate intensities for the brighter v=2 lines (data points at ≈ 13000 K). Likewise, a combination of two oblique J-shocks has the same signature of a single J-shock and does not improve the fit as is shown in Fig. 4.10 by the dashed line with crosses, which corresponds to the sum of the column densities predicted from the $P = 10^8$ K cm^{-3} model and the $P = 10^{10}$ K cm^{-3} model. The combination parameters are found by constraining the total 1-0 S(1) column density predicted to be equal to the observed and yields the parameters $\gamma_1 = 75$ degrees and $\gamma_2 = 84$ degrees for the J-shock front obliquities of the near and far shocks (see Fig. 4.9).

The main conclusion from this analysis is that the J-shock cooling function seems to fail to provide the necessary high emission ratio between the high and low excitation lines. A possible explanation might be that of the neglect of an important low temperature coolant, which would reduce the H_2 emission from the excited lower levels. Alternatively, perhaps, this simply means that the J-shock scenario is wrong. We suggest that future observations of other high excitation lines of H_2 with $T_j \geq 25000$ K, will help to clarify this issue. This is currently a difficult target since an unfeasibly large amount of telescope time is still necessary to be able to detect the very faint lines using the present state-of-art detector array in CGS4. Future observations using new detectors with improved sensitivities will enable to progress from this situation.

4.5.2 Bow C-shock model

Draine (1980) showed that under certain conditions C-type shocks would occur in the interstellar medium. The thermodynamic structure in these shocks is dictated by the propagation of ion magnetosonic waves ahead of the (neutral) shock which causes a smooth transition in all the dynamic gas variables. This ambipolar diffusion heats and accelerates the gas through ion-neutral collisions over a characteristic length scale much greater than the gas mean free path (in contrast to J-shocks), so that heating and cooling are competing processes throughout. Early planar C-shock models (Chernoff et al. 1982; Draine and Roberge 1982) have failed to explain the H_2 line ratios observed in Orion (Brand et al. 1988). This results directly from the gaussian-like temperature profile throughout the heating/cooling layers of a C-shock transition. Most of the emission from these type of shocks arises from the regions near the peak (maximum) temperature and thus mimics the emission signature of a constant temperature slab of gas. The problem for such a structure is to explain simultaneously the emission from lines of highly ionised species like CIV in addition to low-excitation lines like SII and OI (Hartigan et al. 1987). Moreover, the observed line widths observed in these objects (generally ≥ 200 km s^{-1}), cannot be reproduced by any plane-parallel model.

These difficulties have prompted many workers to model the properties of curved C-shocks, and in special, of bow C-shocks (Schwartz 1978) in Herbig-Haro objects (Hartigan et al. 1987; Raymond et al. 1988; Smith and Brand 1990b; Smith et al. 1991a). The bow shock has been suggested to arise naturally from either around a dense clump of gas ejected into the ambient cloud (Norman and Silk 1979, bullet model), or from a supersonic stellar wind impinging upon a clump of gas in the flow (Schwartz 1978, shocked cloudlet model). The combination of strong UV and modest [OIII] emission arises naturally from the range of effective shock velocities present in a bow shock, while the tangential component of the gas velocity directly produces the large observed line widths (Raymond et al. 1988). The optical and infrared appearance of many Herbig-Haro objects are suggestive of bow-shock structures (e.g. Eislöffel and Mundt 1992, HH 34; Reipurth et al. 1992, HH 111; Solf and Bohm 1987, Hartigan et al. 1989, HH 7-11; Schwartz et al. 1988, HH 43)(Carr

1993, HH 7-11). In addition, the H_2 emission properties calculated for the whole bow, which is assumed to be composed by a set of planar shocks having effective velocities given by the normal component of V_S at each point along the bow surface, have been shown to explain successfully the observed line ratios and line widths from several objects (Smith and Brand 1990a).

The axi-symmetric 2-D modelling of the C-shock structure by Smith (1990a) has shown that the H_2 line ratios are mainly sensitive to the bow shape and the cooling function. In addition, the H_2 line ratios are shown to be independent of the bow velocity once it is greater than the breakdown velocity (velocity at which H_2 dissociates; 40–50 km s^{-1} for high Mach flows). In this configuration, the emission is a weak function of the shock velocity, with the higher shock speeds shifting the emitting section towards the tail of the bow surface, which thus produces the same temperature distribution and conserves the same global H_2 line properties. Hence, it has become urgent to calculate the properties from individual sections of the bow structure to test the predictions of current C-type bow shock models for these objects. The high spatial resolution provided by CGS4, enables us to present the first observations of the H_2 line emission from several positions on the HH 7 bow that will be used to explore and constraint the parameter space of current bow C-shock models. We expect that future observations of atomic and ionic species at comparable spatial and spectral resolution will further test these models.

4.5.2.1 The structure of the bow C-shock

In a bow shock, the normal component of the shock velocity varies along the bow surface and determines the local H_2 excitation properties. The very oblique shock in the tail of the bow (small normal velocity component) produces the cooler emission whilst the hotter emission arises in the stronger shocks near the apex of the bow. For shock speeds greater than that above which H_2 is dissociated ($\approx$ 40-50 km s^{-1}), the bow consists of a leading dissociated cap (cf. Fig. 4.9) that can be described by a J-shock followed by a C-shock tail where it is assumed that the ionised fraction remains low and the magnetic field is dynamically important (Smith and Brand 1990b). The optical and infrared appearance of HH 7 suggests a structure of this type: a tilted bow (Hartigan et al. 1989). The relative shift observed between the optical and infrared emission peaks of $\approx 4''$ (Hartigan et al. 1989) can be accounted for by the projection of the bow on the plane of the sky (Smith 1991a, see Fig. 3) and suggests that HH 7 is a fast moving bow at 30–45 degrees to the line of sight. This also implies a confinement of the optical emission region within the shocked molecular gas, which is consistent with the fact that the H_2 emission region is more broadly extended from the bow shock axis than the [S II] emission (Stapelfeldt et al. 1991).

Using the analytic formulae given in Smith et al. (1991b), we have calculated the H_2 emission properties from a bow C-shock and mapped its emission in the plane of the sky to compare with the infrared maps. This mapping exercise is similar to that presented by Smith (1991a). The emission from an individual section of the bow, represented by the projection of the pixel in the plane of the sky, can be approximated by a single C-shock. The use of the planar C-shock approximation anywhere over the bow surface remains valid as long as the C-shock front (radiative zone) is much smaller than the typical size of the bow, i.e. every H_2 emitting section is considered independent of each other and does affect the adjacent section. Since the projected length on the sky of 7.9×10^{15} cm for the pixel size is comparable or larger than the typical C-shock cooling length of $\approx 10^{15}$ cm (Smith and Brand 1990a), we can expect the planar C-shock treatment to be valid in HH 7. Since the H_2 emission is optically thin, each line of sight through the bow intersects two C-shock sections that contribute to the spectra. Thus, the model to be investigated is a two-component C-shock model for each observed position (pixel).

Smith et al. (1991b) has shown that the most sensitive parameters in determining the H_2 excitation conditions from a bow shock are the angle of the axis of bow to the line of sight and the cooling function. Cooling by H_2O has a stronger dependence on the density ($\propto n^2$) then cooling by H_2 ($\propto n$). Therefore, the H_2O cooling models result in a steeper emission gradient over a smaller bow surface area. This produces an emission *hole*, of decreased H_2 emission, which projected on the plane of the sky, would appear just behind the bow apex for $\theta \approx 40°$. The emission maps generated with H_2O as the dominant coolant are generally not consistent with the appearance of the infrared emission maps which show no *hole* in emission from the bow. Slower shocks ($V_s < 50$ km s^{-1}) can shift the emission towards the bow apex but are generally inconsistent with the broad line profiles. We therefore assume that in these C-shocks the gas cools predominantly by the vibrational-rotational transitions of H_2.

The shock velocity V_s and orientation angle θ, are the two most important physical parameters in the description of a bow shock model. Hartigan et al. (1987) have shown that the bow shock velocity can be simply estimated from a single high-resolution line profile of any low excitation line. They have shown that the full width at zero intesity (FWZI) of all lines should be the same and equal to the bow shock velocity and that the line asymmetry is related with the orientation angle of the bow to the line of sight. One of the major difficulties with this model though, is the observed difference in line widths from different species, e.g. OI, SII; 160 km s^{-1}, Hα; 206 km s^{-1} and OIII; 254 km s^{-1} in HH 2A (Hartigan et al. 1987). A discussion on how to produce these asymmetries is given in Raymond et al. (1988). The observed FWZI of Hα in HH 7 has been observed to be $\approx$ 145 km s^{-1} (Solf and Böhm 1987). Smith et al. (1991a) have demostrated that once the bow is moving faster than the breakdown velocity ($\approx$ 48 km s^{-1}), the H_2 line ratios remain constant. This is simply because the maximum temperature of $\approx$ 4000 K is always reached at some location on the bow. The higher the velocity, the farther away from the leading edge will the C-section arise. The smooth paraboloid then ensures that cooler parts of the flow are still present and in the same proportion to the hot section for all velocities above 48 km s^{-1} (Smith et al. 1991a). So, given the uncertainties described above, we assume a conservative bow shock velocity of 140 km s^{-1} for HH 7, which enables a direct comparison to the line optical fluxes tabulated in the literature for bow shock models (Hartigan et al. 1987).

4.5.2.2 The H_2 emission from the bow C-shock

The contour emission map of the 1-0 S(1) line emission for a bow travelling at $V_s = 140$ km s^{-1} and with the axis of symmetry orientated at $\theta = 40°$ to the line of sight, is presented in Fig. 4.11. On this map, the two CGS4 slit positions are shown superposed on the bow with the pixel positions labelled by their row number (cf. Table 4.10). The size of the pixel bins are chosen to scale with the dimensions of the bow and the spatial resolution used, in accordance with the observed near-infrared map (Stapelfeldt et al. 1991). The emission from each pixel position is parametrised by the two effective shock velocities of the near and far shocks and the relative thicknesses (or column densities) in the line of sight. The maximum temperature reached behind the C-shock is then related to the normal component of the shock velocity by $T \approx T_{max} (V_s \cos\alpha / v_b)^{1.21}$, where $T_{max} = 3900$ K and v_b ($\approx$ 48 km s^{-1}) is the breakdown velocity (Smith et al. 1991a). The bow C-shock section starts when the effective shock velocity is comparable to v_b ($\approx$ 48 km s^{-1}), and occurs at an angle

α_b such that $V_s \cos \alpha_b = v_b$. In the present case, a bow shock velocity of $V_s = 140$ km s^{-1} yields $\alpha_b = 70°$. This constrains the bow shape to a large dissociating cap (J-shock section) followed by a C-shock wing that is nearly flat since $70° \leq \alpha \leq \alpha_M$, where the α_M is the Mach angle, given by $V_s \cos \alpha_M$ = sound speed. The predictions of the H_2 line strengths from this model are simultaneous for all 6 positions (3″ data set) on the bow for any specific bow shape. A paraboloidal bow geometry approximates well the flat sections of the wings and seems to generate H_2 line profiles that agree well the observations (Smith and Brand 1990b). The results from this model are shown in Fig. 4.12 with solid lines. It can be seen that the model seems to fail in two respects. Firstly, it cannot provide enough curvature to fit simultaneously the low ($T < 15000$ K) and high excitation lines ($T > 15000$ K) on the high signal to noise positions. Secondly, the smooth run of column densities versus energy level predicted by the model, cannot explain the scatter observed in the $v = 2$ and $v = 3$ levels. Indeed, this is true for any type of shock, which will inevitably generate thermal populations. Note that the scatter between the points of the $v = 2$ and $v = 3$ levels of the first and second diagrams in Fig. 4.12 seems to be significant since it is greater than the associated 1σ error bars. Thus, though the curvature could be produced by a range of C-shocks in the line of sight, the thermal population of the levels preclude any scatter. This inconsistency, lead us to conclude that shocks alone cannot be responsible for the whole H_2 emission observed. These conclusions apply also to the 1.5″ data set since we have shown in the beginning of this discussion that the slope of the data points are similar for both data sets. We investigate next other possibilities for the origin of the high-vibrational H_2 line emission.

4.5.2.3 The effect of the FUV radiation field: H_2 Fluorescence

Tielens and Hollenbach (1985) have recently discussed the structure and chemistry of photo-dissociation regions (PDR) in which surfaces of molecular clouds are exposed to intense ultraviolet radiation fields. Their calculations show that in such regions, ultraviolet photons with $\lambda > 912$ Å can be absorbed by H_2 in the Lyman and Werner band systems. These absorptions are then followed by fluorescence to the vibrational continuum of the ground state 90% of the time, with dissociation occuring 10% of the time. Infrared H_2 emission is then produced by the cascade down the rotational-vibrational energy ladder of the ground electronic state (see Fig. 4.13).

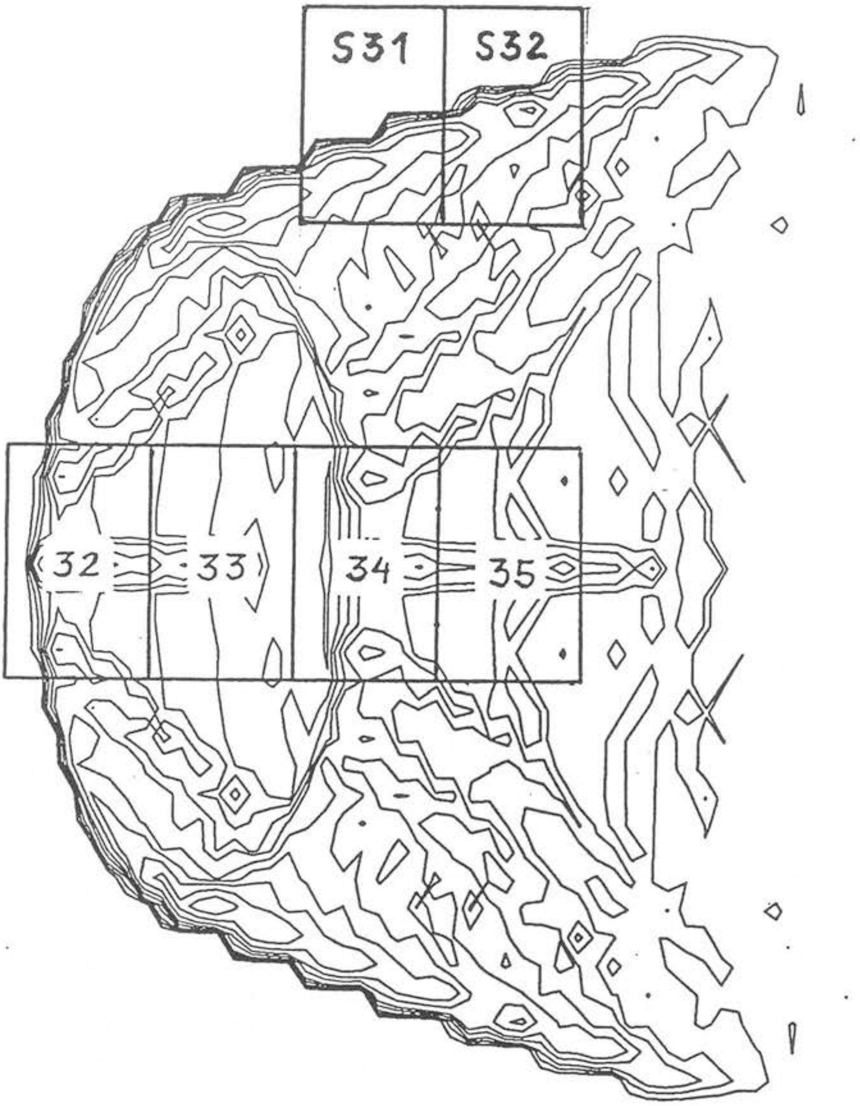

FIGURE 4.11: 1-0 S(1) emission contour map of the projection of the bow on the plane of the sky for a 40 degrees orientation and for a shock velocity of 140 km s^{-1}. Superposed as rectangular boxes are the pixel positions where the H_2 measurements were made. Each pixel has been labelled by the detector row number.

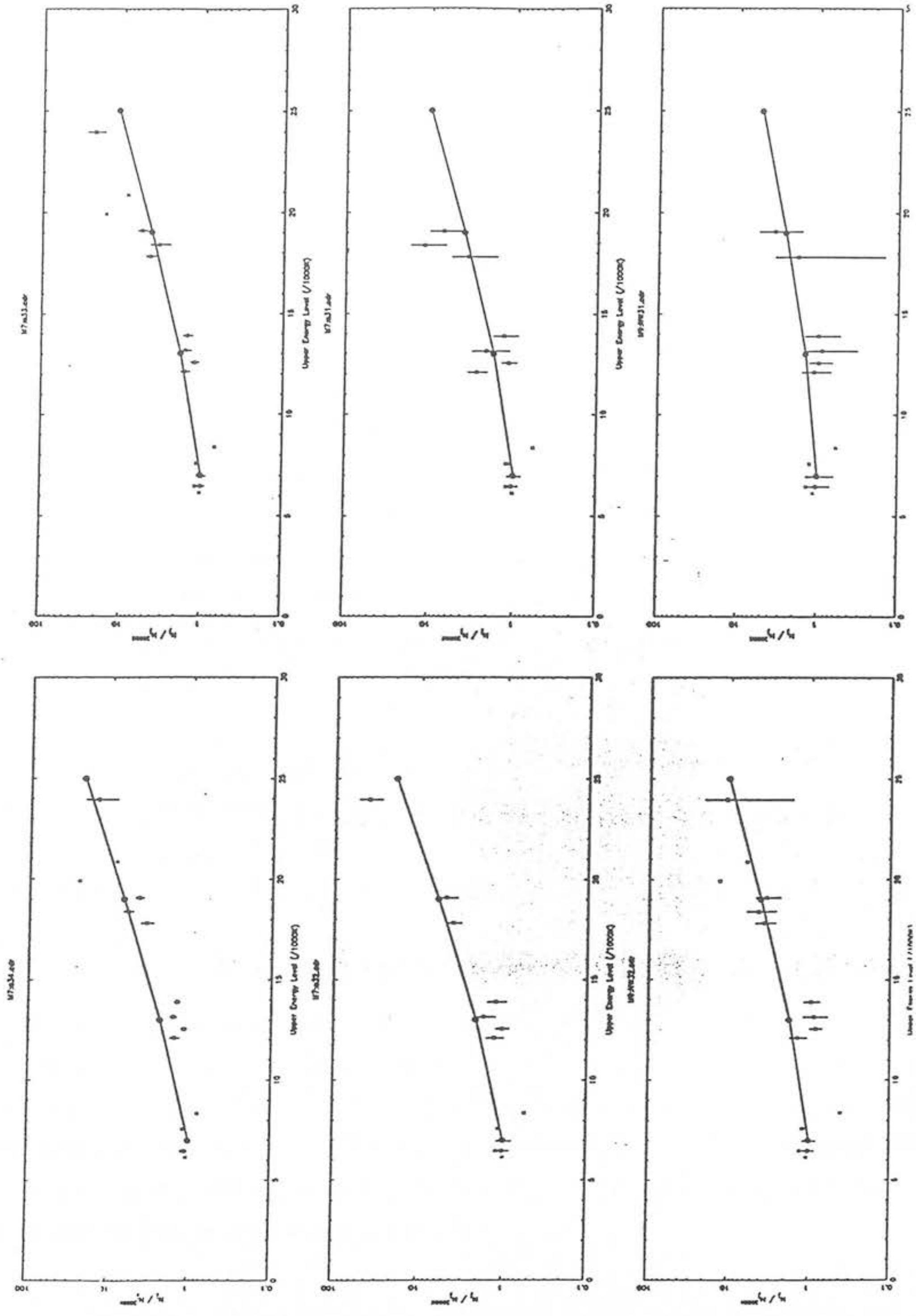

FIGURE 4.12: Column density diagrams for all the six observed positions in HH 7 for the 3″ resolution data set. The solid line is the prediction from the Bow C-shock model discussed in section 4.5.2.2.

In some situations, the H_2 molecules can also be excited by strong emission lines such as HI Lyα (1215.67 Å) and Lyβ (1026 Å) with which there are accidental resonances with the H_2 lines (Black and van Dishoeck 1987). Some likely resonances of Lyα are with the H_2 1-2 P(5) and R(6) lines at 1216.074 Å and 1215.731 Å, respectively, but see also Table 5 of Black and van Dischoeck (1987) for other possible resonances. The ultraviolet fluorescence of H_2 has already been reported from several Herbig-Haro objects (Brown et al. 1981; Schwartz 1983; Schwartz et al. 1985). The importance of this resonance mechanism for the excitation of H_2 line emission in HH 43 has recently been discussed in Schwartz, Cohen and Williams (1987). The line fluorescence mechanism requires the presence of both warm H_2 (2000–3000K), to provide thermal population of the v=2, J=5 ground electronic state, and excited atomic hydrogen, which may or not be mixed with the H_2 gas (Schwartz et al. 1987). A schematic energy level diagram explaining this process is shown in Fig. 4.13. The excited electronic state $B^1\Sigma_u^+$, v'=1, J'=4 is populated by absorption of Lyman α photons from the ground electronic state $X^1\Sigma_g^+$, v"=2,J"=5. The UV Lyman band lines are identified with the P(J"=5) and R(J"=3) branches of the transitions v'=1 $\rightarrow$ v"=3, 6, 7, 8.

Black and van Dishoeck (1987) have suggested that hydrogen molecules formed downstream in the cooling zone can be exposed to a significant flux of Lyα radiation. However, this process is only significant if the radial velocity shift between the Lyα emitting region and the H_2 fluorescence region is small. The Lyα line profile is not known in HH 7 but a reasonable estimate is that of the observed Hα line profile (Solf and Böhm 1987). This profile has a peak velocity of ≈ -50 km s^{-1} and is about two times broader than that of the H_2 1-0 S(1) line profile, which has a FWHM ≈ 50 km s^{-1} and $V_{peak} \approx -4$ km s^{-1} (Zinnecker et al. 1989). Thus, it appears that a significant fraction of Lyα photons (blue wing) can excite the H_2 population. Furthermore, the bright Hα emission observed from HH 7 (Solf and Böhm 1987) appears to favour this scenario, where most of the Lyβ photons are converted into Lyα and Hα (Black and van Dishoeck 1987).

The search for a fluorescent component in HH 7, HH 11 and HH 29, has recently been carried out by Cameron and Liseau (1990) using the International Ultraviolet Explorer (IUE) satellite. No UV H_2 lines from the P and R Lyman branches could be detected in HH 7 by IUE in the wavelength range 1200-3000 Å, and this was attributed to the high dust opacity towards HH 7.

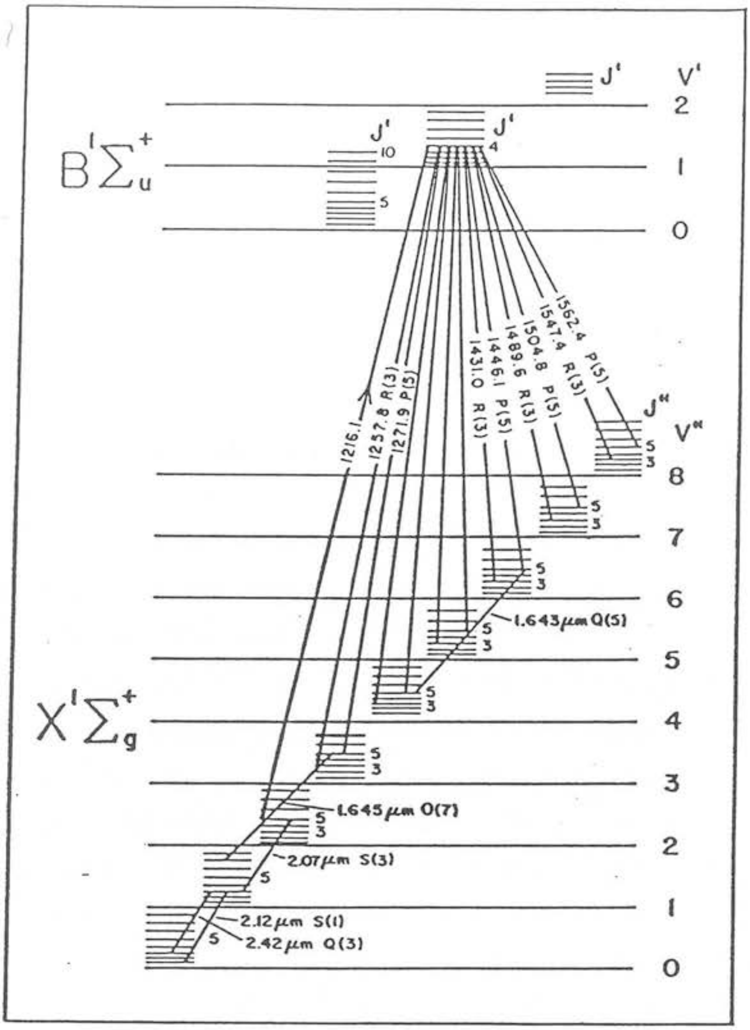

FIGURE 4.13: A schematic diagram of the H_2 line fluorescence mechanism. Shown are the selected v=2-1 and v=1-0 vibrational transitions in the ground electronic state which are produced by thermal excitation. The Lyα pumping transition is seen to populate the v'=1,J'=4 state of the excited electronic state, giving rise to eight Lyman band emission lines observed in the UV for HH 43 by (Schwartz 1983). Adapted from (Schwartz et al. 1987).

However, there is considerable uncertainty about the UV extinction correction used in Cameron's work. In their work, they have assumed the average θ Orionis extinction curve with R=5 and a colour excess $E_{B-V} = 0.55$, which translates into an infrared extinction of $A_K \approx 0.3$. Our derivation of $A_K \leq 2.3$ from the Brγ upper limit (section 4.5), together with the estimate from the v=1-0 S(1)/Q(3) line ratio of $A_K = 2.1 \pm 0.6$ (1.5″ data set) and $A_K = 1.0 \pm 0.1$ (3″ data set), suggests that the extinction in HH 7 is actually higher than that assumed in Cameron's work.

We have investigated the effect of a UV-excited H_2 component superposed on a shocked spectrum using current theoretical models of radiative excitation of H_2 (Black and van Dishoeck 1987, hereafter BvD; Burton et al. 1990, hereafter BHT; Sternberg and Dalgarno 1989) to predict the H_2 line intensities. These models cover different parameter spaces in density, n_0, and intensity of the ultraviolet radiation field, G_0*. The fundamental parameter in these PDR models is the n_0/G_0 ratio, which controls the importance of the collisional processes affecting the distribution of H_2 (Burton et al. 1990). We have taken the intensities predicted for the H_2 fluorescent emission from the BvD and BHT models and calculated the emission from a hybrid model consisting of a shocked H_2 component and a UV-pumped contribution. The parameters to be fitted in this model are the fractional column density of each component, f_1 and f_2, where $N_{total} = f_1.N_{shock} + f_2.N_{fluorescent}$, and the maximum temperatures on the two C-shock sections in each line of sight (rows 33 or 34), T_1 and T_2. The analysis is restricted to rows 33 and 34 of the 1.5″ and 3″ data sets because of the low signal to noise on the other pixel positions. The minimum χ^2 fit results are summarised in Table 4.11 and are determined for each data set and fluorescence models. Column 5 of Table 4.11 shows the significance of the fit for each model based on the reduced χ^2 statistic. The calculated relative fractions of the shocked and fluorescent emission components for model BvD #14 are shown in Table 4.12 for each H_2 line. This table shows that the high excitation lines have significant contributions from H_2 fluorescence; for example the v=3-2 S(1) at 17818 K is excited almost equally by shocks and the FUV radiation field whereas the v=1-0 S(1) at 7000 K is predominantly shock excited (≥ 96%). Transitions from v=2 have intermedium contributions; e.g. in the range 7%–23% for the 2-1 S(1) line at 12550 K. This effect can be seen more clearly in Fig. 4.14 where we plot the relative

---

* Far-UV incident radiation field in units of the interstellar radiation field, equivalent to a one-dimensional flux of 1.6×10^3 ergs s^{-1} cm^{-2} (Burton et al. 1990).

abundances of fluorescence and shocked H_2 against the upper level energy. From a polynomial fit to the fluorescent component, it shown in these plots the difference in the fluorescent contribution expected for the energy levels from 6000 to 25000 K. The population of the lower levels by the fluorescence mechanism differs for the models examined here of BvD and BHT and this can be seen from the different slopes of the fits in Fig.4.14. The total shocked plus fluorescence H_2 emission calculated from this model is plotted in Figs. 4.15-4.22 for comparison with the HH 7 data at two pixel positions: rows 33 and 34. The excellent agreement with the data for the model including BvD fluorescence can be seen from the nearly unity χ^2. The BHT model for fluorescent emission appears not to match so well the data, although it still provides a generally good fit. Overall, we suggest that H_2 fluorescence provides a good match to the data and some possible reasons for the apparent divergence of the predictions of the BvD and BHT models are to be discussed later in this section.

Table 4.11: Fit results for the shocked and fluorescence combined models

Position	data set	Fluorescence Model[a]	χ^2	Prob.[b]	Fig.
	1.5″	BvD #14	1.2	30%	4.15
Row 34	3″	BvD #14	1.2	30%	4.16
	1.5″	BvD #14	2.8	< 1%	4.17
Row 33	3″	BvD #14	1.9	5%	4.28
	1.5″	BHT	2.5	1%	4.19
Row 34	3″	BHT	6.7	< 0.1%	4.20
	1.5″	BHT	4.1	< 0.1%	4.21
Row 33	3″	BHT	3.8	< 0.1%	4.22

Notes: The number of degrees of freedom in these fits is $\nu = 8$, which is calculated from $\nu =$ 10 (no. data points) – 2 (the fluorescent and shock abundances: f_1 andf_2).

a) The fluorescence model parameters are BvD #14: $n=3 \times 10^3$ cm^{-3}, $G_0=10^3$ from Black and van Dishoeck (1987) model 14 and BHT: $n=10^6$ cm^{-3}, $G_0=10^4$ from Burton, Hollenbach and Tielens (1990). The Bow C-shock model parameters (discussed in section 4.5.3) derived from the best fit are: T_1=4000 K (5%) and T_2=2000 K (95%).

b) Prob. gives the probability that the model proposed in that row is correct.

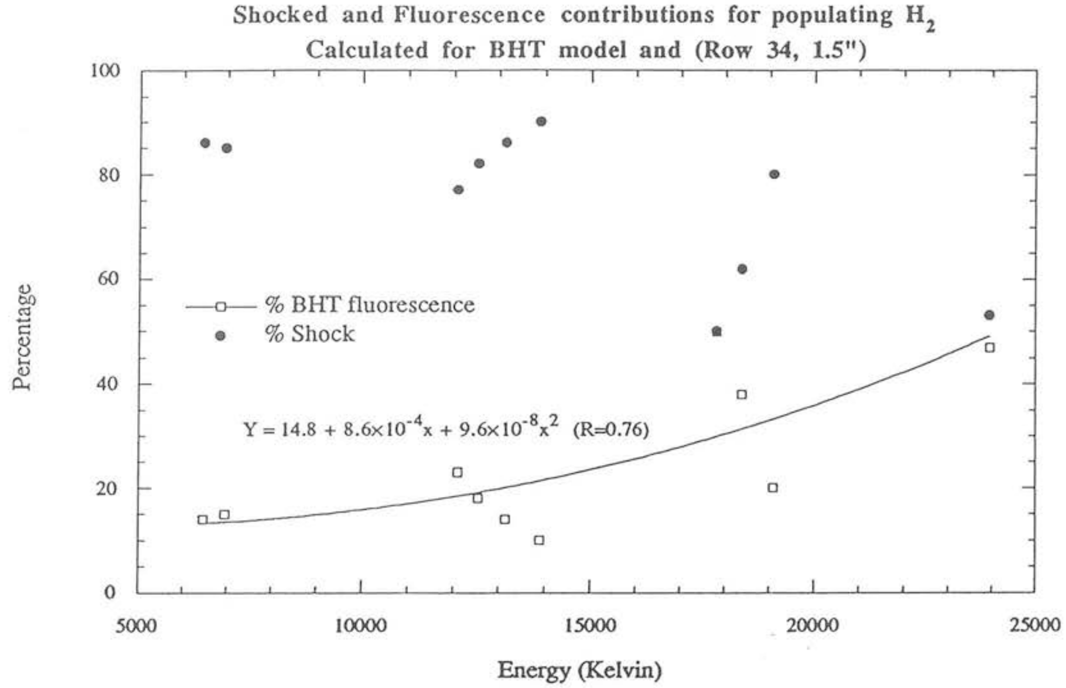

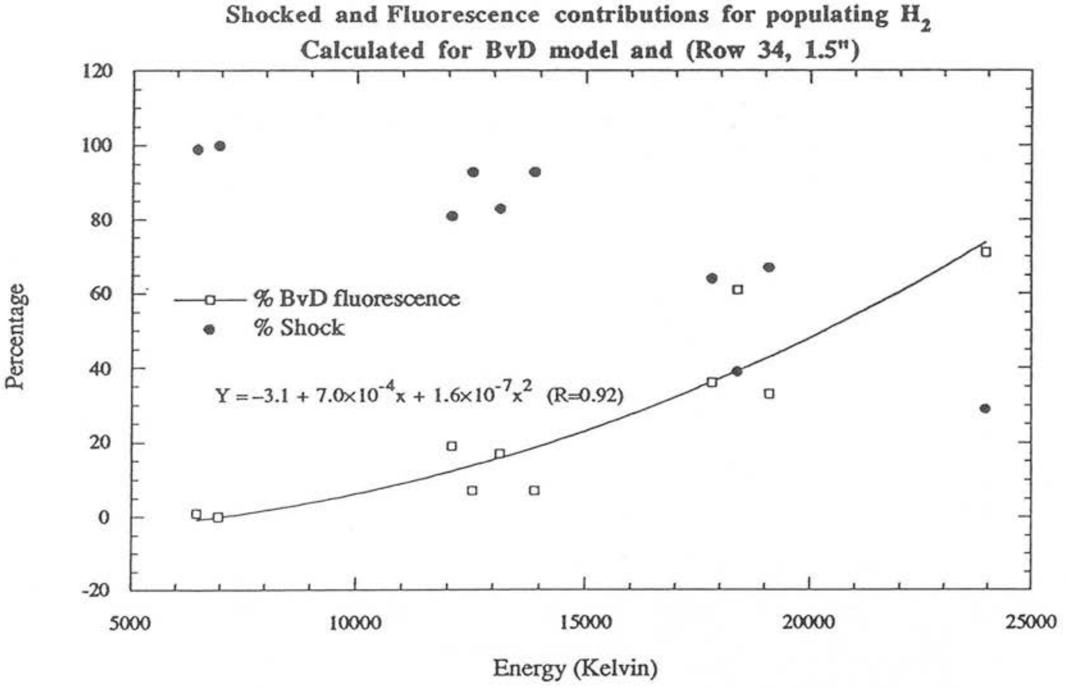

FIGURE 4.14: Relative abundaces of shocked and fluorescent components for models BvD and BHT. The solid line shows a polynomial fit to the trend of the fluorescent component for each PDR model.

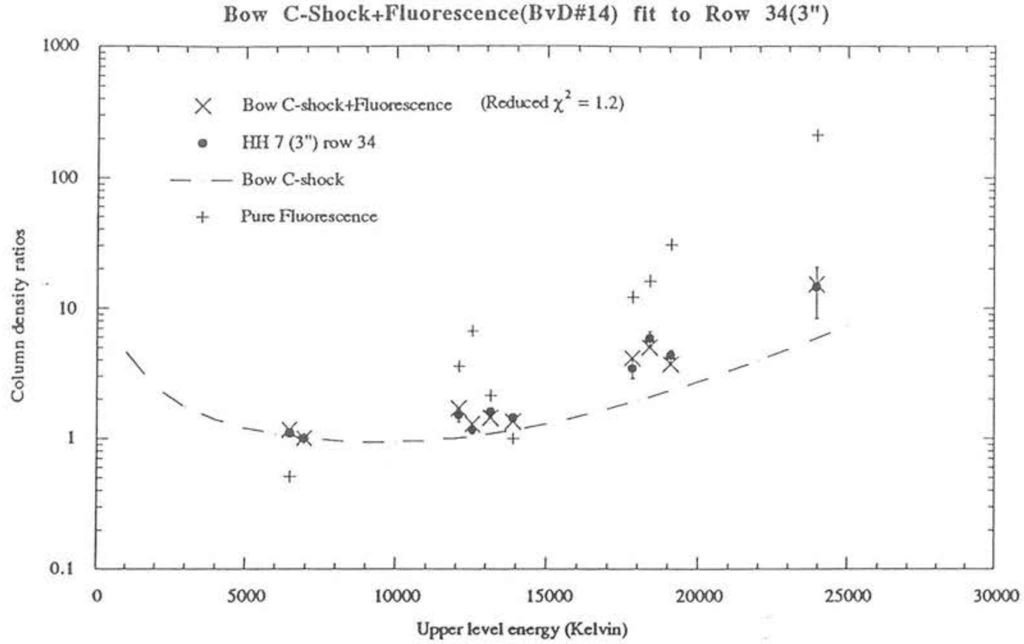

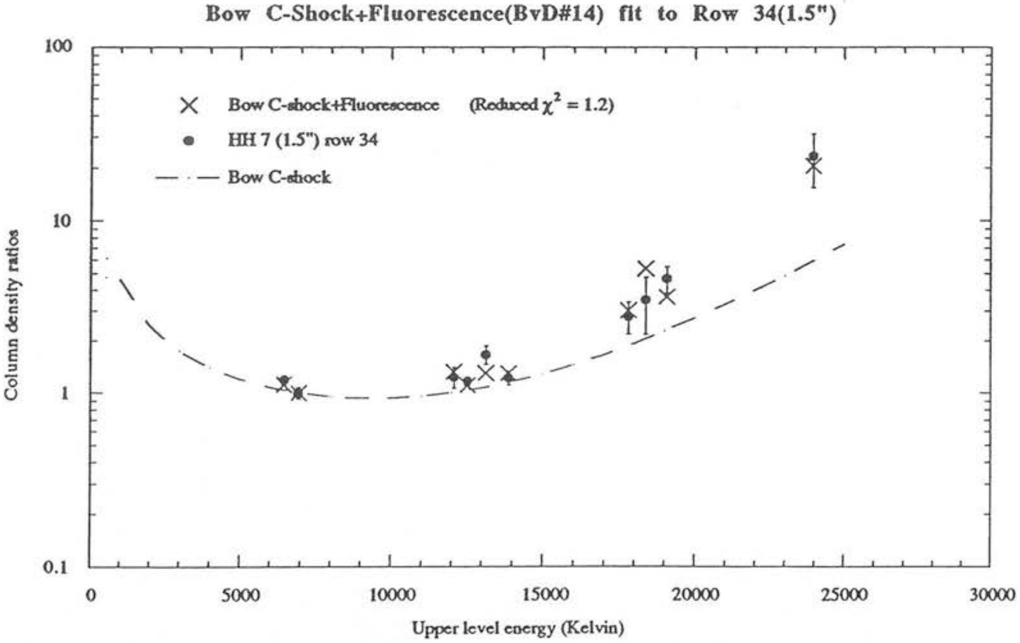

FIGURES 4.15-4.16: Bow C-shock + fluorescence model predictions for the data in rows 33 and 34 of the HH 7 bow for the 1.5″ and 3″ data sets. Refer to Table 4.11.

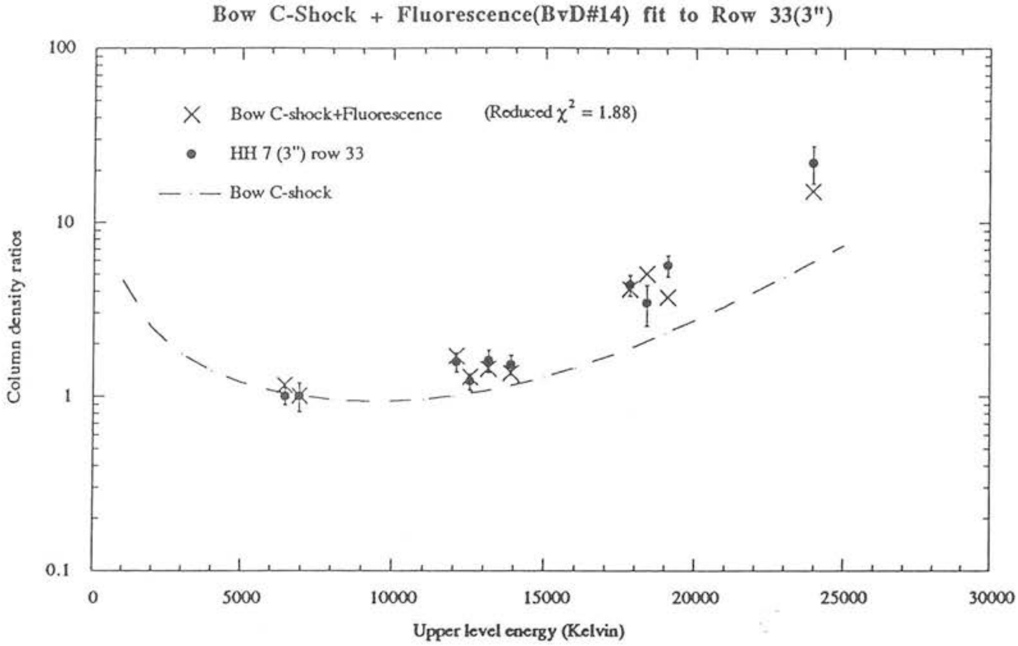

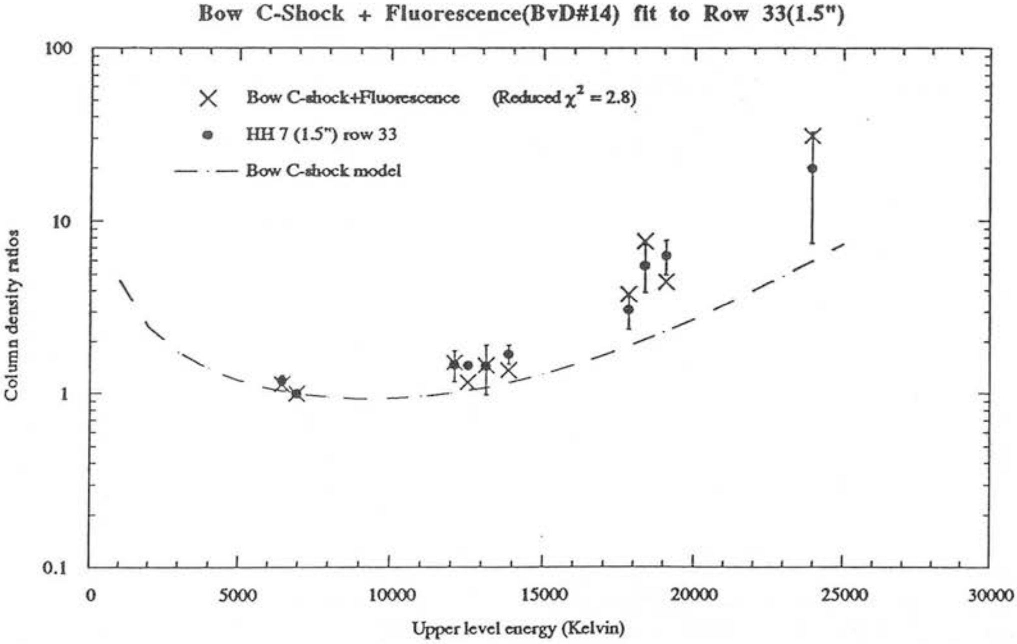

FIGURES 4.17-4.18: Model predictions for HH 7. Refer to Table 4.11.

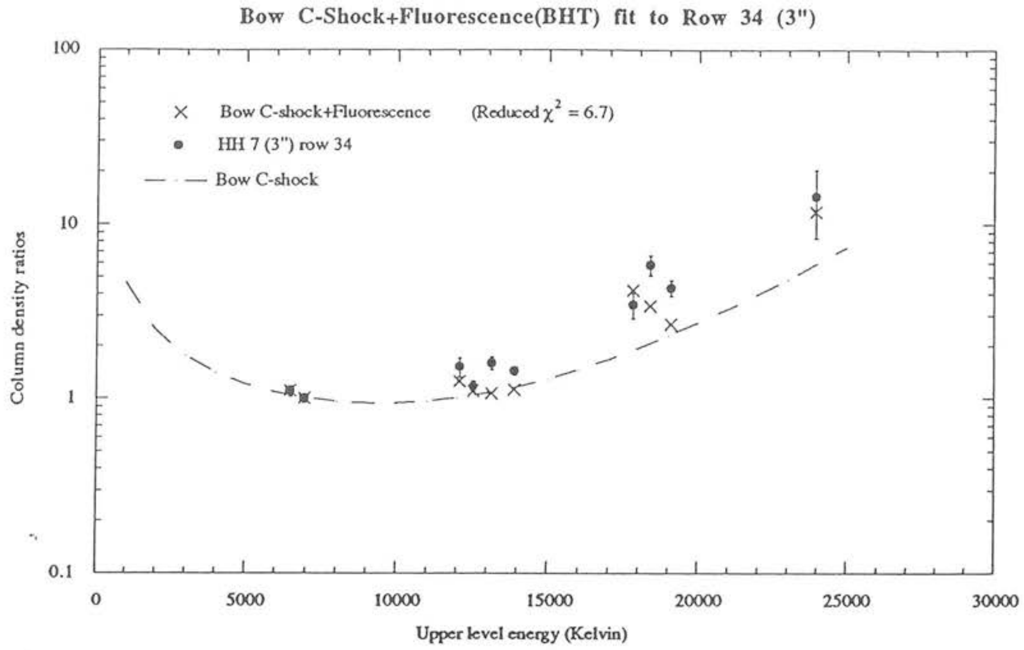

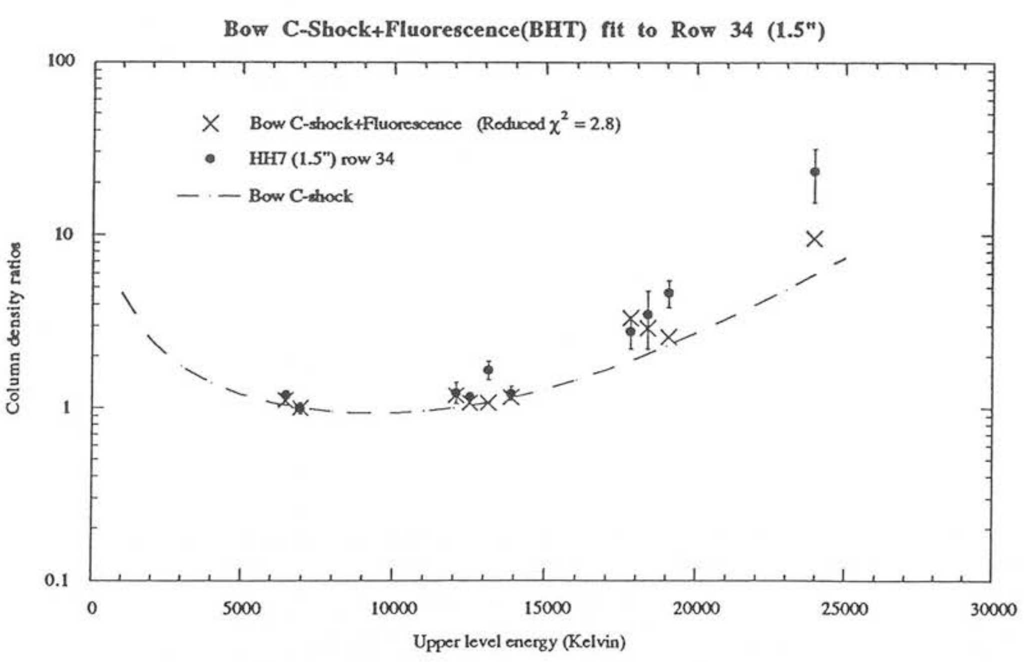

FIGURES 4.19-4.20: Model predictions for HH 7. Refer to Table 4.11.

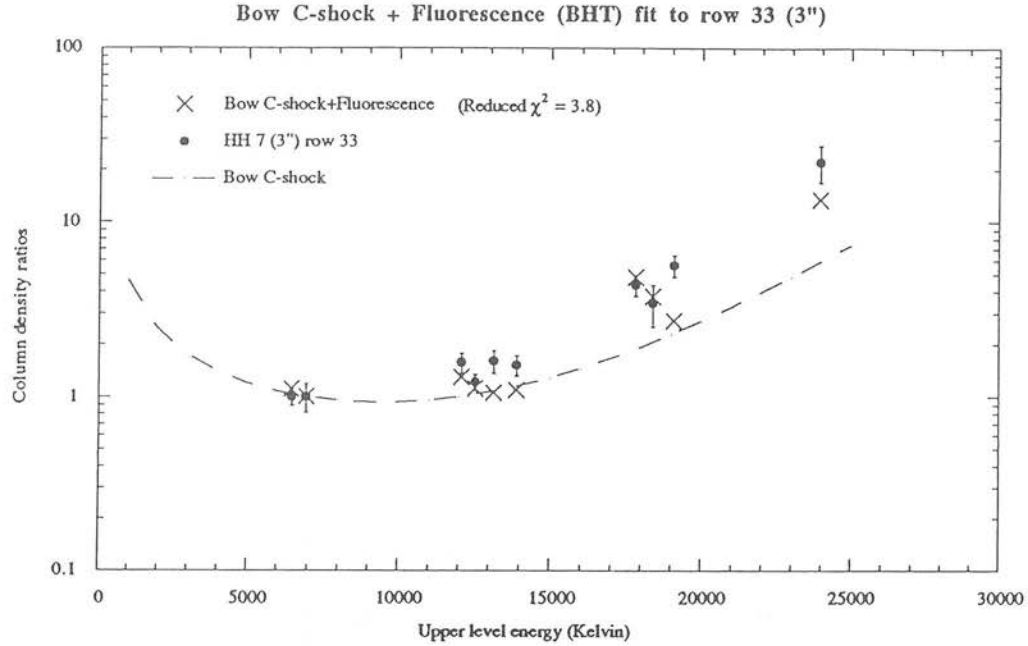

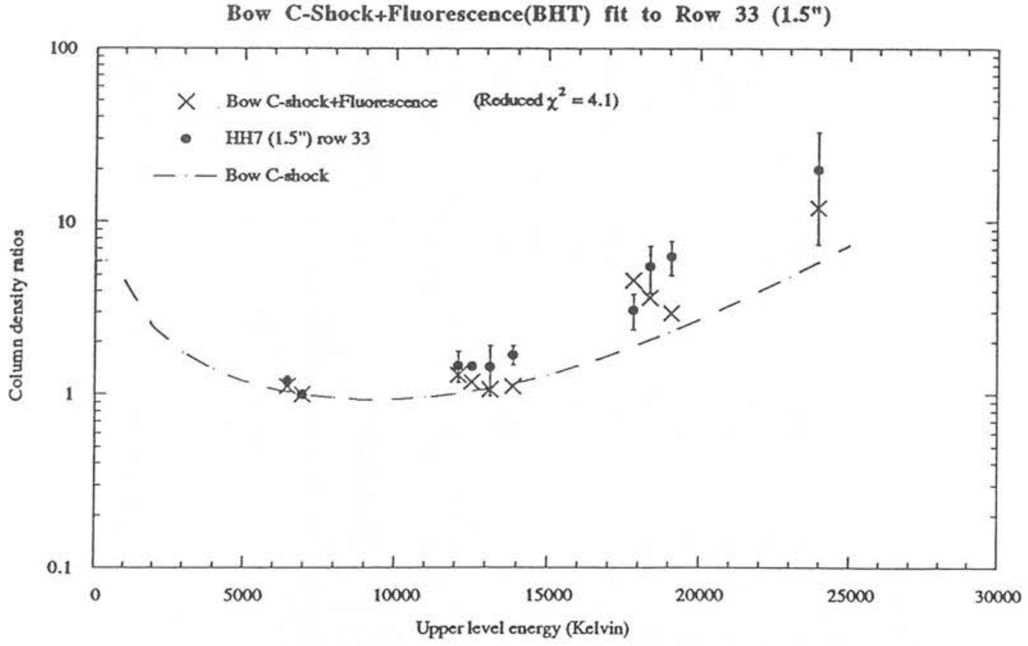

FIGURES 4.21-4.22: Model predictions for HH 7. Refer to Table 4.11.

Table 4.12: Shocked and fluorescent fractions for the combined model

Bow C-shock + Fluorescence (BvD #14) Emission Model

Transition	Energy	Row 33				Row 34			
		3 arcseconds		1.5 arcseconds		3 arcseconds		1.5 arcseconds	
		N_{fl}/N_{Tot}	N_{sh}/N_{Tot}	N_{fl}/N_{Tot}	N_{sh}/N_{Tot}	N_{fl}/N_{Tot}	N_{sh}/N_{Tot}	N_{fl}/N_{Tot}	N_{sh}/N_{Tot}
1-0 S(1)	6956	4%	96%	1%	99%	4%	96%	0%	100%
2-1 S(1)	12550	23%	77%	11%	89%	23%	77%	7%	93%
3-2 S(3)	19086	37%	63%	46%	54%	37%	63%	33%	67%
4-3 S(3)	23956	63%	37%	81%	19%	63%	37%	71%	29%
2-1 S(3)	13890	14%	86%	11%	89%	14%	86%	7%	93%
2-1 S(2)	13150	28%	72%	26%	74%	28%	72%	17%	83%
1-0 S(0)	6471	8%	92%	2%	98%	8%	92%	1%	99%
2-1 S(0)	12095	40%	60%	29%	71%	40%	60%	19%	81%
3-2 S(2)	18386	60%	40%	73%	27%	60%	40%	61%	39%
3-2 S(1)	17818	55%	45%	49%	51%	55%	45%	36%	64%

(cont. of Table 4.12)

Bow C-shock + Fluorescence (BHT) Emission Model

Transition	Energy	Row 33				Row 34			
		3 arcseconds		1.5 arcseconds		3 arcseconds		1.5 arcseconds	
		N_{fl}/N_{Tot}	N_{sh}/N_{Tot}	N_{fl}/N_{Tot}	N_{sh}/N_{Tot}	N_{fl}/N_{Tot}	N_{sh}/N_{Tot}	N_{fl}/N_{Tot}	N_{sh}/N_{Tot}
1-0 S(1)	6956	30%	70%	23%	77%	24%	76%	15%	85%
2-1 S(1)	12550	36%	64%	28%	72%	28%	72%	18%	82%
3-2 S(3)	19086	38%	62%	30%	70%	31%	69%	20%	80%
4-3 S(3)	23956	69%	31%	61%	39%	62%	38%	47%	53%
2-1 S(3)	13890	22%	78%	17%	83%	17%	83%	10%	90%
2-1 S(2)	13150	29%	71%	22%	78%	22%	78%	14%	86%
1-0 S(0)	6471	30%	70%	23%	77%	24%	76%	14%	86%
2-1 S(0)	12095	43%	57%	34%	66%	35%	65%	23%	77%
3-2 S(2)	18386	61%	39%	53%	47%	53%	47%	38%	62%
3-2 S(1)	17818	72%	28%	64%	36%	65%	35%	50%	50%

Notes: N_{fl}/N_{Tot} is the fractional column density (or intensity) of the fluorescent component. Similarly, N_{sh}/N_{Tot} refers to the shocked component.

The origin of the observed H_2 fluorescence has yet to be determined for HH 43 (Schwartz 1983). A possible solution might be that this emission arises from the same shock that is propagating into the molecular cloud with a velocity sufficient to produce partial molecular dissociation. The atomic component of the post-shock gas would then give rise to the low-excitation optical lines. The Bow C-shock model investigated here, has one shock component with a maximum temperature close to the dissociation limit of the H_2 molecules (to provide enough high-excitation line emission) and is therefore capable of producing partial molecular dissociation. In the absence of a continuum source or HII region near HH 7, the FUV continuum produced behind the bow C-shock can affect the shock excited H_2 population (Hartigan et al. 1987). The emission from a planar shock depends on the ionisation state of the gas entering the shock (pre-shock gas), and the bow shock models that have been constructed from them to predict the line ratios and line profiles expected from HH objects are based on either the assumption of complete preionisation or the assumption of local equilibrium preionisation (Hartigan et al. 1987; Raymond et al. 1988). In the equilibrium preionisation models, which generally agree better with the observed widths for the lines, the pre-shock gas is exposed to the ionising radiation produced by the shock and an equilibrium is reached between the number of ionising photons produced in the shock and the number of ionised atoms entering it (Shull and McKee 1979). The transition between neutral and ionised pre-shock gas occurs over a narrow velocity range, $90 < V_s < 120$ km s^{-1}, because of the high efficiency of neutral hydrogen in cooling the gas by means of (non-ionising) Lyman line emission (Raymond et al. 1988). The effect of the ionisation level and magnetic field on the H_2 emission, has been considered by Smith et al. (1991a) and shown to have little influence on the line ratios, as long as dissociation provides the breakdown condition. For high magnetic fields or ionisation fractions, the breakdown is via streaming ionisations, i.e., neutral-ion collisions that lead to runaway self-ionisation and subsequent dissociation (Smith et al. 1991a). From the bow shock models of Hartigan et al. (1987), we derive that for bow shock of velocity 140 km s^{-1}, the Lyα flux is $\approx 9.3 \times 10^{-3}$ erg s^{-1} cm^{-2}. If we assume that some 90% of the Far-UV radiation field from the hot post-shock gas comes in Lyα (Hollenbach and McKee 1979) then, the FUV flux is ≈ 0.01 erg s^{-1} cm^{-2} which translates to $G_0 \approx 6$. However, the densities assumed in Hartigan's model of $\leq 10^3$ cm^{-3}, are far below the critical densities for collisional excitation of H_2 ($n_{crit} \approx 10^{5-6}$ cm^{-3}). Since the luminosity of the optical lines scale linearly with density in this regime (Raymond et al. 1988), we expect that the FUV field in HH 7 can be parametrised with $G_0 = 10^2 - 10^3$. From inspection of Table 4.11, we can see that this value for G_0 is in good agreement with the G_0 parameter used for the H_2 fluorescence models of BvD and BHT and this suggests that the FUV radiation field in HH 7 is of order 0.16–1.6 erg s^{-1} cm^{-2}. Thus, we conclude that a model including both the shocked H_2 emission from a bow structure and a UV-excited H_2 population is necessary to fit the H_2 line ratios in HH 7.

4.5.2.4 The ortho to para ratio

From Figs. 4.15-4.22 we can see that the main difference in the model predictions of the BvD and BHT fluorescence is the scatter on the column densities for each vibrational level. For example, the level v=2 (≈ 13000 K) has a flatter signature in these diagrams for the BHT model whereas it has a saw-like signature for the BvD model. The main reason for this is the different assumed abundances of the ortho (odd J) and para (even J) states of the emitting H_2 molecules. The ortho-to-para ratio gives a measure of the overpopulation of the odd J states relative to the even J states. This ratio is believed to be set in the formation of H_2 on the surfaces of grains and probabily reflects the physical conditions under which H_2 is formed (Duley and Williams 1986; Mathis et al. 1977). The conversions between these states are not radiatively allowed but spin exchange reactions can occur through collisional interactions with H and H^+ while in the gas phase (Dalgarno et al. 1973). If the gas is hot enough (> 300 K), the ortho to para abundance ratio saturates at a value of 3, since collisions will rapidly bring the states to a thermal equilibrium as is the case for shocks. Otherwise, in cold gas (< 50 K) this abundance ratio will depend strongly on the temperature and the timescales for the destruction of the H_2 molecules and the spin exchange reactions (Flower and Watt 1984). In the PDR model of BvD, the ortho to para ratio is assumed to be 1.8, because of the assumed H_2 reformation scheme on the dust grains. The PDR model of BHT, however, assumes this ratio to be 3 to account for the high density PDR environments. The fit results of section 4.5.2.3 suggests that the ortho to para ratio is consistent with a value of 1.8 for the UV excited H_2 population in HH 7. Such low values have been observed in several objects including the M17 region (o/p=1.8), Hubble 12 (o/p=1.7) and NGC 2023 (o/p=2.2) (Chrysostomou 1992). This has strong implications for the formation mechanism of H_2 in PDRs and is being currently investigated.

4.5.3 Alternative interpretations

4.5.3.1 Reformation of H_2 in dissociative shocks

In fast shocks that completely dissociate the H_2 molecular gas ($V_s \geq 45$ km s^{-1}), the H_2 emission arises from the reformation of molecules on the surfaces of dust grains that have not been destroyed (Duley and Williams 1986; Hollenbach and Salpeter 1971). Current models of the H_2 reformation process behind dissociative shocks predict a 1–0 S(1) / 2-1 S(1) ratio of ≈ 2–3 for densities in the range $10^3 - 10^4$ cm^{-3} and for shocks speeds in the range 30–150 km s^{-1} (Hollenbach and McKee 1989). This contrasts with our observed value of 9 in HH 7. In addition, the observed 1-0 S(1) intensity of 1.4×10^{-3} ergs s^{-1} cm^{-2} sr^{-1} at HH 7's emission peak is larger than the larger value predicted by the model of $\approx 10^{-4}$ ergs s^{-1} cm^{-2} sr^{-1}, which occurs for densities $n \geq 10^4$ cm^{-3}.

The reformation time of 10^{17} / n seconds is of order 10^{11} seconds for typical pre-shock gas densities of $10^5 - 10^6$ cm^{-3} assumed here. This time is long compared with the cooling timescale behind a J-shock which is of order 10^8 seconds (Duley and Williams 1986). The cooling time in a C-shock can be roughly estimated as the length of the C-shock transition layer divided by a typical shock velocity of ≈ 50 km s^{-1}, yielding a few × 10^7 seconds. Thus, we expect no significant contribution from emission of reformed H_2 molecules in the observed spectra. Furthermore, the H_2 recombination emission from behind a shock originates in a region of cool gas (≈ 500 K) and this would be too cold to produce the large column densities observed for the highly excited states (Hollenbach and McKee 1989).

4.5.3.2 Magnetic precursor to a J-shock

In a magnetised medium, a magnetic precursor can form and travel ahead of the J-shock front acting as an incomplete C-shock section, gradually raising the temperature of the neutrals by collisional slippage of ions, before the J-shock front arrival (Draine and McKee 1993). Shock models including magnetic precursors have been proposed to explain the H_2 emission from Herbig-Haro objects (Carr 1993; Hartigan et al. 1989) and from supernovae remnants (Graham et al. 1991). To fit the observations these models require densities of order 100 cm^{-3} that seem too low for the low-vibrational and rotational lines to be in thermodynamic equilibrium. In a low density medium, the high excitation lines of H_2 would be so poorly populated that we should not see any emission, as opposed to the observed enhanced flux. For higher pre-shock densities of order $\approx 10^6$ cm^{-3}, the presence of a magnetic precursor ahead of the J-front will not significantly affect the dynamics of the shock because multiple collisions between the ions and the numerous neutrals will set to dominate and damp the precursor wave (Draine and McKee 1993). Thus, we conclude that the H_2 emission from HH 7 seems unlikely to arise from a magnetic precursor. However, a complete physical description of the properties of a magnetic precursor is still required and only further work on precursors will help to clarify this situation.

4.6. Conclusions

We have investigated the H_2 emission properties from Herbig-Haro 7 by measuring several spectral lines arising in the K band. These H_2 lines cover a wide range in energy of the upper level (6000–25000 K) and enables a detailed study of the temperature distribution of the gas. The calculated column density ratios have been compared to J and C–shock models for different shock geometries. We have shown that current oblique J- and C-shock models fail to explain the observed H_2 column density ratios. J-shock models fail to provide sufficient hot gas from behind the shock front and are not able to explain the large line intensities observed in the high-vibrational H_2 lines. The line emission from the 6 positions observed within the bow are shown to be consistent with a paraboloidal bow shock geometry, which however necessitates an extra source of excitation of the high energy levels to explain the H_2 line ratios. We present a study of the effects of the UV radiation field associated with the bow shock structure and show that a shock-induced Far-UV radiation field with a strength of $G_0 = 10^2$–10^3, can account for the observed H_2 line ratios. We demonstrate that shocks can be responsible for the low-lying level excitation of the H_2 molecule while Lyα resonance pumping is responsible for the high-excitation line emission. An ortho to para ratio of 1.8 appears to be consistent with the H_2 fluorescenct emission from HH 7.

A paper based on this work is being prepared for publication in the astronomical journal Monthly Notices of the Royal Astronomical Society.

Chapter 5

Molecular hydrogen spectroscopy in DR21

Summary :

Infrared emission lines of H_2 measured in the K window from the DR21 bipolar outflow show evidence for different excitation conditions in the east and west lobes of shock excited H_2. The higher H_2 line ratios measured for the east lobe suggests that the central FUV radiation field is exciting the fluorescent H_2 emission with larger efficiency than in the west lobe. Since the east lobe is closer to the central HII region, this correlates well with the lower level of fluorescence predicted for the west lobe. We show that the H_2 emission can be explained by a C-shock plus fluorescence model, where the low excitation H_2 emission is produced by shock excitation and the high excitation emission is produced by a FUV field that can be either shock-produced or ambient.

5.1 Introduction

The close association of high-velocity molecular gas with regions of active star formation in molecular clouds has stimulated numerous studies of the physical properties of shock waves and the physical conditions in star forming regions. One of the best probes of molecular cloud dynamics in these star-forming regions is vibrationaly excited H_2 emission which arises predominantly from the hot shocked gas that is produced when stellar winds collide with the surrounding cloud medium. The best studied example of such a region, the Orion Molecular Cloud star forming region (Beckwith et al. 1978; Brand et al. 1988; Draine and Roberge 1982; Geballe and Garden 1990) has defied simple understanding of its energetic activity. The gas dynamics and excitation processes in these regions are poorly understood, partially because of the lack of comparable data on other active star-forming regions. Although the DR21/HII region star forming complex has not been studied in so much detail as Orion, it is an ideal source for its spatial extent (Garden et al. 1990, ≈ 5 arcminutes), high luminosity, $L = 1.5 \times 10^5 L_o$ (Harvey et al. 1977) and high velocity winds (Garden et al. 1986; Garden et al. 1991b; Jaffe et al. 1989). This region was first discovered in a 5 GHz survey of the Cygnus X region (Downes and Rinehart 1966) and comprises several compact HII regions and near infrared sources (Wynn-Williams et al. 1974). These appear to be the source driving two highly collimated outflows which are oriented in opposite directions and extend over 2 arcminutes to each side of the central region (Fig. 5.1). Evidence for shock excitation of the molecular gas in the DR21 bipolar outflow was provided by the detection of strong emission at 2 μm from H_2 at temperatures of ≈ 2000 K and densities $n \geq 10^5$ cm^{-3} (Fischer et al. 1980; Fischer et al. 1985), consistent with post-shock cooling. At a distance of ≈ 300 pc (Campbell et al. 1982), the H_2 emission extends to about 5 pc from the central DR21 HII region/molecular cloud core which is completely obscured at optical wavelengths by about 100 magnitudes (Harvey et al. 1986). Recent observations of the 1-0 S(1) and 1-0 Q(3) lines of H_2 (Nadeau et al. 1991), suggest that the extinction is uniform across both emission lobes and that the observed morphology of the H_2 emission (Fig. 5.1) reflects the actual columns of excited gas and is not caused by increased extinction toward the DR21 central region. Thus, the lack of H_2 emission between the edge of the ionisation front and the peak of H_2 emission in the east lobe suggests that, either the DR21 outflow impacts the molecular cloud at a great distance from its source after passing through a low-density medium or that the H_2 is completely dissociated there due to the large shock velocities ($V_s \geq 300$ km s^{-1}). H_2 line profiles measured at several peak positions in both lobes show a significant difference in both shape and width (Garden et al. 1986). The velocities of peak line emission in the east lobe are on average blueshifted by 3-5 km s^{-1} relative to the DR21 rest velocity of ≈ –2.5 km s^{-1} whereas the west lobe velocities are blueshifted by ≈ 10 km s^{-1} relative to the east lobe (Garden et al. 1991a); this shows that the DR21 outflow is not bipolar in velocity. This asymmetry is also observed in the FWHM of the 1-0 S(1) line profiles, which appear to indicate higher velocities ($v > 60$ km s^{-1}) for the west lobe compared with $v < 35$ km s^{-1} for the east lobe (Garden et al. 1991a).

It has been suggested that photodissociation may be an important exciting mechanism for the molecular hydrogen lines observed (Jaffe et al. 1989). The UV radiation field from the early-type stars in the central HII region can cause the nearby molecular cloud surfaces to show intense emission from molecular and ionised species such as CO, H_2, [OI] (63 μm), [CII] (158 μm) and [SiII] (35 μm) (Burton 1992). However, the broad velocity profiles observed at certain positions within the flow suggest the presence of shocks and so it is not clear how significant is the contribution from the central PDRs to the observed H_2 spectrum. The CO J=7-6 line map of Jaffe et al. (1989) shows broad emission that correlates well with the H_2 emission (Garden et al. 1991a) and yet, it peaks in the direction of the HII region and compact far-IR continuum source rather than getting weaker (see Fig. 4 of Jaffe et al.), as is observed in H_2. Although absorption by foreground dust to the central core may be responsible for the difference in appearance of the broad-line CO 7-6 and the 2.12 μm H_2 v=1-0 S(1) distributions in DR21, the necessary dust optical depth of ≈ 5 at 2.2 μm seems too excessive (see section 5.3.1). Nevertheless, Jaffe et al. argues for the existence of a cooler quiescent gas component in front of the DR21 core that would explain simultaneously the CO 7-6 narrow-line central absorption (Fig. 6; Jaffe et al.) and the non-coincidence of the CO and H_2 emission peaks. The spatial correlation between CII, warm CO and CI in M17, suggests that the CO 7-6 emission traces the molecular cloud interfaces (PDR) that are exposed to UV ionising radiation from the central sources (Stutzki et al. 1988). This led us to investigate how much energy input into the outflow is due to shocks and how much is due to UV excitation from PDRs, for which we have measured several H_2 emission lines in the K band, arising from a range of energy levels. Since in dense PDRs the lower H_2 levels will be thermalised (Burton et al. 1988; Sternberg 1988), a clear discrimination of the emission from shocks is not possible based only on the lower vibrational and rotational lines. However, a distinction can be made in a multi-line study of the H_2 population in which the highly excited lines of H_2 (with $v \geq 3$) will be predominantly excited by the PDR.

5.2 Observations

The H_2 line observations were made during 1992 September 17-18 at the 3.8 meter UKIRT telescope on Mauna Kea. The long slit capability of the cooled grating spectrometer CGS4 was used to measure K band H_2 emission lines from the DR21 cloud, whose H_2 1-0 S(1) emission arises from two directly opposite lobes (Garden et al. 1986). The $1.5'' \times 90''$ slit was oriented parallel to the major axis of the H_2 emission on each lobe according to the 1-0 S(1) emission map of Garden et al. (1991a). This yielded a slit position angle of 59 degrees for the east lobe and 45 degrees for the west lobe (Fig. 5.1). In these positions the slit aperture intersects several peaks (clumps) of H_2 emission that are shown in the 2″ resolution map presented by Garden et al. (1990). The nominal middle slit positions chosen for both lobes are shown in Table 5.1. The complete K window spectrum of H_2 was measured in two grating positions (K1: 2.01-2.24 μm and K2: 2.21-2.44 μm) due to the medium spectral resolving power employed of $\approx$ 710 at 2.2 μm. Since at this resolving power the lines are unresolved, their line fluxes were measured by fitting the instrumental triangular profile. Standard sky nodding (300″ North-South) and frequent checks of the nominal position on source (peak-ups) were employed. Absolute pointing was performed by using the movie technique, which consists in taking a nearby sky frame and subtracting from a source frame movie at a rate of 1 frame per second. During this movie, the slit position on-source is adjusted by a fraction of an arcsecond so to maximise the intensity measured. This technique is believed to provide a pointing accuracy better than 1″. Line flux calibration was based on measurements of the continuum flux density of the standards BS 7847 (R.A.= $20^h 30^m 59.1^s$, Decl.= +36° 56′ 9″; J2000.0) and BS 15 (R.A.= $0^h 8^m 23.2^s$, Decl.= +29° 5′ 26″; B1950.0), whose K magnitudes were taken to be 3.51 and 2.37, respectively. The Brγ absorption feature present in the spectrum of the standards was artificially removed by fitting the instrumental profile to this line and then subtracting it off from the spectrum. Wavelength calibration was determined by measuring the emission lines of an arc lamp. The observations log for DR21 is presented in Table 5.1. The final spectrum was coadded over 40 detector rows for both slit positions to increase the signal-to-noise in the H_2 emission lines. The high signal to noise achieved in these lines can be seen in Fig. 5.2, which presents the coadded spectra for the east lobe; the west lobe has similar signal to noise. Some residual sky emission was found on the final reduced frames and arises as a result of inaccurate sky subtraction, probably due to the poor weather conditions. Some of these sky emission lines appeared blended with H_2 lines at the positions labelled in Fig. 5.2. We have estimated the sky line strength from an adjacent sky pixel position and subtracted from the blend to recover the line flux from the H_2 line alone. The measured fluxes for all H_2 lines are given in Table 5.2.

The standard stars used for flux calibration and ratioing out the atmospheric absorption, were observed through clouds in some frames, causing the measured flux to fluctuate over the observation period. This has affected the measurements of DR21 west lobe in the K1 grating position. The 1-0 S(1) flux observed by Garden et al. (1991) in a 10″ circular aperture centred on a bright H_2 emission peak is $\approx 2 \times 10^{-4}$ erg s^{-1} cm^{-2} sr^{-1} for the east lobe and compares well with the flux of 5.6×10^{-4} erg s^{-1} cm^{-2} sr^{-1} which we have measured in a 1.5″ × 60″ aperture and which covers most of that H_2 emission peak. However, the 1-0 S(1) flux observed in the west lobe was down by a factor of ≈ 90 from the value in Garden et al. (1991). Comparing the 1-0 S(0) line flux from both grating positions in DR21 west it was found that they differ by a factor of ≈ 86. Since the measurements on the K1 grating position are consistent with the result obtained by Garden et al. (1991) for the 1-0 S(1) line, we concluded that the measurements in DR21 west K2 had been overestimated. The solution to this problem came from inspection of Table 5.1, which shows that this grating position (K2) used a different standard for calibration. By inspecting the flux in both standards at 2.25 μm, we found a discrepancy of about 90 between the number of counts. This appears to explain the flux loss from the DR21 data in grating position K1, since the gratings data were reduced independently. After correcting for this effect, the emission from the west lobe is typically 5 times weaker than that from the east lobe (Table 5.2) and yields a flux in the 1-0 S(1) line of 1.1×10^{-4} erg s^{-1} cm^{-2} sr^{-1}, which is a similar value to the one found by Garden et al. (1991).

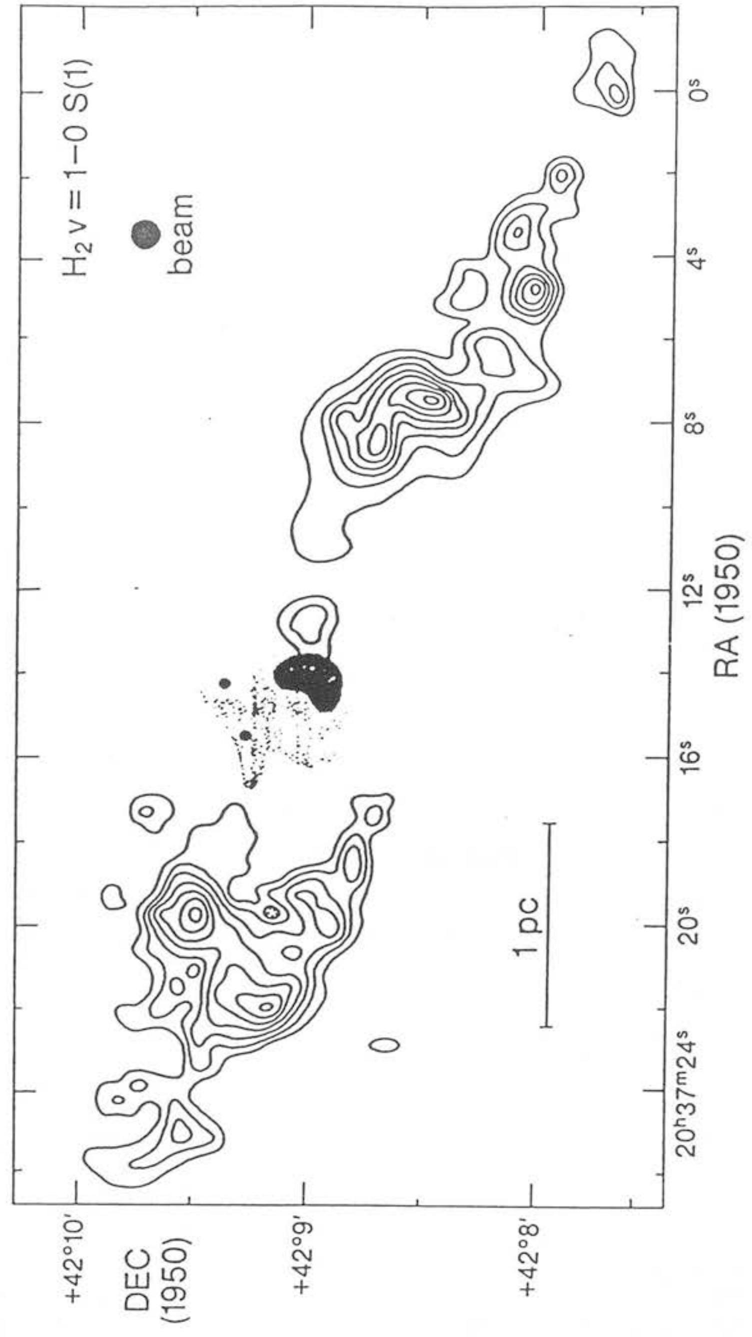

FIGURE 5.1: Contour map of the H_2 v=1-0 S(1) line intensity in the DR21 outflow as measured on a 3″ square grid of positions using a 100 km s^{-1} resolution Fabry-Perot interferometer and a 5″ beam. The shaded area corresponds to the DR21 compact HII region as revealed by the 6 cm radio continuum emission (Garden et al. 1991a).

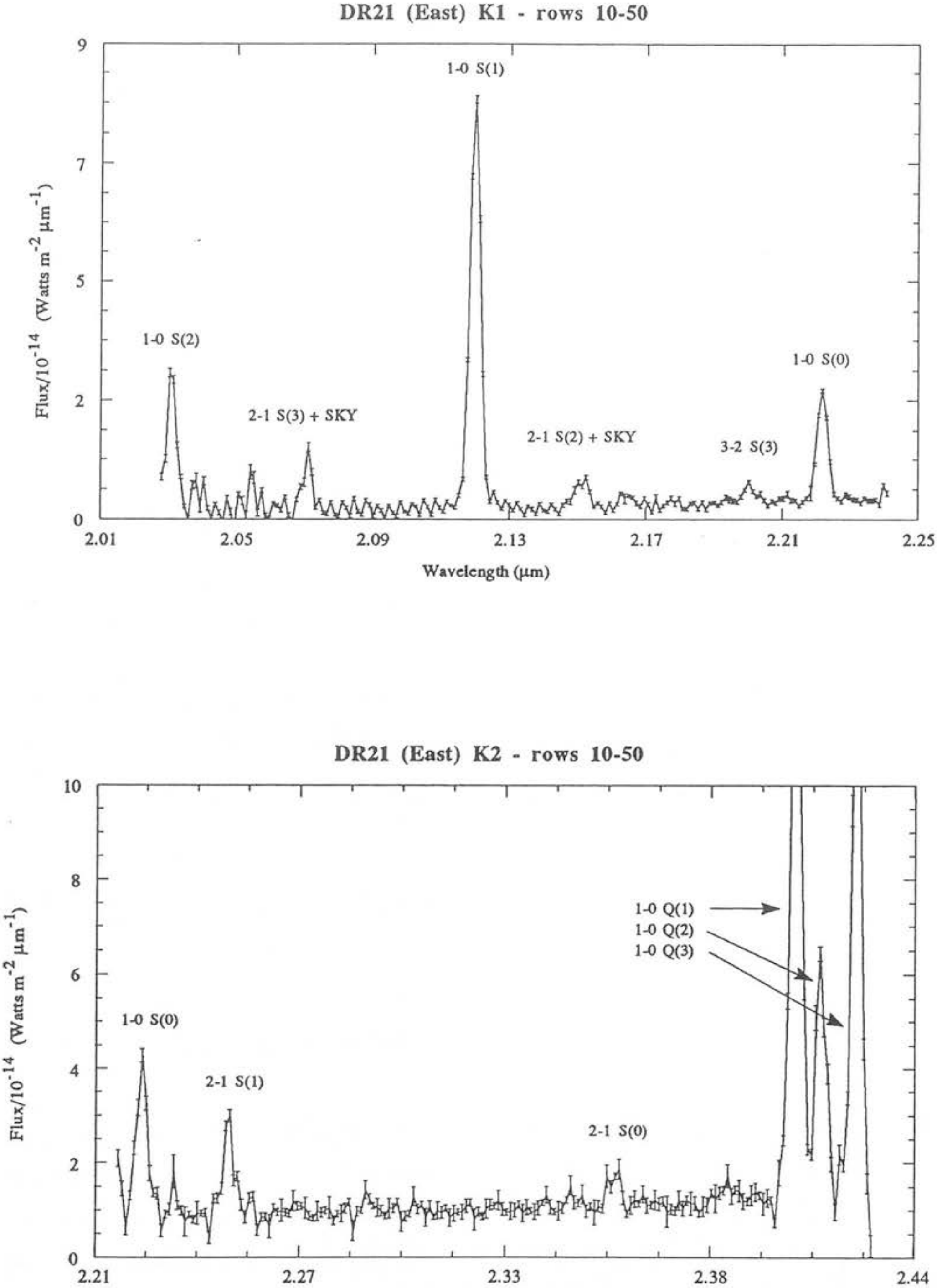

DR21 (East) K1 - rows 10-50

DR21 (East) K2 - rows 10-50

FIGURE 5.2: Observed K-band spectra at the East lobe of DR21.

TABLE 5.1: Observations log of DR21

Position/Date	Co-ordinates (middle of slit)	Grating position[a]	Standard star	m_K[b]
DR 21 West	R.A.= $20^h\,37^m\,7.4^s$	K1	BS 7847	3.51
Date: 17/9/92	Decl.= +42° 8' 29"			
	(1950.0)	K2	BS 15	2.37
DR 21 East	R.A.= $20^h\,37^m\,22^s$	K1	BS 7847	3.51
Date: 18/9/92	Decl.= +42° 9' 10"			
		K2	BS 7847	3.51

Notes: [a] The grating positions are K1: 2.01-2.24 μm and K2: 2.21-2.44 μm.

[b] This is the K (2.2 μm) magnitude of the standard star given in Lang (1992).

5.3 Results and Discussion

5.3.1 Measurement of the extinction

The reddening to the source can be determined from our data by comparing the fluxes of the 1-0 S(1) and 1-0 Q(3) lines of H_2 because since their line ratio is independent of the excitation process, it provides a direct measure of the foreground dust extinction. Then, in a manner similar to the calculation in chapter 4, the extinction at any other wavelength is determined from the assumed extinction law $A_\lambda = k\,\lambda^{-\alpha}$, where $\alpha = 1.7$. In these calculations, the energy levels are taken from Dabrowski (1984), the Einstein A-values are from Turner, Kirby-Docken & Dalgarno (1977) and the ortho-to-para ratio is assumed to be 3. We estimate that $A_K = 1.9 \pm 0.3$ in the east emission lobe and $A_K = 2.3 \pm 1.0$ in the west emission lobe. In a recent work, Nadeau et al. (1991) have obtained measurements of these two lines at several positions in DR21 and conclude that the extinction plays little role in the near-infrared appearance of the region. The general uniformity of the extinction across the source was taken to indicate that the gap in emission seen in the 1-0 S(1) infrared maps (e.g. Garden et al. 1990) is real and suggested that both outflows move through a low-density medium before impacting the surrounding molecular cloud. Their average extinction value of 25 ± 6 visual magnitudes ($A_K = 2.5 \pm 0.6$), derived for $\alpha = 1.8$, is in good agreement with our measurements at both outflow lobes. Garden et al. (1986) report extinction values of 3.4 ± 1.0 and 3.3 ± 1.0 for the east and west lobes of H_2 emission, respectively, obtained for $\alpha = 1.85$. The higher extinction uncertainty obtained for the west lobe in the present work is probably due to the lower signal to noise obtained on the lines, as they are 5 times weaker than in the east lobe. In addition, an extra source of error in 1-0 S(1) / 1-0 Q(3) line ratio probably might be introduced in the process of scaling the flux from the K2 grating position (1-0 Q(3)) to the K1 grating position (1-0 S(1)).

5.3.2 Excitation mechanisms for the H_2 emission

Table 5.2 presents the H_2 line intensities and respective column densities measured in both emission lobes in DR21. These data are plotted in Fig. 5.3 in a normalised column density ratio diagram. The advantage of using such a diagnostic diagram is that the H_2 line ratios can be directly compared with a thermalised slab of gas at T = 2000 K, having the same column density on the $v = 3$, $J = 1$ upper level. It is perhaps not surprising that the line ratios from the east and west lobes appear significantly different, since the asymmetry of the excitation in the lobes has already been established (Garden et al. 1991a). In particular, the emission from the east lobe appears to arise from a hotter gas component, since the vibrational excitation temperature derived from the 1-0 S(1) / 2-1 S(1) ratio, being proportional to the slope defined by the 1-0 S(1) and 2-1 S(1) data points in this diagram, is of order 3000 K whereas the flatter slope for the west lobe implies an excitation temperature of ≈ 2000 K. Furthermore, the line ratios measured in the east lobe are higher than those for the west lobe, for all the observed H_2 lines. This presents strong evidence for different excitation conditions in both emission lobes. This difference raises questions about the physical conditions in both lobes, the nature of the shocks exciting the emission and the role of UV excitation.

TABLE 5.2: Line intensities and column densities for the H_2 emission in DR 21

				DR21 WEST		DR21 EAST	
Transition	λ^a (μm)	Energy^b (Kelvin)	g_j^c	Line flux^d (10^{-6} erg s^{-1} cm^{-2} sr^{-1})	Nj / gj (10^{13} cm^{-2})	Line flux^d 10^{-6} erg s^{-1} cm^{-2} sr^{-1}	Nj / gj (10^{13} cm^{-2})
K2 grating...........							
1-0 S(0)	2.2235	6471	5	24.2 ± 0.85	26.9 ± 0.9	132 ± 9.9	147 ± 11
2-1 S(1)	2.2477	12550	21	9.02 ± 0.27	1.23 ± 0.03	89.7 ± 6.1	12.2 ± 0.8
3-2 S(2)	2.2870	18386	9	0.94 ± 0.16	0.27 ± 0.04	12.6 ± 3.6	3.60 ± 1.02
4-3 S(3)	2.3445	23956	33	0.49 ± 0.17	0.05 ± 0.02	10.9 ± 4.5	1.07 ± 0.44
2-1 S(0)	2.3556	12095	5	2.66 ± 0.24	2.15 ± 0.20	33.5 ± 4.7	27.2 ± 3.8
3-2 S(1)	2.3864	17818	21	1.76 ± 0.19	0.25 ± 0.03	12.8 ± 3.9	1.80 ± 0.54
1-0 Q(1)^e	2.4066	6149	9	94.0 ± 2.3	37.1 ± 0.9	517 ± 8	204 ± 3
1-0 Q(2)^e	2.4134	6471	5	34.2 ± 2.3	34.4 ± 2.3	194 ± 6	196 ± 6
1-0 Q(3)^e	2.4237	6956	21	85.7 ± 2.3	22.5 ± 0.6	431 ± 9	113 ± 2
K1 grating...........							
1-0 S(1)	2.1218	6956	21	111 ± 8	20.4 ± 1.5	555 ± 3	102 ± 0.6
2-1 S(3)	2.0735	13890	33	8.04 ± 0.60	0.55 ± 0.04	74.9 ± 3.8	5.16 ± 0.27
1-0 S(2)^e	2.0338	7584	9	34.8 ± 2.5	12.5 ± 0.9	200 ± 5	71.7 ± 1.8
2-1 S(2)	2.1542	13150	9	2.92 ± 0.27	0.79 ± 0.07	40.6 ± 2.6	11.0 ± 0.7
3-2 S(3)	2.2014	19086	33	2.27 ± 0.22	0.17 ± 0.02	21.1 ± 1.7	1.58 ± 0.13
1-0 S(0)	2.2235	6471	5	24.2 ± 1.9	26.9 ± 2.2	132 ± 3	147 ± 3

Notes:

a) Line center wavelengths in vacuum; taken from (Dabrowski 1984).

b) Upper level energy of the transition in units of temperature; $E_j = kT_j$.

c) Statistical weight for the upper level of the transition assuming an ortho/para ratio of 3.

d) Line intensities corrected for extinction. The associated 1σ error is derived from the line fitting process.

e) These lines lie at the edges of the K window, where atmospheric absorption is significant and thus the quoted fluxes are lower limits. In addition, the Q-branch lines are partially blended in the spectrum (see Fig. 5.2) which makes these lines unreliable for the H_2 line ratio analysis presented in section 5.3.

In the DR21 region, where both high-velocity flows and large UV photon fluxes (originating from the central expanding HII regions) are present, a determination of the relative contributions of shock excited and fluorescent H_2 emission is essential for a detailed analysis of the dynamics and energetics resulting from the interaction with the ambient molecular cloud. Previous observations of this source (Garden et al. 1986) have used the 1-0 S(1) / 2-1 S(1) intensity line ratio to deduce that collisional excitation by shocks was responsible for the observed H_2 emission. This conclusion followed from the fact that the observed 1-0 S(1)/2-1 S(1) peak values of 9 and 13 for the east and west lobes, respectively, were close to the theoretical ratio of ≈ 10 for shocks (Shull and Draine 1987) and significantly different from 1.8, the value predicted for radiatively excited H_2 emission (Black and Dalgarno 1976). These values compare well with the present calculations for the east and west positions of approximately 5 (8 dereddened) and 10 (16 dereddened), respectively. However, these conclusions are based on a single line ratio which, as will be discussed below, is a poor diagnostic in regions close to a FUV field.

We have used two basic shock models, (J)ump and (C)ontinuous, to attempt to explain the emission from both lobes. These are distinguishable by the importance of the ambient magnetic field (Draine 1980). The physical properties and model predictions for the H_2 line emission of these two types of shocks have been outlined in Chapter 2. C-shocks are magneto hydrodynamic structures where the neutral gas is accelerated and heated by the ambipolar diffusion of trace ions through the neutrals (Draine and McKee 1993). In these shocks, both the neutrals and the ion-electron flow variables are continuous throughout the shock structure rather than undergoing a compression jump (J-shock). Thus, C-shocks are essentially of non-dissociative nature ($V_s \leq$ 40-50 km s^{-1}), which implies that the maximum post-shock temperatures are constrained to be ≤ 4000 K (Smith et al. 1991a), far below the temperatures which result from dissociative J-shocks. C-shocks cool primarily through [OI] fine-structure lines (63 and 145 μm) for $V_s \leq 12$ km s^{-1} and through H_2 vibrational-rotational and H_2O rotational lines for $12 \leq V_s \leq 50$ km s^{-1} (Draine et al. 1983).

On the other hand, J-shocks can form in a relatively highly ionised gas causing the gas to attain post-shock temperatures $\geq 10^4$ K and causing the complete or partial dissociation of molecules and the ionisation of atoms (Hollenbach and

Shull 1977). Dissociative J-shocks generally radiate via atomic and ionic permitted and forbidden lines in the UV and optical wavelengths, but also emit significant intensities in the far-infrared fine-structure lines, and in particular the 63 μm [OI] transition. Slow (partially dissociative) J-shocks, produce strong H_2 and [OI] (63 μm) emission, but since they cause negligible gas ionisation, they produce little [CII] (158 μm) and [SiII] (35 μm). To reproduce the [OI], H_2, CO and OH line intensities observed toward Orion, a two-shock model combining C-shocks and dissociative J-shocks has been proposed (Chernoff et al. 1982; McKee and Hollenbach 1987). Non-dissociative J-shocks, with $8 \leq V_s \leq 20$ km s^{-1}, have been shown to provide a better fit to the H_2 line emission in the BN-KL region of Orion (Brand et al. 1988; Brand et al. 1989b), although it is difficult to reconciliate the low velocities implied for the gas with the observed broad (FWHM $\approx$ 60 km s^{-1}) H_2 line profiles (Garden et al. 1991a).

In Fig. 5.4 it is plotted the column density ratios for the east and west lobes together with selected C-shock and J-shock models. Clearly, neither model provides an acceptable fit to the data. As already discussed in Chapter 4, a J-shock model cannot provide sufficient curvature in the high-excitation lines to explain simultaneously all the H_2 line ratios while a single C-shock predicts a common origin for the line emission (near the peak temperature), and produces a nearly flat curve in the column density diagrams of Fig. 5.4. In addition, no shock model can account for the observed scatter amongst the data points in each particular vibrational level. In general, no single — or combination of any type of — shock will be able to generate such scatter. We have seen in chapter 4 that H_2 fluorescence can generate such scatter in these diagrams if the ortho to para abundance ratio is 1.8. Thus, if the origin of the scatter can be attributed to H_2 fluorescence then, this indicates that the UV excitation is preferentially pumping the high energy levels of H_2. Examination of Table 5.3, which shows the fraction of fluorescence and shocked emission that contributes to any H_2 line, confirms so. Hence, it seems that both shocks and fluorescence are competing mechanisms for the excitation of H_2 emission in DR21. This two-component model consisting of a shocked component and a fluorescent component is analysed next.

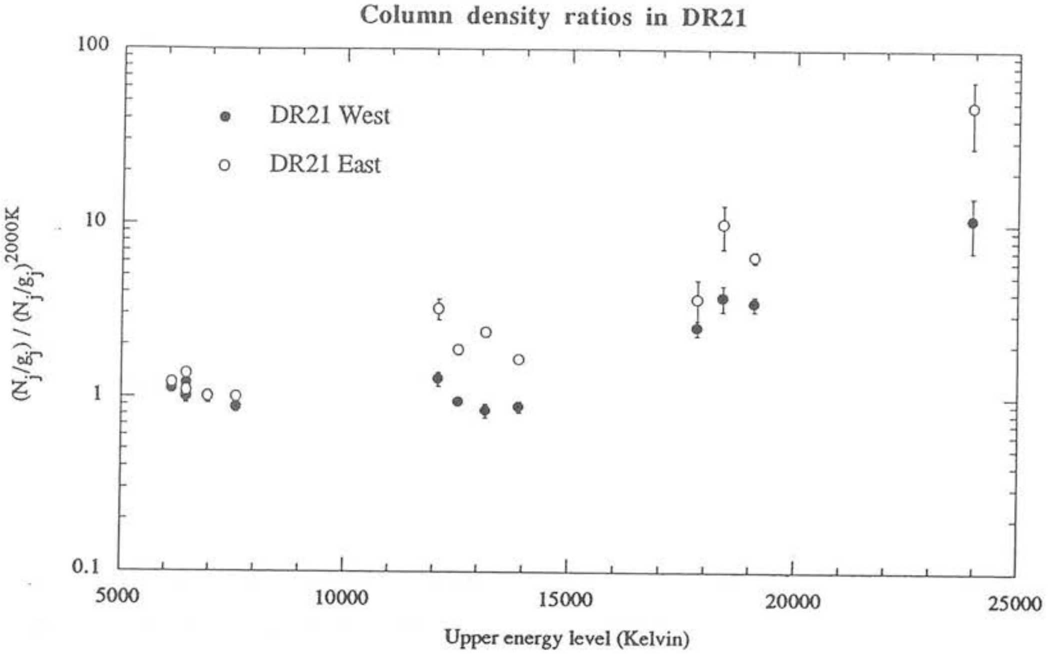

FIGURE 5.3: Column density ratio (CDR) diagrams for both lobes in DR21.

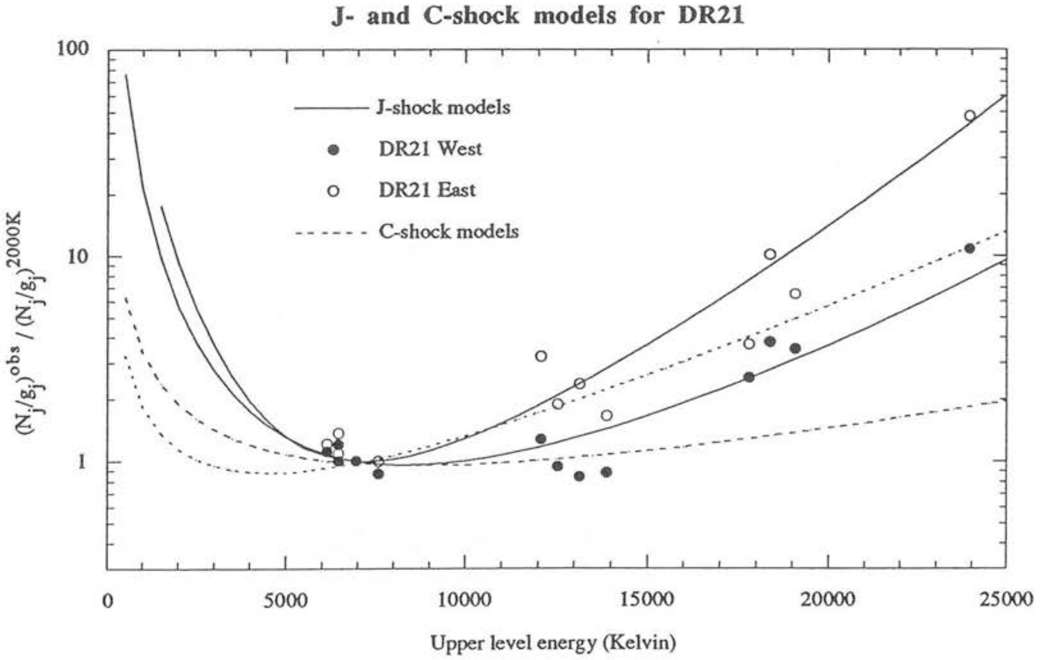

FIGURE 5.4: J- and C-shock model fits to DR21 east and west lobes.

5.3.3 A combined model for the H_2 emission in DR21

The dashed line in Figure 5.5 shows the prediction for the H_2 line ratios of the a single C-shock for the west lobe (upper diagram) and the east lobe (lower diagram). The C-shock curve model was calculated from the analytic approximation given in Smith (1989) for the planar C-shock, but modified to account for oblique shock fronts (Smith et al. 1991a). As demonstrated in Fig. 9 of Smith (1991a), the slope of the shock model curve for $T_j \geq 7000$ K, is a function of the maximum temperature attained in the post-shock layer, which in turn is a function of the shock front obliquity for a given shock speed. Other parameters less sensitive to the H_2 line ratios, were taken from the standard set given in Smith (1991a): pre-shock density $n_0 = 10^6$ cm^{-3}, magnetic field strength $B = 10^{-3}$ G, ionisation fraction $\chi_0 = 10^{-7}$ and H_2O abundance of 4.25×10^{-4}. The crosses in Fig. 5.5 show the predictions for a model where the excitation of H_2 is simultaneous from an oblique C-shock and from an ambient UV field. The predictions for the fluorescent line ratios were taken from Black and van Dishoeck (1987, hereafter BvD) model #14, which has parameters: $n = 3 \times 10^3$ cm^{-3}, $T = 100$ K and $I_{UV} = 10^3$ (FUV intensity in the 912-1130 Å range is $\approx 4.76 \times 10^{-5}\, I_{UV}$ erg s^{-1} cm^{-2} sr^{-1}). This combined model is essentially parametrised by the obliquity of the C-shock front (which gives the maximum temperature) and the combination factors for the shocked and fluorescence column densities: $N_{total} = f_1\, N_{C\text{-shock}} + f_2 N_{fluorescence}$. The predicted relative populations for the shocked and fluorescent components are presented in Table 5.3. As expected, the fluorescent contribution for the $v = 3$, $J = 3$ energy level is small for the 1-0 S(1) line (10%, East; 4%, West) compared with the shocked contribution (90%, East; 96%, West). The 1-0 S(1) line intensity due to fluorescence is predicted to be $\approx 4.1 \times 10^{-6}$ erg s^{-1} cm^{-2} sr^{-1} and $\approx 9.2 \times 10^{-5}$ erg s^{-1} cm^{-2} sr^{-1} in the west and east lobes, respectively. Yet, fluorescent H_2 dominates the excitation in the high energy levels, as can be seen for example in the 4-3 S(3) line (86%, East; 63%, West). Intermediate combination values are found for intermediate energy levels. Other detailed models of fluorescence H_2 line emission from clouds have been presented by Burton, Hollenbach and Tielens (1990, BHT) and Sternberg and Dalgarno (1989, SD). The main difference between these models is the different regimes of parameter space: $10^3 \leq n \leq 10^7$ cm^{-3} and FUV fields, $10^3 \leq G_0 \leq 10^5$ times the ambient interstellar value (BHT, SD), and densities $n \leq 10^4$ cm^{-3} with $G_0 \leq 10^3$ (BvD). Also, these models employ different descriptions for the chemistry and the energy balance through the PDR. Only models with $10^2 \leq G_0 \leq 10^3$ for densities $n \approx 3 \times 10^3$ cm^{-3}

(BvD) or n ≈ 10^6 cm^{-3} (BHT), can provide an overall good fit to the data (see Figs. 5.5 and 5.6). The best fit for the BHT model has parameters n = 10^6 cm^{-3} and G_0 = 10^3 and is displayed in Fig. 5.7 for the east and west lobes. Both BvD and BHT models have clearly different predictions for the fluorescent H_2 line ratios. It was discussed in chapter 4 that the reason was the assumed ortho to para ratio, 1.8 for the BvD model and 3 for the BHT model. So, it appears that in DR21 this ratio is 1.8 for the fluorescent component, since the BvD model provides a better fit to the scatter.

The best fit C-shock model yields a maximum temperature of ≈ 2700 K for the East lobe and ≈ 2000 K for the west lobe. These correspond to shock front obliquities of ≈ 47° and 58°, respectively (for V_s = 120 km s^{-1}). Smaller front obliquity angles can be attained by reducing V_s, so to get the same peak temperatures. It is clear from Table 5.3 that there is a higher contribution of fluorescent emission in the east lobe. As discussed by Garden et al. (1986) the East lobe is situated in the immediate vicinity of the expanding central HII region which may produce an enhanced UV field. In the absence of an exciting UV continuum, another possibility for producing the H_2 fluorescent emission is that of Lyα resonance pump of the excited levels of H_2 (Black and van Dishoeck 1987). Shock-produced FUV emission, and in particular Lyα, has been proposed to explain the excitation in Herbig-Haro 7 (chapter 4), since these objects show no continuum emission in the line of sight and the source responsible for driving the HH 7-11 flow seems to be too distant to significantly affect the gas excitation properties in HH 7. The gap in H_2 emission between the central HII region and the east lobe seems to present a problem for the excitation of H_2 in the east lobe by the central ambient field. Unless we invoke clumpiness in this medium, it is difficult to explain why the ionising UV gets absorbed so close to the source and yet the FUV travels so far (≈ 1 pc) as to excite H_2 emission in the east lobe. A more detailed study of the excitation conditions in this emission gap is required before ruling out the ambient field model. Nevertheless, there is probably sufficient contribution from shock-produced Lyα resonance pumping of the H_2 levels in DR21. Testing this hypothesis will require high spectral and spatial resolution observations of profiles of several H_2 emission lines arising from widely different upper energy levels. The width of these lines would then directly relate with the excitation mechanism, narrow for fluorescence and broad for shocks.

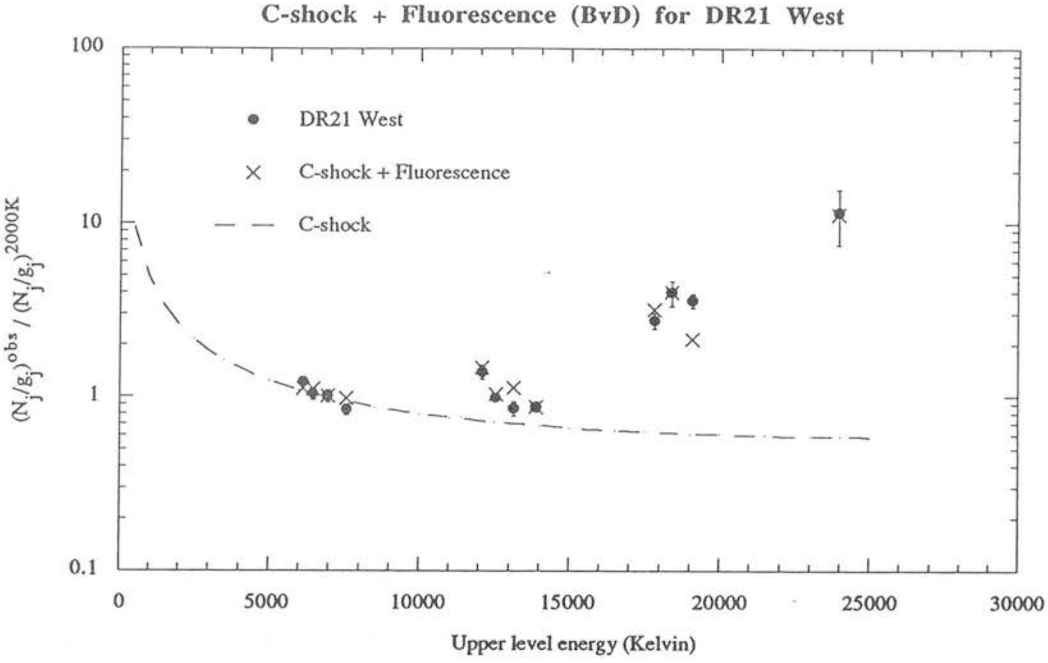

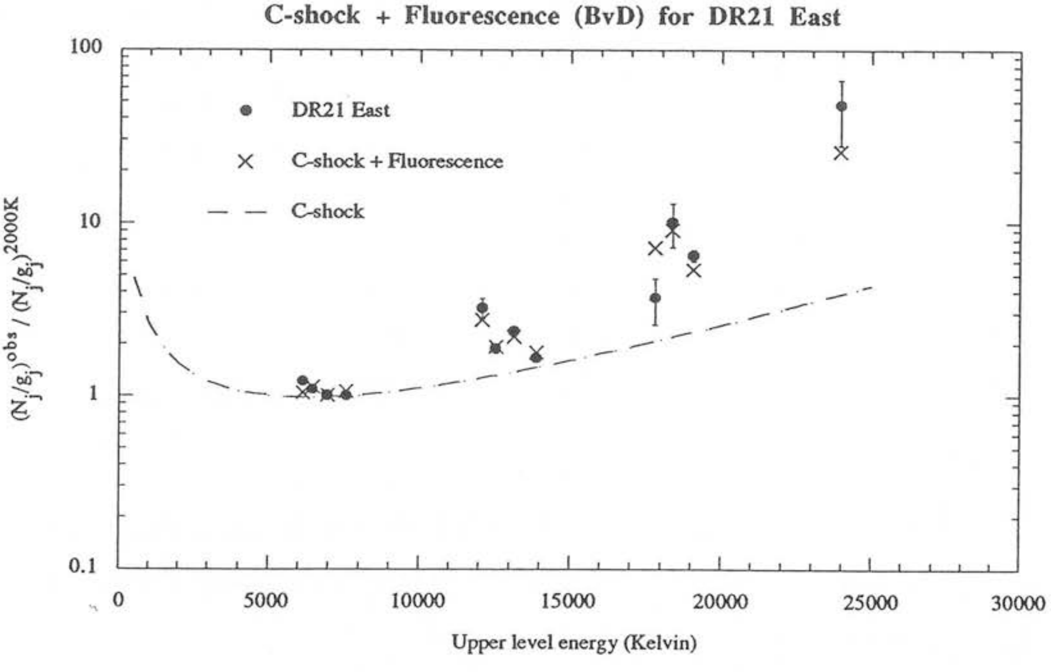

FIGURE 5.5: Combined model prediction for the east and west emission lobes. The PDR fluorescent model used in these plots is taken from (Black and van Dishoeck 1987).

Table 5.3: Shocked and fluorescent fractions for the combined model

Transition	WEST		EAST	
	N_{fl}/N_{Tot}	N_{sh}/N_{Tot}	N_{fl}/N_{Tot}	N_{sh}/N_{Tot}
K2 grating				
1-0 S(0)	7%	93%	20%	80%
2-1 S(1)	25%	75%	37%	63%
3-2 S(2)	62%	38%	78%	22%
4-3 S(3)	63%	37%	86%	14%
2-1 S(0)	43%	57%	58%	42%
3-2 S(1)	58%	42%	74%	26%
1-0 Q(1)	5%	95%	14%	86%
1-0 Q(2)	7%	93%	20%	80%
1-0 Q(3)	4%	96%	10%	90%
K1 grating				
1-0 S(1)	4%	96%	10%	90%
2-1 S(3)	16%	84%	25%	75%
1-0 S(2)	5%	95%	13%	87%
2-1 S(2)	30%	70%	43%	57%
3-2 S(3)	39%	61%	60%	40%
1-0 S(0)	7%	93%	20%	80%

Note: N_{fl}/N_{Tot} (N_{sh}/N_{Tot}) is the fractional column density of the fluorescent (shocked) component, calculated with the BvD PDR model.

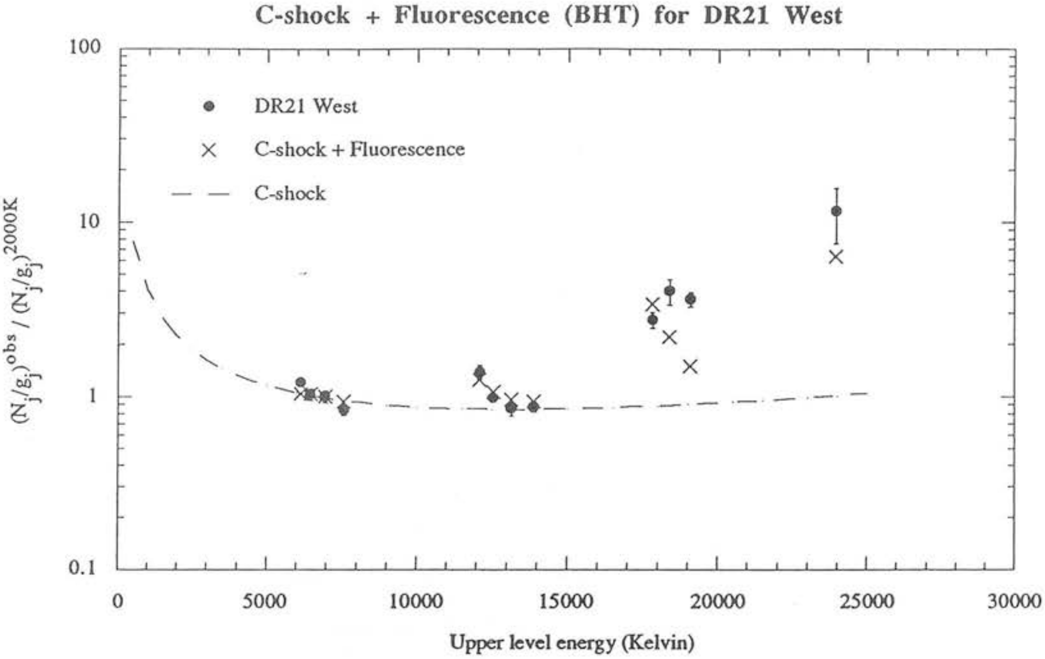

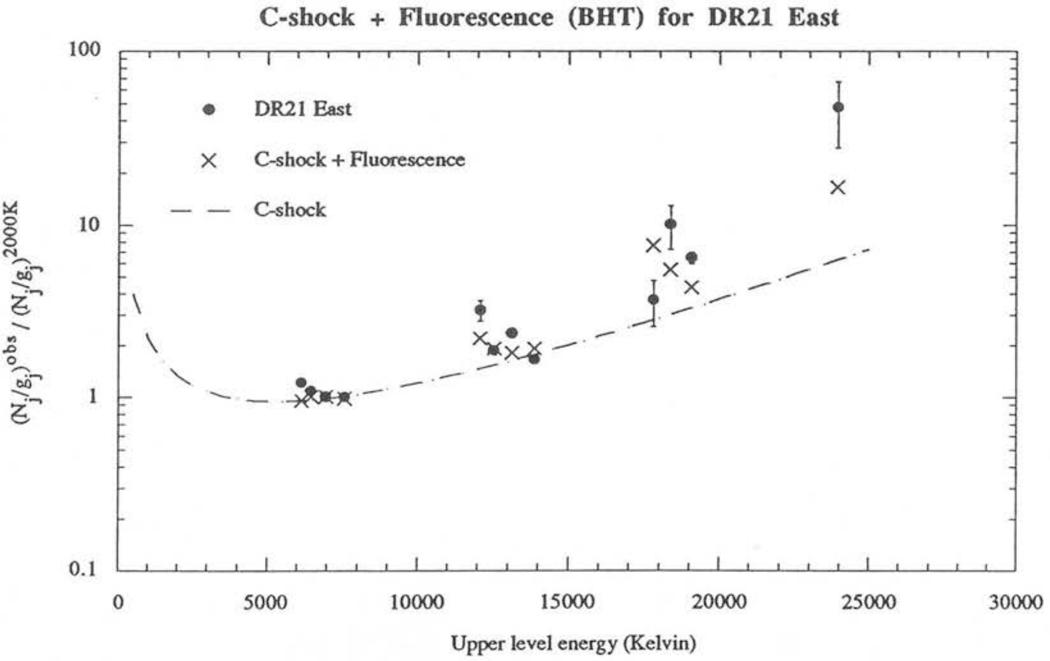

FIGURE 5.6: Similar to Fig 5.5 but for the PDR fluorescent model of Burton et al. (1990).

5.4 Conclusions

In this chapter we have presented measurements of several infrared emission lines of H_2 in the K window from the DR21 bipolar outflow, which show different excitation conditions for the east and west lobes of H_2 emission. The higher H_2 line ratios measured for the east lobe is indicative of enhanced excitation for the high-excitation levels of the H_2 molecule, which can be caused by either shock-produced Lyα resonance pumping or by direct UV excitation of H_2 from the central HII region. This is consistent with the east lobe being bordering the central HII region and producing higher fluorescent fluxes. We show that the H_2 emission can be explained in terms of a model consisting of a C-shock and a PDR. The H_2 line ratios are best fitted with a PDR model with parameters: FUV field in the range $10^2 \leq G_0 \leq 10^3$ and densities $n \geq 3 \times 10^3$ cm^{-3}. From comparison of the PDR models investigated we suggest that in DR21 the ortho to para ratio is 1.8 for the fluorescent component.

Chapter 6

Conclusions

6.1. Introduction

The work presented in this thesis is concerned with the study of shock excited molecular hydrogen in dense molecular clouds that is associated with high-velocity phenomena. The emission from this molecule provides an important diagnostic of the shock activity because of its high abundance and the fact that these lines are observable from gas at temperatures (≈ 2000 K) similar to those achieved behind a shock wave, unlike other molecules, e.g. CO that is predominantly excited in cooler gas. The spectroscopic study carried out in this work in two high luminosity galactic regions, Herbig-Haro 7 and the bipolar outflow DR21, has concentrated in the measurement of more than 10 emission lines of molecular hydrogen (H_2) in the K band (2.03–2.44 μm) that cover a wide range of upper level energies (6000–25000 K) and thus are sensitive to the excitation conditions in the gas. The H_2 emission observed from HH 7 show that the column density ratios are consistent with the emission being excited in a bow C-shock; a shock structure that has been suggested by high spectral resolution optical studies. The C-shock model used employs an analytic approximation for planar C-shocks but modified to account for the curvature of a paraboloidal bow surface. The paraboloidal bow C-shock configuration proposed for HH 7 is parametrised from two oblique C-shocks and a fluorescent component. The maximum temperatures reached in the shocks are well separated, with the near shock contributing 8% (T=4000 K) and the far shock contributing 92% (T=1900 K) to the total shocked emission. The most sensitive parameters in the model are the orientation angle of the axis of the bow relative to the line of sight (θ), the bow shock velocity and the gas cooling function. Extinction can also affect the observed appearance of the bow. We show that for the 4 positions observed within the HH 7 bow the extinction is uniform: $A_K \approx 1$. The H_2 line emission from HH 7 is well fitted to a bow shock with parameters $V_s = 140$ km s^{-1} and $\theta = 40°$.

The most important result derived from the high signal to noise line ratios obtained for both objects, is that a combination of shocks and fluorescence may be contributing together to the emission spectrum. The Far-ultraviolet (FUV) field arising from the DR21 central HII region may be affecting the excitation of all or part of the east and west outflows and causing the high excitation lines of H_2 to have a fluorescent signature. It is predicted that H_2 fluorescence dominates the spectra of the high excitation lines observed in both objects, contributing > 60% for the 4-3 S(3) line and > 40% for the 3-2 S(3) line, while the lower vibrational-rotational lines of H_2 are collisionally thermalised by shocks, contributing > 96% for the 1-0 S(1) line. The lack of a nearby continuum source in HH 7 suggests that the H_2 fluorescent emission in this object is pumped through HI Lyman-α resonance with some H_2 UV transitions. The bright Hα emission observed in this object, associated with its broad line profile, also favours this scenario. The H_2 line ratios in both objects indicate a FUV radiation field of $10^2 \leq G_0 \leq 10^3$ for densities $n \geq 10^4$ cm^{-3} using current models of radiatively excited H_2 emission. Future high spectral resolution observations of these H_2 emission lines are expected to provide further constraints to the models. In particular, they should delineate the importance of H_2 fluorescence in these and other shocked regions and provide further diagnostics to test C-shock models.

Because of the different predictions of the PDR models used, we derive that the ortho to para abundance ratio of the fluorescent H_2 population is of order 1.8 in both objects. This is in contrast to a pure shocked population which has an abundance ratio of 3. These low values have been observed in several objects, M17, Hubble 12, and NGC 2023 that are nearly pure fluorescent sources and this has strong implications for the H_2 formation mechanism in PDRs. We expect that in the near future the modelling of the ortho to para ratio from "shocked" regions will provide important diagnostics of the H_2 formation mechanism on the surfaces of dust grains.

Whilst the velocity profiles observed in HH 7 (FWHM $\approx$ 30–45 km s^{-1}) are generally consistent with the bow C-shock model, which predicts total H_2 dissociation for $V_s > 40–50$ km s^{-1}, the extremely wide profiles observed in DR21 and Orion still present a problem for C-shock models. Nor can standard J-shock models provide the observed line widths since these are limited by molecular dissociation to velocities ≤ 25 km s^{-1}. To explain these widths by J-shocks then requires very exotic mechanisms, such as pre-accelerated clumps (30-40 necessary in Orion) with velocities of up to $\approx$ 70 km s^{-1} being impacted by weak J-shocks (8–20 km s^{-1}). The dissociation limit for C-shocks can, however, be relaxed in regions of high magnetic fields such as those energised by outflows from young stars. Under such conditions ($B \geq 20$ μG), the very high Alfven velocities achieved ($v_A \geq 30$ km s^{-1}) will produce a softened shock in which the ions stream through the neutrals with only a small fraction of the shock speed. As a result, molecular hydrogen can be accelerated to very high velocities without being dissociated. Our knowledge of the field strength in dense molecular clouds is still very limited but the best available data suggests that it is of order a few μG. Verifying the predictions from highly magnetised C-shock models through its many molecular and atomic coolants is necessary to clarify this issue.

6.2. Directions and prospects for future research

Recent technological advances in infrared detector designs have provided the astronomical community with highly sensitive and reliable infrared array detectors whose efficiency has substantially increased over the past few years and now provides a comprehensive facility for both high spectral (10 km s^{-1}) and spatial (1″) resolutions. The latest spectrometer to use such technology is the new cooled grating spectrometer CGS4, designed and built at the Royal Observatory in Edinburgh and now operates on the 3.8 meter United Kingdom Infrared Telescope (UKIRT) in Hawaii. The present detector on CGS4 with a current format of 58 × 62 pixels is expected to be upgraded to a 256 × 256 device by the end of 1994. All these improvements will help to produce high quality data on more sources and allow the determination of more accurate line intensities and ratios that are an essential for comparison with the models. Furthermore, observations of the more interesting and faint lines will be possible with the higher sensitivity arrays in the near future, and this will help to establish the nature of the shocks exciting the infrared H_2 emission and the importance of UV-excited H_2 emission in molecular outflows near regions of recent star formation. Of much interest also, will be the determination of the infrared extinction curve with high accuracy to deredden the extinguished line fluxes, since with the high signal to noise now offered by the new generation of cooled grating spectrometers available, it is vital to calculate the line ratios with similar accuracy. All these observations will prove crucial for developing current shock models and will help to constrain the model's parameter space.

Up to now, most of the work on the infrared emission from H_2 has been done by observing in the windows that are free from strong telluric absorption. A new generation of telescopes for optical and infrared studies is being built for both ground based and satellite observatories. For example, the Infrared Space Observatory (ISO) will enable observations to be made free of atmospheric absorption and will extend the wavelength regions covered by measuring lines at windows that are unobservable from earth. Another planned future observatory is the 3 meter airborne infrared telescope SOFIA that will replace the Kuiper airborne observatory, currently installed in a Boeing 747. The already underway Gemini project will build two 8 meter telescopes, one in Hawaii and one in Chile. The combined power from these telescopes associated with their low emissivity, will provide unprecedented image quality (better than 0.1 arcseconds) from infrared to ultraviolet wavelengths. The expected progress in the solid state detector technology will also provide detector arrays with higher sensitivities to use in conjunction with these telescopes.

Important projects already underway are the study of the FeII bullets in Orion for which we have recently acquired data. We have taken high spectral resolution profiles of several of these and the asymmetric profiles seems to indicate the presence of bow shock structures. In addition, recent H_2 observations of the Orion shocked region have produced high spatial (1″) and spectral (12 km s^{-1}) resolution images of the main shocked region and together with the FeII velocity information, will allow a in-depth study of the physics and dynamics of the velocity field. This links to the study of bow structures in shocked gas and a future project will be to calculate optical and H_2 line profiles from individual sections of the bow to match the spatial resolution now achievable. Another promising project seems to be the possibility of obtaining high spectral resolution profiles of the high excitation line of H_2. These will be used to explore the effect of fluorescence emission in objects that were previously thought to be purely shocked and will provide a powerful tool to discriminate between different shock models.

These advances in the observational resources will unquestionably lead to advances in the theoretical understanding of the physics and chemistry that ultimately link to the energetic phenomena observed in these star formation regions. No doubt many more questions will arise in the process, but a new level of understanding will be reached in due course. These are the thrills of scientific research.

References

Bachiller, R. and Chernicharo, J. (1990), *Astronomy & Astrophysics,* **239**: 276-286.

Bally, J. and Lane, A. (1991), "Shocked molecular hydrogen associated with Herbig-Haro objects and molecular outflows: The Cepheus-A flow". Astrophysics with Infrared Arrays, Astronomical Society of the Pacific Conference series,:

Beckwith, S., Persson, S., Neugebauer, G. and Becklin, E. (1978), *Astrophysical Journal,* **223**: 464.

Black, J. and Dalgarno, A. (1976), *Astrophysical Journal,* **203**: 132.

Black, J. and van Dishoeck, E. (1987), *Astrophysical Journal,* **322**: 412-449.

Blitz, L. (1991), Star Forming Giant Molecular Clouds. "The Physics of Star Formation and Early Stellar Evolution". Netherlands, Kluwer Academic Publishers. ed. 3-33.

Blitz, L. and Shu, F. (1980), *Astrophysical Journal,* **238**: 148.

Böhm, K., Brugel, E. and Mannery, E. (1980), *Astrophysical Journal,* **235**: L137-L141.

Brand, P. (1991), The structure of shocks in molecular clouds: molecular hydrogen line emission from the Orion outflow.

Brand, P. (1993), Observations of molecular hydrogen in star forming regions.

Brand, P., Moorhouse, A., Burton, M., Geballe, T., Bird, M. and Wade, R. (1988), *Astrophysical Journal (Letters),* **334**: L103-L106.

Brand, P., Toner, M., Geballe, T. and Webster, A. (1989a), *Monthly Notices of the Royal Astronomical Society,* **237**: 1009-1018.

Brand, P., Toner, M., Geballe, T., Webster, A., Williams, P. and Burton, M. (1989b), *Monthly Notices of the Royal Astronomical Society,* **236**: 929-934.

Brown, A., Jordan, C., Millar, T., Gondhalekar, P. and Wilson, R. (1981), *Nature,* **290**: 34.

Burton, M. (1986), PhD Thesis: *University of Edinburgh*

Burton, M. (1992), *submitted to Australian Journal of Physics,* :

Burton, M., Brand, P., Geballe, T. and Webster, A. (1989), *Monthly Notices of the Royal Astronomical Society,* **236**: 409-423.

Burton, M., Hollenbach, D. and Tielens, A. (1988), "IR line emission from dense photodissociation regions". 22nd Eslab symposium on infrared spectroscopy in astronomy, Salamanca, ESA EP series,:

Burton, M., Hollenbach, D. and Tielens, A. (1990), *Astrophysical Journal,* **365**: 620-639.

Cameron, M. and Liseau, R. (1990), *Astronomy & Astrophysics,* **240**: 409-428.

Campbell, M., Hoffmann, W., Thronson, H., Niles, D., Nawfel, R. and Hawrylycz, M. (1982), *Astrophysical Journal,* **261**: 550.

Carr, J. (1993), *Astrophysical Journal,* **406**: 553-562.

Chapman, A., Beard, S., Mountain, M., Pettie, D., Pickup, A. and Wade, R. (1990), "Reduction of data from the UKIRT common-user long slit 1-5μm spectrometer (CGS4)". SPIE: Instrumentation in Astronomy VII, **1235**: 25.

Chernoff, D. (1987), *Astrophysical Journal,* **312**: 143.

Chernoff, D., Hollenbach, D. and McKee, C. (1982), *Astrophysical Journal (Letters),* **259**: L97.

Chernoff, D. and McKee, C. (1990), Shocks in dense molecular clouds. "Molecular Astrophysics". Cambridge University Press. ed. 360-373.

Chrysostomou, A. (1992), PhD Thesis: *Edinburgh Univ.*

Dabrowski, I. (1984), *Canadian Journal of physics,* **62**: 1179-1953.

Dalgarno, A., Black, J. and Weisheit, J. (1973), *Astrophysical Journal (Letters),* **14**: 77.

Dame, M., Elmegreen, B., Cohen, R. and Thaddeus, P. (1986), *Astrophysical Journal,* **305**: 892.

Downes, D. and Rinehart, R. (1966), *Astrophysical Journal,* **144**: 937.

Draine, B. (1980), *Astrophysical Journal,* **241**: 1021-1038.

Draine, B. (1988), "Interstellar extinction in the infrared". 22nd Eslab Symposium on Infrared Spectroscopy in Astronomy, Salamanca, Spain, ESA pulication Divisions,**ESA SP-290**: 93-98.

Draine, B. (1991), Magnetohydrodynamic shock waves in molecular clouds. "Fragmentation of molecular clouds and star formation". Printed in the Netherlands. ed. 185-196.

Draine, B. and McKee, C. (1993), *to appear in Annual Review of Astronomy and Astrophysics,* **31**:

Draine, B. and Roberge, W. (1982), *Astrophysical Journal (Letters),* **259**: L91-L96.

Draine, B., Roberge, W. and Dalgarno, A. (1983), *Astrophysical Journal,* **264**: 485.

Duley, W. and Whittet, D. (1992), *Monthly Notices of the Royal Astronomical Society,* **255**: 243-247.

Duley, W. and Williams, D. (1986), *Monthly Notices of the Royal Astronomical Society,* **223**: 177-182.

Eislöffel, J. and Mundt, R. (1992), *submitted to Astronomy & Astrophysics,* :

Fischer, J., Righini-Cohen, G. and Simon, M. (1980), *Astrophysical Journal (Letters),* **238**: L155.

Fischer, J., Sanders, D., Simon, M. and Solomon, P. (1985), *Astrophysical Journal,* **293**: 508.

Flower, D. and Watt, G. (1984), *Monthly Notices of the Royal Astronomical Society,* **209**: 25.

Garden, R., Geballe, T., Gatley, I. and Nadeau, D. (1986), *Monthly Notices of the Royal Astronomical Society,* **220**: 203-221.

Garden, R., Geballe, T., Gatley, I. and Nadeau, D. (1991a), *Astrophysical Journal,* **366**: 474-483.

Garden, R., Hayashi, M., Gatley, I., Hasegawa, T. and kaifu, N. (1991b), *Astrophysical Journal,* **374**: 540-554.

Garden, R., Russell, A. and Burton, M. (1990), *Astrophysical Journal,* **354**: 232-241.

Gatley, I., Hasegawa, T., Suzuki, H., Garden, R., Brand, P., Lightfoot, J., Glencross, W., et al. (1987), *Astrophysical Journal (Letters),* **318**: L73.

Gautier, T., Fink, U., Treffers, R. and Larson, H. (1976), *Astrophysical Journal (Letters),* **207**: L129.

Geballe, T. and Garden, R. (1990), *Astrophysical Journal,* **365**: 602-605.

Genzel, R. (1991), Physical conditions and heating/cooling processes in high mass star formation regions. "The Physics of Star Formation and Early Stellar Evolution". Netherlands, Kluwer Academic Publishers. ed. 155-219.

Graham, J., Wright, G., Hester, J. and Longmore, A. (1991), *The Astronomical Journal,* **101**: 175.

Hartigan, P., Curiel, S. and Raymond, J. (1989), *Astrophysical Journal (Letters),* **347**: L31.

Hartigan, P., Raymond, J. and Hartmann, L. (1987), *Astrophysical Journal,* **316**: 323-348.

Harvey, P., Campbell, M. and Hoffmann, W. (1977), *Astrophysical Journal,* **211**: 786.

Harvey, P., Joy, M., Lester, D. and Wilking, B. (1986), *Astrophysical Journal,* **300**: 737.

Heiles, C. (1976), *Annual Review of Astronomy and Astrophysics,* **14**: 1.

Herbig, G. and Jones, B. (1983), *The Astronomical Journal,* **88**: 1040-1052.

Hertzberg, G. (1950), "Molecular Spectra and Molecular Structure". D. Van Nostrand Company, Inc.

Hollenbach, D., Chernoff, D. and McKee, C. (1988), "Infrared diagnostics of interstellar shocks". Proceedings of the 22nd Eslab Symposium on Infrared Spectroscopy in Astronomy, Salamanca, Spain, ESA publications Division,**ESA SP-290**: 245-258.

Hollenbach, D. and McKee, C. (1979), *Astrophysical Journal Supplement Series,* **41**: 555-592.

Hollenbach, D. and McKee, C. (1980), *Astrophysical Journal (Letters),* **241**: L47.

Hollenbach, D. and McKee, C. (1989), *Astrophysical Journal,* **342**: 306-336.

Hollenbach, D. and Salpeter, E. (1971), *Astrophysical Journal,* **163**: 155-180.

Hollenbach, D. and Shull, M. (1977), *Astrophysical Journal,* **216**: 419.

Jaffe, D., Genzel, R., Harris, A., Lugten, J., Stacey, G. and Stutzki, J. (1989), *Astrophysical Journal,* **344**: 265-276.

Jura, M. (1974), *Astrophysical Journal,* **191**: 375-379.

Kwan, J. (1977), *Astrophysical Journal,* **216**: 713.

Lada, C. (1985), *Annual Review of Astronomy and Astrophysics,* **23**: 267-317.

Landau, L. and Lifshitz, E. (1987), "Fluid Mechanics". Pergamon press.

Lang, K. (1992), "Astrophysical data: Planets and Stars". Springer-Verlag.

Langer, W. (1985), "Protostars and Planets II". Tucson, University of Arizona Press. ed. 650.

Lepp, S. and McCray, R. (1983), *Astrophysical Journal,* **269**: 560.

Lizano, S., Heiles, C., Rodríguez, L., Koo, B., Shu, F., Hasegawa, T., Hayashi, S., et al. (1988), *Astrophysical Journal,* **328**: 763-776.

London, R., McCray, R. and Chu, S. (1977), *Astrophysical Journal,* **217**: 442-447.

Masson, C., Mundy, L. and Keene, J. (1990), *Astrophysical Journal (Letters),* **357**: L25-L28.

Mathis, J., Rumpl, W. and Nordseick, K. (1977), *Astrophysical Journal,* **217**: 425-433.

McKee, C. (1989), *Astrophysical Journal,* **345**: 782-801.

McKee, C. and Draine, B. (1991), *Science,* **252**: 397-403.

McKee, C. and Hollenbach, D. (1980), *Annual Review of Astronomy and Astrophysics,* **18**: 219-262.

McKee, C. and Hollenbach, D. (1987), *Astrophysical Journal,* **322**: 275.

Meyers, P. and Goodman, A. (1988), *Astrophysical Journal (Letters),* **326**: L27.

Moorhouse, A., Brand, P., Geballe, T. and Burton, M. (1990a), *submitted to Monthly Notices of the Royal Astronomical Society,* :

Moorhouse, A., Brand, P., Geballe, T. and Burton, M. (1990b), *Monthly Notices of the Royal Astronomical Society,* **242**: 88-91.

Mountain, C., Robertson, D., Lee, T. and Wade, R. (1990), "An advanced cooled grating spectrometer for UKIRT". SPIE Symposium on Astronomical Telescopes and Instrumentation for the 21st Century, Tucson, :

Nadeau, D. and Geballe, T. (1979), *Astrophysical Journal,* **230**: 169.

Nadeau, D., Riopel, M. and Geballe, T. (1991), *Astrophysical Journal (Letters),* **372**: L103-L106.

Norman, C. and Silk, J. (1979), *Astrophysical Journal,* **228**: 197.

Outred, M. (1978), *Journal of Physical and Chemical Reference Data,* **7**: 81.

Press, W., Flannery, B., Teukolsky, S. and Vetterling, W. (1986), "Numerical Recipes". Cambridge University Press.

Puxley, P., Beard, S. and Ramsay, S. (1992), Reduction of data from the UKIRT Common-User long slit 1-5μm spectrometer. "to appear in Proceedings of 4th ESO/ST-ECF Data Analysis Workshop". ed.

Raymond, J., Hartigan, P. and Hartmann, L. (1988), *Astrophysical Journal,* **326**: 323-333.

Rieke, G. and Lebofsky, M. (1985), *Astrophysical Journal,* **288**: 618-621.

Roberge, W. and Dalgarno, A. (1982), *Astrophysical Journal,* **255**: 176.

Rodríguez, L., Lizano, S., Cantó, J., Escalante, V. and Mirabel, I. (1990), *Astrophysical Journal,* **365**:

Schwartz, R. (1978), *Astrophysical Journal,* **233**: 884.

Schwartz, R. (1983), *Astrophysical Journal (Letters),* **268**: L37-L40.

Schwartz, R., Cohen, M. and Williams, P. (1987), *Astrophysical Journal,* **322**: 403-411.

Schwartz, R., Dopita, M. and Cohen, M. (1985), *The Astronomical Journal,* **90**: 1820.

Shull, J. and Draine, B. (1987), The physics of interstellar shock waves. "Interstellar processes". Dordrecht, D. Reidel Publishing Company. ed. 283-319.

Shull, J. and Hollenbach, D. (1978), *Astrophysical Journal,* **220**: 525-537.

Shull, M. and McKee, C. (1979), *Astrophysical Journal,* **227**: 131-149.

Smith, M. (1991a), *Monthly Notices of the Royal Astronomical Society,* **252**: 378-385.

Smith, M. (1991b), Molecular J-shocks: Speed Limit and Excitation Level. Preprint

Smith, M. (1991c), Shocks in molecular clouds: Switches & Bows. Preprint

Smith, M. and Brand, P. (1989), *Monthly Notices of the Royal Astronomical Society,* **243**: 498.

Smith, M. and Brand, P. (1990a), *Monthly Notices of the Royal Astronomical Society,* **242**: 495-504.

Smith, M. and Brand, P. (1990b), *Monthly Notices of the Royal Astronomical Society,* **245**: 108.

Smith, M., Brand, P. and Moorhouse, A. (1991a), *Monthly Notices of the Royal Astronomical Society,* **248**: 451.

Smith, M., Brand, P. and Moorhouse, A. (1991b), *Monthly Notices of the Royal Astronomical Society,* **248**: 730.

Snell, R. and Edwards, S. (1981), *Astrophysical Journal,* **251**: 103.

Solf, J. and Böhm, K. (1987), *Astrophysical Journal,* **93**: 1172-1181.

Spitzer, L. (1978), "Physical processes in the interstellar medium". Wiley-Interscience publication.

Stapelfeldt, K., Beichman, C., Hester, J., Scoville, N. and Gautier III, T. (1991), *Astrophysical Journal,* **371**: 226-236.

Sternberg, A. (1988), "The excitation of molecular hydrogen and its significance". Proceedings of the 22nd Eslab Symposium on Infrared Spectroscopy in Astronomy, Salamanca, Spain, ESA publications Division,**ESA SP-290**: 269-280.

Sternberg, A. and Dalgarno, A. (1989), *Astrophysical Journal,* **338**: 197-233.

Stutzki, J., Stacey, G., Genzel, R., Harris, A., Jaffe, D. and Lugten, J. (1988), *Astrophysical Journal,* **332**: 379.

Tielens, A. and Hollenbach, D. (1985), *Astrophysical Journal,* **291**: 722.

Treffers, A., Fink, U., Larson, H. and Gautier, T. (1976), *Astrophysical Journal,* **291**: 722.

Troland, T. and Heiles, C. (1986), *Astrophysical Journal,* **301**: 339.

Turner, J., Kirby-Docken, K. and Dalgarno, A. (1977), *Astrophysical Journal Supplement Series,* **35**: 281-292.

Wardle, M. (1991), *Monthly Notices of the Royal Astronomical Society,* **251**: 119.

Wardle, M. and Draine, B. (1987), *Astrophysical Journal,* **321**: 321-333.

Watson, D., Genzel, R., Townes, C. and Storey, J. (1985), *Astrophysical Journal,* **298**: 316.

Whittet, D. (1988), The observed properties of interstellar dust in the infrared. "Dust in the Universe". Cambridge University Press. ed. 25-53.

Witt, A., Bohlin, R. and Stecher, T. (1984), *Astrophysical Journal,* **279**: 698-704.

Wynn-Williams, C., Becklin, E. and Neugebauer, G. (1974), *Astrophysical Journal,* **187**: 473.

Zel'dovich, Y. and Raizer, Y. (1967), "Physics of shock waves and high-temperature hydrodynamic phenomena". Moscow, Academic Press.

Zinnecker, H., Mundt, R., Geballe, T. and Zealey, W. (1989), *Astrophysical Journal,* **342**: 337-344.